

Transient Magnetospheric Response to Solar Wind Discontinuities

Ryuhō Kataoka

2003

Acknowledgments

Abstract

1	Introduction	1
1.1	Transient Response of the Earth's Magnetosphere	1
1.2	Magnetic Impulse Events and Traveling Convection Vortices	3
1.3	Purpose of This Thesis	6
2	Comprehensive Event Study of TCVs	7
2.1	Data Set	7
2.1.1	Ground Magnetometers	7
2.1.2	Super Dual Auroral Radar Network	8
2.1.3	Satellite Observations	9
2.2	Method of Analysis	12
2.2.1	Magnetometer Data Analysis	12
2.2.2	Solar Wind Data Analysis	13
2.3	Results	14
2.3.1	Geomagnetic Disturbances	14
2.3.2	Ionospheric Disturbances	17
2.3.3	Auroral Dynamics	19
2.3.4	Interplanetary Conditions	20
2.4	Discussion	24
2.4.1	F region Plasma Irregularity	24
2.4.2	Spectral Width Enhancement	27
2.4.3	Generation Mechanism	29
2.4.4	Energetics	32
2.5	Summary	36

3	Statistical Study of MIEs	37
3.1	Magnetometer Data Analysis	37
3.2	Solar Wind Discontinuity Analysis	40
3.3	Occurrence Properties	44
3.4	Discussion	48
3.5	Summary	52
4	Simulation of TCVs	53
4.1	Simulation Model	53
4.2	Ionospheric Disturbances	56
4.3	Magnetospheric Disturbances	58
4.4	Wave Equation of Field-aligned Currents	59
4.5	Discussion	61
4.6	Summary	64
5	Conclusion	65
	References	66
	Vita	73

Acknowledgments

There are many people without whom this work would not have been completed. The informative guidance and unfailing encouragements of Prof. Hiroshi Fukunishi as my academic advisor have been pivotal, and deserve many thanks. The insightful suggestions of Dr. Louis J. Lanzerotti have helped me as the basis of my research, and his words always made me strong. Dr. Keisuke Hosokawa extended tremendous help for my SuperDARN analysis. Dr. Shigeru Fujita provided lots of help on the simulation work.

I would also like to thank Prof. A. Morioka, Prof. S. Okano, Prof. T. Ono, Dr. I. Murata, Dr. Y. Takahashi, Dr. H. Misawa, and Dr. M. Iijima for evaluation of my dissertation. I am indebted to Dr. H. Fujiwara, Dr. T. Sakanoi, Dr. K. Sakanoi, Mr. M. Sato, Mr. Y. Yamada, and Mr. N. Yoshida for their helpful comments. I am also thankful to Dr. T. Kikuchi, Dr. T. Tanaka, Dr. M. Itonaga, and Prof. T. Ogawa for fruitful discussions.

Data handling was supported by many excellent scientists. AGO data handling was supported by Dr. C. G. MacLennan, Prof. T. J. Rosenberg, Dr. A. T. Weatherwax, Dr. D. L. Detrick, , Dr. H. U. Frey, Dr. J. H. Doolittle, Dr. S. P. Geller, and Prof. S. B. Mende. MACCS magnetometer data was provided by Prof. M. Engebretson and Dr. J. Posch. Greenland magnetometer data was provided by Dr. J. Watermann and Prof. C. R. Clauer. SuperDARN data was provided by Prof. N. Sato and Dr. S. A. Yukimatu. POLAR UVI data was provided by Dr. Y.-K. Tung and Prof. G. Parks.

Almost six years have passed since I joined the Aurora Team to enjoy adventurous research life with my red MINI. I wish to acknowledge all the colleagues for various kinds of practical support and precious funny days. Special thanks go to Yumi Hirano, Saori Toyoshima, Tomoyuki Hasunuma, and Chihiro Tao for a lot of inspirations via collaborations.

This thesis is dedicated to my parents, Tadashi and Motoko Kataoka. A brief paragraph here can not express my gratitude for their love and patient support throughout my academic years.

Abstract

Because of their solitary characteristics, magnetic impulse events (MIEs) accompanied with traveling convection vortices (TCVs) are known as unique geomagnetic disturbances offering an opportunity to study the interaction processes among the solar wind, the bow shock, the magnetosphere, and the ionosphere. Although the transient response of the magnetosphere to the solar wind discontinuities is known as the most prominent cause of MIEs and TCVs, the detailed generation mechanisms of MIEs and TCVs remain unsolved. The purpose of this study is to elucidate their generation mechanisms and to understand the fundamental physical processes associated with the transient response of the Earth's magnetosphere to solar wind discontinuities.

For this purpose, a comprehensive event study is performed first, focusing on a TCV event on May 22, 1996. The whole available data are analyzed for this TCV event. From a three-dimensional analysis using multiple spacecraft, the solar wind source of this TCV event is identified to be a tangential discontinuity (TD) exhibiting a rapid turning of the interplanetary magnetic field (IMF). This TD has an abnormal orientation, and satisfies the criteria for the formation of the hot flow anomaly (HFA) at the bow shock. The magnetopause deformations due to the HFA can explain not only the triggering process, but also the temporal and spatial evolution of the three-dimensional current system derived from ground magnetometer data analysis, and all other observed features of this TCV event. Other generation mechanisms such as direct compression due to solar wind pressure pulses or dayside reconnection burst alone can not explain all of these features. The three-dimensional current system of TCVs causes a transient production of localized dayside aurora and localized F region irregularities, with hundreds of km horizontal extent in the ionosphere. From a model fitting, the total current intensity of this current system is estimated as 0.1-1 MA, and the total power supply into the ionosphere is estimated as 1-10 GW.

In order to reveal the contribution rates of the HFA mechanism and other generation mechanisms to produce TCVs, a statistical analysis is performed, focusing on the relationship between MIEs and IMF discontinuities. Continuous wavelet transform is applied to the magnetometer data obtained at South Pole station to detect 825 MIEs automatically for the 8 year period 1995-2002. IMF discontinuities are also detected for the same 8 year period. Significant correlation is found between occurrences of MIEs and IMF discontinuities. The solar wind conditions of low-density, high-speed, and/or radial IMF are identified to be favorable for the production of MIEs. Of the 36 one-to-one correspondence events between MIEs and IMF discontinuities, ~70% of IMF discontinuities are found to be TDs. The HFA mechanism can explain at most ~50% of the MIEs, and dayside reconnection burst or solar wind pressure pulses are possibly associated with ~30% and ~20% of the

MIEs, respectively. All of the obtained results are consistent with HFAs and foreshock cavities being the main causes of MIEs.

The essential effect by the production of HFAs or foreshock cavities at the bow shock can be simplified and represented by a localized density pulse superposed just in front of the bow shock. The transient response of the magnetosphere and the ionosphere to such a localized density pulse is investigated using a global magnetohydrodynamic (MHD) simulation to quantitatively understand how the three-dimensional current system arises in the magnetosphere and the ionosphere. The simulated ionospheric disturbances exhibit many properties similar to those observed during actual TCVs. The simulated TCVs are driven by pairs of field-aligned currents. The generation mechanisms of the field-aligned currents in the magnetosphere are evaluated in terms of a wave equation of field-aligned currents. The source current is found to be inertial current associated with plasma acceleration in the magnetosphere near the impact region. The inertial current is converted into the field-aligned currents off from the equatorial plane via the curvilinear effect of the geomagnetic field. Inhomogeneous effect also contributes to generation of the field-aligned currents at the sharp gradient of Alfvén speed.

The whole topics associated with TCVs are compiled in this thesis. The generation mechanism and the energetics of TCVs are quantitatively revealed based on both observations and theories. The bow shock plays a dominant role for the generation of TCVs via the production of HFAs and foreshock cavities. It is concluded that TDs are the most effective solar wind discontinuities to produce TCVs, and the three-dimensional structure of TDs is essential to understand and to predict the transient response of the Earth's magnetosphere to solar wind discontinuities.

Chapter 1

Introduction

1.1 Transient Response of the Earth's Magnetosphere

The interplanetary space is not a perfect vacuum and is filled by magnetized tenuous plasma constantly flowing outward from the solar coronal region. This plasma flow is termed the solar wind, and the magnetic field existing in the solar wind is termed the interplanetary magnetic field (IMF). Because of large conductivity of the solar wind, IMF is “frozen in” to the solar wind plasma. In the vicinity of the Earth's orbit, normal solar wind speed, proton density, proton temperature, and IMF intensity are in the ranges of 300-800 km/s, 1-40 /cc, 10^3 - 10^6 K, and 0-20 nT, respectively.

Geomagnetic disturbances studied in this thesis are related to the microstructures of the solar wind with spatial scales of 1-10 R_E . These spatial scales correspond to the time scales of 10 s to several min in the vicinity of the Earth's orbit. Rapid IMF directional changes with such spatial scales are termed IMF discontinuities. IMF discontinuities are one of the fundamental microstructures of the solar wind plasma. Two types of IMF discontinuities are frequently observed in the vicinity of the Earth; tangential discontinuities (TDs) and rotational discontinuities (RDs). TDs are identified by a lack of the magnetic field normal across their surfaces. TDs are considered as a surface separating two different types of plasma because TDs have no mass flux across their surfaces. The direction and intensity of magnetic field, the density and temperature of plasma, and even the composition of plasma are different on both sides of the TD surface. TDs are “frozen in” to the solar wind and do not propagate with respect to the solar wind. On the other hand, RDs have the nonzero normal component of the magnetic field and have mass flow across their surfaces. RDs do not usually exhibit changes in the magnetic field intensity, and propagate with respect to the solar wind at the Alfvén speed.

The territory of the Earth's internal magnetic field is spatially confined due to the interaction between the geomagnetic field and the solar wind. This geomagnetic territory is termed the Earth's magnetosphere. The outer boundary of the Earth's magnetosphere is termed the magnetopause. The geomagnetic field is shielded by the surface current flowing on the magnetopause. The Alfvén mach number of the impinging solar wind is so large that a standing shock surface is formed ahead of the Earth's magnetopause. The curved shock surface is termed the bow shock. Across the bow shock, kinetic energy of the solar wind is converted into the thermal energy to slow the solar wind to sub-Alfvénic speed. The region of the sub-Alfvénic solar wind behind the bow shock is called the

magnetosheath.

The Earth's ionosphere is globally formed in the upper atmosphere in the altitude range 80-800 km. The altitude range 150-500 km is termed the F region. The altitude range 90-150 km is called the E region, and the ionization region below 90 km is termed D region. In the polar ionosphere, neutral atmosphere is effectively ionized by solar ultraviolet radiation and auroral electron precipitation. The peak plasma density region is called the F peak and this peak attains values as high as 10^6 /cc at noon. Near the peak of the plasma density the dominant ions are O^+ , although NO^+ and O_2^+ become more important below the peak.

In the magnetohydrodynamic (MHD) coupling system of the ionosphere and the magnetosphere, the ionosphere approximately behaves like a spherical conductive shell. Field-aligned currents generated in the magnetosphere act as a power supply into the conductive ionosphere. In response to this power supply, the ionospheric potential is formed to complete the zero divergence of the ionospheric currents, and ionospheric plasma moves along the equicontour lines of the ionospheric potential. This plasma motion is termed the plasma convection.

The Hall current, that is the horizontal ionospheric current flowing perpendicular to both the magnetic field and the electric field, flows oppositely to plasma convection and usually has negligible divergence. On the other hand, the Pederson current, that is the horizontal ionospheric current flowing perpendicular to the magnetic field and parallel to the electric field, contributes to establish the current system between the ionosphere and the magnetosphere. Ionospheric Joule heating is also caused by the Pederson current. Geomagnetic perturbations observed by ground magnetometers are mainly caused by the Hall current because magnetic perturbations due to the field-aligned current and the Pedersen current tends to be canceled on the ground [Fukushima, 1976].

Investigations of the mechanisms by which energy and momentum are transferred from the solar wind into the Earth's magnetosphere and ionosphere are an important subject of space plasma physics. There are two major processes of energy and momentum transfer; magnetic reconnection at the dayside magnetopause [Dungey, 1961] and magnetospheric compression due to dynamic pressure change of the solar wind impinging upon the magnetopause [Tamao, 1964]. The processes of the dayside reconnection and the magnetospheric compression are transient phenomena because typical time scales of these phenomena are 1-10 min as described below.

Short-lived (~5 min) bipolar magnetic field perturbations are frequently observed by spacecraft in the vicinity of the dayside magnetopause. This phenomenon is termed the flux transfer event (FTE) and interpreted as a product due to spatially localized (~1 R_E) reconnection at the dayside magnetopause by Russell and Elphic [1978]. The finding of FTEs indicates that the dayside reconnection is dominantly occurring as transient processes [Haerendel et al., 1978]. FTEs are observed during periods of southward IMF orientation [Lee et al., 1993]. The histogram of FTE

recurrence rate has a peak at 3 min and the mean value is 8 min [Lockwood and Wild, 1993]. Although a vast majority of transient solar wind-magnetosphere interaction is explained in terms of FTEs, the mechanism to produce FTEs is still controversial [e.g., Lockwood and Hapgood, 1998].

Another type of transient phenomena is a sudden compression of the magnetosphere. Regardless of IMF conditions, a rapid increase in the solar wind dynamic pressure causes such a sudden compression of the magnetosphere. As a result, jumps of the northward geomagnetic field intensity are observed by ground magnetometers worldwide but clearly in middle and low latitudes. This characteristic geomagnetic perturbation is called the sudden commencement (SC). The normal risetime of SC ranges from 1 to 20 min, and the jump in amplitude ranges from 10 to 100 nT. A scenario proposed by Araki [1994] successfully explains the overall characteristics of SCs.

1.2 Magnetic Impulse Events and Traveling Convection Vortices

The magnetic impulse events (MIEs), with amplitudes ranging from several tens to several hundreds of nanoteslas and durations ranging from 5 to 20 min, are often observed by dayside high-latitude ground magnetometers. Lanzerotti *et al.* [1986] first suggested that MIEs could be a possible ground signature of FTEs. Since FTEs explain a vast majority of the solar wind-magnetosphere interaction, this was a pioneering suggestion for investigating MIEs with great importance. Subsequently, using dense arrays of ground-based magnetometers, it was shown that a number of MIEs can be interpreted in terms of traveling convection vortices (TCVs) moving antisunward from the midday sector [Friis-Christensen *et al.*, 1988; Glassmeier *et al.*, 1989].

TCVs are identified as east-west aligned pairs of oppositely directed convection vortices which propagate eastward or westward at speeds of 3-10 km/s over 5-15 minutes through the dayside ionosphere in magnetic latitudes of 70°-80°. Each vortex has a spatial scale of 1000-2000 km, and twin vortices encompass a local time sector of several hours. Many TCVs show the magnetic conjugacy in northern and southern hemispheres [Lanzerotti *et al.*, 1991]. TCVs correspond to spatially localized and transient convection cells embedded in a large-scale convection pattern [Ridley *et al.*, 1998]. TCVs are accompanied by enhanced electric fields [Lühr *et al.*, 1993], localized dayside aurora [Vorobjev *et al.*, 1994a, 1994b; Lühr *et al.*, 1996], and pairs of upward/downward field-aligned currents [Vogelsang *et al.*, 1993]. Many TCVs are caused by sudden changes in solar wind pressure and/or IMF [Lanzerotti *et al.*, 1987; Friis-Christensen *et al.*, 1988; Glassmeier *et al.*, 1989; Sibeck *et al.*, 1989; Lin *et al.*, 1996a, 1996b; Cable and Lin, 1998]. Detailed mechanisms of the initiation and temporal evolution of TCVs remain open question because of at least two reasons. The first reason is a lack of sufficient magnetometer network observations. It is difficult to track TCVs without dense and extended magnetometer networks. The second reason is that the solar wind origins of TCVs are not as obvious as the cases of FTEs or SCs. Because of their mysteries but

solitary features, TCVs are now recognized as the most important phenomenon to understand the transient coupling processes among the solar wind, the magnetosphere, and the ionosphere.

Statistical properties of MIEs have been investigated by many researchers. Note that the term “MIEs” is basically used in this thesis as a magnetic signature of TCVs to ignore complicated problems in terminology. Using the Scandinavian magnetometer array in magnetic latitude from $\sim 55^\circ$ to $\sim 67^\circ$, *Glassmeier et al.* [1989] first showed that TCV occurrences have a single-peak distribution with a maximum occurrence in the magnetic local morning. On the other hand, based on conjugate magnetometer observations at magnetic latitudes of 73° - 74° , *Lanzerotti et al.* [1991] showed that MIE occurrences have a double-peak distribution around magnetic local noon. Also, *Lanzerotti et al.* [1991] showed an average occurrence rate of 1.1 event/day. The maximum amplitudes of MIEs tend to be larger in the prenoon sector than in the postnoon sector [*Sibeck and Korotova*, 1996]. It is also known that MIE occurrences have preference for radial IMF conditions [*Konik et al.*, 1994; *Sibeck and Korotova*, 1996; *Vorobjev et al.*, 1999]. The long term trend of MIE/TCV occurrences is still under debate. The presence of semi-annual peaks of MIE occurrences was reported by *Sibeck and Korotova* [1996], based on magnetometer data acquired in the northern hemisphere. In contrast, *Glassmeier et al.* [1989] found a minimum in occurrence during equinox, while *Zesta et al.* [2002] concluded that there is no clear seasonal variation for TCV events.

Recently, the bow shock has been considered as a possible source region for TCVs since a hot flow anomaly (HFA) observed in the vicinity of the bow shock was shown to cause a TCV event via gross deformation (by some $5 R_E$) of the dayside magnetopause [*Sibeck et al.*, 1998, 1999; *Sitar et al.*, 1998]. HFAs, a kind of diamagnetic cavities [*Schwartz et al.*, 1985], have enhanced temperatures (10^6 - 10^7 K) and large deflection of solar wind flow in the cavity structure. Such structures of a HFA are consequences of ions reflected at the bow shock being channeled along the current sheet of an incident TD [*Schwartz*, 1995]. This process requires a motional electric field pointing toward the TD on at least one side [*Schwartz et al.*, 2000].

Phenomena similar to HFAs without these enhanced temperature and flow deflection are called foreshock cavities. The foreshock cavities are frequently present in foreshock regions of quasi-parallel shocks [*Sibeck et al.*, 2001]. Both HFAs and foreshock cavities were reasonably reproduced by recent global hybrid simulations, and it was shown that the arrival of IMF discontinuities is not needed to form the foreshock cavities [*Lin*, 2002, 2003]. *Sibeck et al.* [1989] and *Fairfield et al.* [1990] originally associated the foreshock cavities with compressions and rarefactions of the dayside magnetosphere. Recently, *Murr and Hughes* [2003] showed from in-situ measurements of foreshock cavities that a vast majority of TCVs in their study resulted from the foreshock cavities. However, the solar wind origins of TCVs far upstream of the bow shock are not fully understood yet, particularly in terms of the importance of IMF discontinuities for the generation of TCVs.

The generation mechanisms of TCVs are also controversial, although recent observations suggest that small-scale pressure pulses are the most probable cause of TCVs [*Sibeck et al.*, 2003; *Murr and Hughes*, 2003]. As summarized by *Cowley* [2000], there are at least three generation mechanisms of field-aligned currents due to localized pressure pulses impinging upon the magnetopause. *Glassmeier* [1992] suggested the generation of a single field-aligned current at each end of a perturbed region based on the continuity of perturbed magnetopause current. *Kivelson and Southwood* [1991] predicted field-aligned current pair at each end by considering sheared flows due to in-out boundary motions. It is noted that the dominant source is diamagnetic current for the *Glassmeier's* [1992] model and inertia current for the *Kivelson and Southwood's* [1991] model, although field-aligned currents flow on the magnetopause in both models. On the other hand, *Lühr et al.* [1996] suggested that field-aligned currents are associated with the divergence of inertia currents at sharp density gradients on the inner edge of the low latitude boundary layer (LLBL). These three models paid attention to the processes in the equatorial plane. Combining these models, the recent work of *Sibeck et al.* [2003] approximates the relationship between field-aligned currents and localized pressure pulses in the LLBL in the equatorial plane. They showed that the most essential parameter in the source region is the azimuthal gradient of perturbed total pressure. Both inertial and diamagnetic currents are mixed as the source current in their hypothesis.

TCVs were also studied using numerical simulation techniques. *Lysak and Lee* [1992] simulated the transient response of the dipole magnetosphere to pressure pulses using a set of linearized cold plasma MHD equations. Their result showed that vortex structures tend to form on field lines resonant with the source frequency. *Slinker et al.* [1999] are the first researchers who investigated the response of the ionosphere to a density pulse in the solar wind using a global MHD simulation. They also reproduced pairs of ionospheric convection vortices traveling away from noon. *Chen et al.* [2000] investigated the response of the magnetosheath and the magnetosphere to a pressure enhancement accompanied by a TD using a global MHD simulation. They showed that tailward traveling twin vortices and shear Alfvén waves arise in the dayside magnetosphere. These simulations tell us that the solar wind pressure pulse is one of the most fundamental sources of field-aligned currents driving TCVs. However, it is still unclear which proposed mechanisms of localized pressure pulses dominantly contribute to the generation of the field-aligned currents in the magnetosphere.

1.3 Purpose of This Thesis

As described above, the generation mechanism of TCVs is still controversial, although TCVs are unique geomagnetic disturbances offering an opportunity to study the interaction processes among the solar wind, the bow shock, the magnetosphere, and the ionosphere. The purpose of this thesis is to elucidate the generation mechanism of TCVs and to understand the fundamental physical processes associated with the transient response of the Earth's magnetosphere to solar wind discontinuities. **Chapter 2** describes the results obtained from a comprehensive event study of TCVs. The whole features and energetics of TCVs are discussed. **Chapter 3** presents the results of a statistical study on MIEs. Long-term observation data over the 8-year period 1995-2002 make it possible to identify the solar wind origins of MIEs. The relationship between MIEs and IMF discontinuities are discussed. **Chapter 4** presents the results of a simulation of TCVs. Three-dimensional global MHD simulation reveals that there are different types of sources for field-aligned currents to produce the simulated TCVs. Finally, this thesis is concluded in **Chapter 5**.

Chapter 2

Comprehensive Event Study of TCVs

This Chapter presents the results of a comprehensive event study on traveling convection vortices (TCVs). Data analysis is concentrated on a TCV event on May 22, 1996 because this event has a comprehensive data set which provides information on all topics discussed throughout this thesis. The whole available data are analyzed in this study in order to investigate the temporal and spatial evolution of TCVs. Several other events are referenced as additional evidences for discussing underlying physics in more detail. **Table 2.1** shows the list of TCV events mainly consulted in this Chapter. All the listed events occurred in summer under quiet geomagnetic activity conditions.

Table 2.1. List of TCV events.

Date	UT	Kp	References
1996/05/22	1312	2	[Mende <i>et al.</i> , 2001; Kataoka <i>et al.</i> , 2002, 2003]
1996/07/24	1138	1	[Sibeck <i>et al.</i> , 1999; Kataoka <i>et al.</i> , 2003]
1997/06/06	1611	1+	[Kataoka <i>et al.</i> , 2001]
1998/05/27	1610	1+	[Kataoka <i>et al.</i> , 2002]

2.1 Data Set

2.1.1 Ground Magnetometers

Continuous magnetic field data obtained from ground-based magnetometer stations are the most stable and useful diagnostic tool for investigating transient geomagnetic disturbance events. The locations of magnetometer stations used in this study are shown in **Figure 2.1**. The coordinates of the magnetometers are provided in **Table 2.2**. The CANOPUS (Canadian Auroral Network for the OPEN Program Unified Study) network [Rostoker *et al.*, 1995] is shown by triangles. Greenland coastal and ice cap stations are shown by diamonds. The MACCS (Magnetometer Array for Cusp and Cleft Studies) magnetometer stations in Canada [Hughes and Engebretson, 1997] are shown by squares. Antarctic magnetometer stations are shown by circles. The overall instrumentation and objectives of the U.S. Automatic Geophysical Observatories (AGOs) in Antarctica are provided by Rosenberg and Doolittle [1994]. The time resolutions are 5 s, 20 s, 5 s, and 1 s for CANOPUS, Greenland, MACCS, and Antarctic networks, respectively. In Antarctica, search-coil magnetometers

are also installed at AGOs, South Pole (SP), and McMurdo (MM), with sampling frequencies of 2 Hz, 10 Hz, and 10 Hz, respectively.

The SYM-H index is available from the World Data Center for Geomagnetism, Kyoto University (<http://swdcwww.kugi.kyoto-u.ac.jp/>). The SYM-H index is basically the same as Sugiura's hourly Dst index [Sugiura and Poros, 1971] except that the SYM-H index consists of 1 min values from a different set of stations and uses a slightly different coordinate system. The SYM-H index is useful to identify occurrences of sudden commencements (SCs). Also, careful comparisons between variations in solar wind dynamic pressure and the SYM-H index enable us to precisely estimate the propagation time of interplanetary transient phenomena to the ground.

2.1.2 Super Dual Auroral Radar Network

The SuperDARN (Super Dual Auroral Radar Network) coherent HF radars are designed to employ backscatter from high-latitude, field-aligned ionospheric plasma density irregularities as tracers of bulk plasma motion under the influence of the convection electric field [Greenwald *et al.*, 1985, 1995]. Each radar is operated at a specific frequency within the range from 8 to 20 MHz, although the operating frequency is typically ~10 MHz, which corresponds to a wavelength of scattering plasma irregularities of 15 m. During the May 22 event, the whole radars were running in normal scan mode. The radar scans through 16 beams in every two minutes and the dwell time on each beam is 7 s. Each beam is separated into 75 range gates, 45 km in length with a distance to the first gate of 180 km. Doppler line-of-sight velocities and spectral widths are derived by the FITACF algorithm [Villain *et al.*, 1987; Baker *et al.*, 1988].

The Doppler spectral width is a measure of the variation of the electric field in both the spatial domain (the radar sampling cell, typically 45 km by 100 km in dimension) and the time domain (variations occurring during the radar integration time which is 7 s). A large increase in the Doppler spectral width indicates that the electric field has varied rapidly in one or both of these two domains. Andre *et al.* [1999, 2000] evaluated the impact of a time-varying electric field on the Doppler spectral width. A number of researchers demonstrated that the equatorward edge of the radar backscatter region showing broad (>220 m/s) Doppler spectral widths is coincident with the equatorward edge of the cusp particle precipitation and OI 630.0 nm auroral region [Baker *et al.*, 1995; Rodger *et al.*, 1995; Yeoman *et al.*, 1997; Milan *et al.*, 1999].

2.1.3 Satellite Observations

With the advent of the International Solar Terrestrial Physics (ISTP) program, data from a number of satellite missions are used to investigate the interplanetary conditions that prevailed at the time of the TCV event. Interplanetary data from the spacecraft ACE, Wind, IMP8, Interball, and Geotail spacecraft have been used in order to provide information on the interplanetary magnetic field (IMF), solar wind velocity, proton number density, and proton temperature. All of these data are available at CDAWeb (<http://cdaweb.gsfc.nasa.gov/>) operated by the Space Physics Data Facility at Goddard Space Flight Center. Magnetometer data from the GOES spacecraft are also available at the CDAWeb, and are used to investigate geosynchronous magnetic field perturbations.

Data from the Ultraviolet Imager (UVI) instrument aboard the POLAR spacecraft [*Torr et al.*, 1995] are used to investigate the effect of auroral electron precipitation in global view. The UVI has five filters with different wavelength bands. The band used for this study is the Lyman-Birge-Hopfield long (LBHL) band in the range of 160-180 nm. The auroral brightness from the LBHL band depends mainly on the total precipitating energy flux over a wide range of precipitating electron energy [*Germany et al.*, 1994]. All images shown in this Chapter are integrated for 36.8 s. Line-of-sight correction, cosmic ray removal, and dayglow removal are also performed as preprocessing.

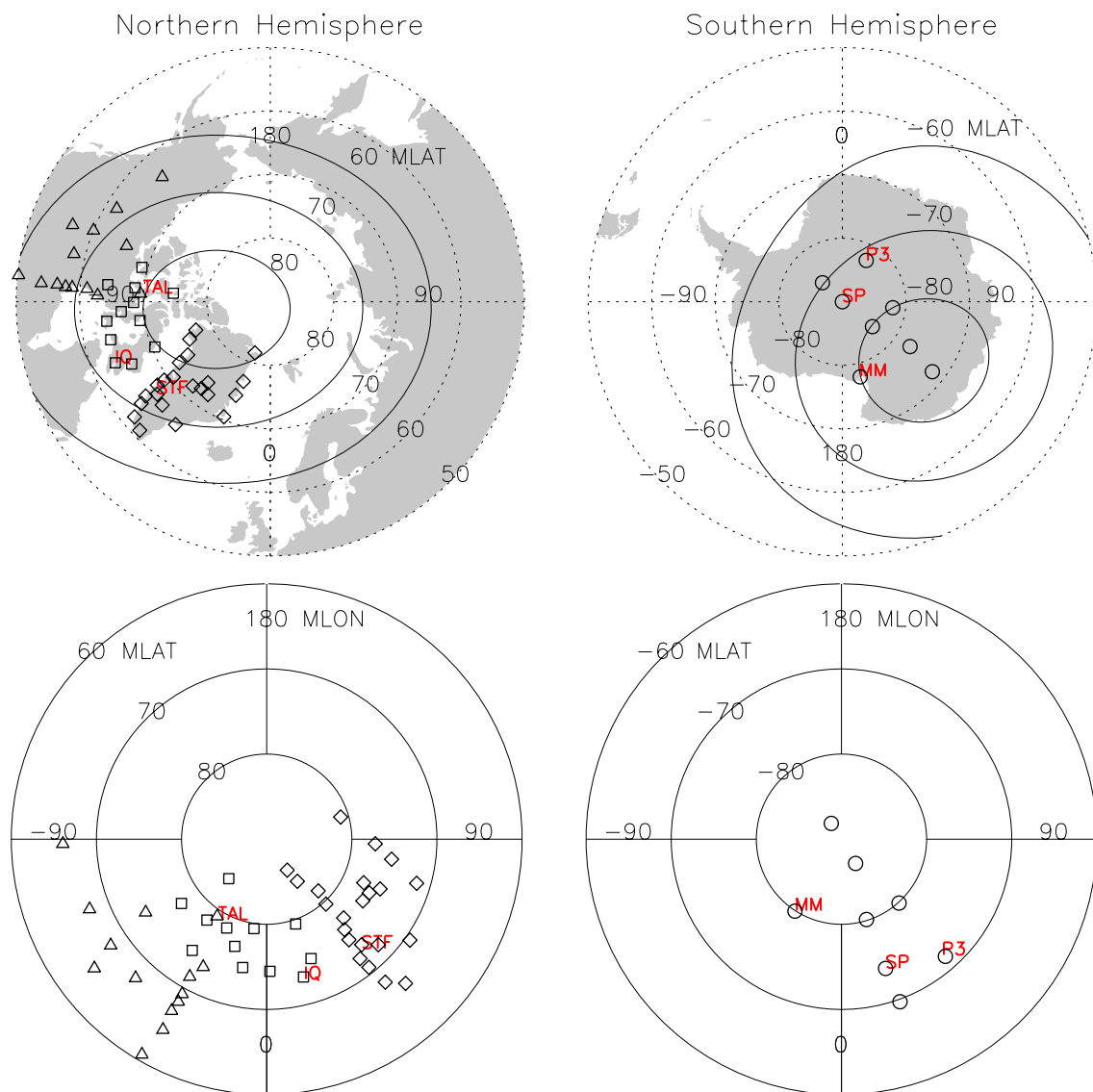


Figure 2.1. Magnetometer station map in northern and southern polar regions higher than 50° geographic latitudes (top), and higher than 60° corrected geomagnetic latitudes (bottom). Corrected geomagnetic latitudes of 60°, 70°, and 80° are indicated by solid lines in the top maps. Magnetometer stations of CANOPUS, MACCS, Greenland, and Antarctic networks are shown by triangles, squares, diamonds, and circles, respectively. Red characters show the magnetically conjugate magnetometer stations analyzed in **Section 2.3.1**.

Table 2.2. Geographic (GLAT and GLON) and corrected geomagnetic (MLAT and MLON) coordinates of magnetometer stations. MLTMN is given by UT of magnetic local midnight.

Station	Code	GLAT	GLON	MLAT	MLON	MLTMN
CANOPUS						
Taloyoak	TAL	69.54	266.45	78.90	329.02	6:44
Rankin Inlet	RAN	62.82	267.89	72.85	334.68	6:26
Rabbit Lake	RAB	58.22	256.32	67.32	317.57	7:25
Pinawa	PIN	50.20	263.96	60.50	330.60	6:40
Fort McMurray	MCM	56.66	248.79	64.52	307.66	8:02
Island Lake	ISL	53.86	265.34	64.20	332.18	6:34
Gillam	GIL	56.38	265.36	66.63	331.81	6:35
Fort Smith	SMI	60.02	248.05	67.64	305.18	8:11
Fort Simpson	SIM	61.76	238.77	67.46	292.49	9:01
Fort Churchill	CHU	58.76	265.92	68.93	332.27	6:34
Eskimo Point	ESK	61.11	265.95	71.14	331.80	6:35
Dawson	DAW	64.05	220.89	65.93	272.24	10:31
Contwoyto Lake	CON	65.75	248.75	73.19	302.65	8:20
Back	BAK	57.72	265.83	67.94	332.32	6:34
MACCS						
Pangnirtung	PG	66.10	294.20	74.64	19.90	3:47
Clyde River	CY	70.50	291.40	79.08	18.38	3:53
Iqaluit	IQ	63.80	291.50	72.83	14.79	4:07
Cape Dorset	CD	64.20	283.40	74.01	1.60	4:54
Igloolik	IG	69.30	278.20	78.96	352.63	5:25
Coral Harbour	CH	64.10	276.80	74.21	350.07	5:34
Repulse Bay	RB	66.50	273.80	76.43	344.37	5:53
Pelly Bay	PB	68.50	270.30	78.18	337.11	6:17
Baker Lake	BL	64.30	264.00	73.93	327.53	6:50
Gjoa Haven	GH	68.60	264.10	77.87	325.24	6:57
Cambridge Bay	CB	69.10	255.00	77.25	308.91	7:56
Resolute Bay	RE	74.70	265.00	83.33	319.30	7:17
Greenland						
Qaanaaq	THL	77.48	290.83	85.28	31.85	3:01
Savissivik	SVS	76.02	294.90	83.53	34.62	2:49
Kullorsuaq	KUV	74.57	302.82	81.14	43.44	2:10
Upernavik	UPN	72.78	303.85	79.39	41.13	2:20
Ummannaq	UMQ	70.68	307.87	76.81	43.17	2:10
Qeqertarsuaq	GDH	69.25	306.47	75.70	39.70	2:25
Attu	ATU	67.93	306.43	74.45	38.36	2:31
Kangerlussuaq	STF	67.02	309.28	73.06	41.14	2:19
Manitsoq	SKT	65.42	307.10	71.88	37.42	2:36
Nuuk	GHB	64.17	308.27	70.45	38.00	2:33
Paamiut	FHB	62.00	310.32	67.90	39.16	2:28
Narsarsuaq	NAQ	61.18	314.56	66.21	43.43	2:08
Nord	NRD	81.60	343.33	81.02	104.85	21:20
Danmarkshavn	DMH	76.77	341.37	77.28	86.28	22:42
Daneborg	DNB	74.30	339.78	75.18	79.74	23:12
Ittoqqortoorm	SCO	70.48	338.03	71.60	72.61	23:45
Tasiilaq	AMK	65.60	322.37	69.23	54.07	1:18
MAGIC-1 North	MCN	73.93	322.38	77.42	64.42	0:29
MAGIC-1 East	MCE	72.40	326.10	75.38	65.08	0:25
MAGIC-1 West	MCW	72.00	317.41	76.44	56.00	1:10
MAGIC-1 GISP	MCG	72.57	321.55	76.29	61.10	0:45
MAGIC-2 Raven	MCR	66.48	313.71	71.70	45.87	1:58
Antarctica						
AGO P1	P1	-83.86	129.61	-80.10	17.50	3:43
AGO P2	P2	-85.67	313.62	-69.81	19.72	3:28
AGO P3	P3	-82.50	30.00	-71.76	41.44	1:58
AGO P4	P4	-82.01	96.76	-79.92	42.08	1:58
AGO P5	P5	-77.23	123.51	-86.69	30.77	2:48
AGO P6	P6	-72.07	127.87	-87.77	212.31	14:41
McMurdo	MM	-77.85	166.67	-79.97	327.45	6:57
South Pole	SP	-90.00	0.00	-73.99	18.89	3:35

2.2 Method of Analysis

2.2.1 Magnetometer Data Analysis

Throughout this Chapter, H, D, and Z are used to designate local geomagnetic (LGM) coordinate directions: H for south-north (magnetic field increase northward), D for west-east (field increase eastward), and Z for vertical (increases in field corresponding to changes downward in the northern hemisphere and upward in the southern hemisphere). Usually, raw data from magnetometer observations are obtained in the LGM coordinate system. On the other hand, corrected geomagnetic (CGM) coordinates are used in the following analysis. The translation from LGM coordinates to CGM coordinates is performed via geographic (GEO) coordinates. The declination angle, θ_D , is used to translate from LGM to GEO, and the oval angle, θ_O , is used to translate from GEO to CGM. The declination angle is defined as the angle between the directions to the GEO pole and the LGM pole, and the oval angle is defined as the angle between the directions to the GEO pole and the CGM pole. Oval and declination angles increase eastward (westward) in the northern (southern) hemisphere from the GEO pole direction defined as zero degrees. The translation from LGM to CGM is given by the relation

$$\begin{pmatrix} Y \\ X \end{pmatrix} = \begin{pmatrix} \cos(\theta_D - \theta_O) & -\sin(\theta_D - \theta_O) \\ \sin(\theta_D - \theta_O) & \cos(\theta_D - \theta_O) \end{pmatrix} \begin{pmatrix} D \\ H \end{pmatrix}, \quad (2.1)$$

where X and Y are the northward and eastward components in the CGM coordinate system, respectively. Description and software of the CGM coordinate system are available from the web site of Goddard Space Flight Center (<http://nssdc.gsfc.nasa.gov/space/cgm/cgm.html>).

As suggested by *Fukushima* [1976], it can be assumed that ground level magnetic field perturbation caused by field-aligned currents is the same as that caused by ionospheric Hall current when the ionospheric conductivity is horizontally uniform. Based on this *Fukushima's* [1976] theorem, the horizontal component of ground level magnetic field perturbation is rotated by 90° to provide the direction of ionospheric plasma convection. In order to extract the signal of interest, running-averaged time series with a 30 min window is subtracted from each component in advance.

2.2.2 Solar Wind Data Analysis

A normal vector of an IMF discontinuity is a clue to distinguish the property of the discontinuity. For example, tangential discontinuities (TDs) do not have a normal component of the magnetic field, whereas rotational discontinuities (RDs) do. Inversely speaking, it is worthwhile to note that the normal vector of a TD is simply deduced by a cross product of magnetic fields immediately upstream and downstream of the TD. On the other hand, the normal vector is a necessary element to estimate the Earth's arrival time of the discontinuity. For example, assuming a tilted plane with the normal vector \mathbf{n} , when it is propagating at the constant velocity \mathbf{V} , the time lag τ from an observation point \mathbf{r}_0 to a location \mathbf{r} is given as

$$\tau = \frac{(\mathbf{r} - \mathbf{r}_0) \cdot \mathbf{n}}{\mathbf{V} \cdot \mathbf{n}}. \quad (2.2)$$

The signal transmission typically takes 4-8 min from the bow shock to the magnetopause, assuming that the propagation speed is $V/8$ and the travel path in the magnetosheath is $3 R_E$. It also takes additional 1-2 min propagation from the magnetosphere to the ionosphere with an Alfvén speed of 1000 km/s and a magnetic field line length of 10-20 R_E . These parametric estimations are essentially based on the method of *Lockwood et al.* [1989] and references therein.

Minimum variance analysis (MVA) is generally applied to IMF discontinuities to provide the normal vector \mathbf{n} of the discontinuity plane by computing the minimum value of the standard deviation, σ , of the magnetic field component in that direction [*Sonnerup and Cahill*, 1967];

$$\sigma^2 = \frac{1}{K} \sum_{k=1}^K [\mathbf{B}_k \cdot \mathbf{n} - \langle \mathbf{B} \rangle \cdot \mathbf{n}]^2, \quad (2.3)$$

where \mathbf{B}_k is the k-th vector field measurement and $\langle \mathbf{B} \rangle$ is the average vector defined by

$$\langle \mathbf{B} \rangle \equiv \frac{1}{K} \sum_{k=1}^K \mathbf{B}_k. \quad (2.4)$$

Minimizing the value of the standard deviation is equivalent to finding the smallest eigenvalue, λ_{\min} , of the covariant matrix defined by

$$\mathbf{M}_{ij} \equiv \langle \mathbf{B}_i \mathbf{B}_j \rangle - \langle \mathbf{B}_i \rangle \langle \mathbf{B}_j \rangle, \quad (2.5)$$

where subscripts $i, j = 1, 2, 3$ denote Cartesian components. The eigenvalues $\lambda_{\min}, \lambda_{\text{int}}, \lambda_{\max}$ are given here in order of increasing magnitude. A cutoff ratio of the intermediate to the minimum eigenvalues $\lambda_{\text{int}} / \lambda_{\min} > 2$ is used in this study to avoid bad estimation.

2.3 Results

2.3.1 Geomagnetic Disturbances

Differences found in the amplitude and phase of magnetic perturbations observed at a pair of interhemispheric magnetically conjugate magnetometer stations provide important information for understanding the coupling processes working between the magnetosphere and the ionosphere. In **Figure 2.2**, geomagnetic perturbations obtained from magnetically conjugate pairs of northern and southern fluxgate magnetometers are shown with black and red lines, respectively. Conjugate magnetometer data are available at Taloyoak (TAL) and MM, Iqaluit (IQ) and SP, and Kangerlussuaq (STF) and AGO P3 on the May 22, 1996 event, as shown in **Figure 2.1**. The X and Y components are defined as the northward and eastward components in CGM coordinates, and the Z component is defined as the vertical downward component in the northern hemisphere and the vertical upward component in the southern hemisphere. A magnetic impulse event started at ~1310 UT has a peak-to-peak amplitude of more than 100 nT in the three components at SP. A similar feature is also observed at IQ with almost the same duration and amplitude. In the Z component at SP, a positive pulse at 1312 UT, a negative pulse at 1315 UT, and a positive pulse at 1323 UT can be interpreted as traveling Hall current loops accompanied with downward, upward, and downward field-aligned currents, respectively. TAL and MM are located $\sim 6^\circ$ poleward and ~ 3 MLT (magnetic local time) downstream of the TCV propagation from IQ and SP, as shown in **Figure 2.1**. The solitary signature of TCVs is not clear in these stations anymore, implying the localized characteristics of the TCVs. STF and P3 are located $\sim 1^\circ$ equatorward and ~ 1.5 MLT upstream of the TCV propagation from IQ and SP. The X-component perturbations are in phase, while the Y-component perturbations are out of phase for STF and P3. This relationship in the horizontal components is similar to that of IQ and SP. The Z-component perturbations are clearly out of phase for STF and P3 data, while in phase and out of phase relationship are mixed for perturbations at IQ and SP.

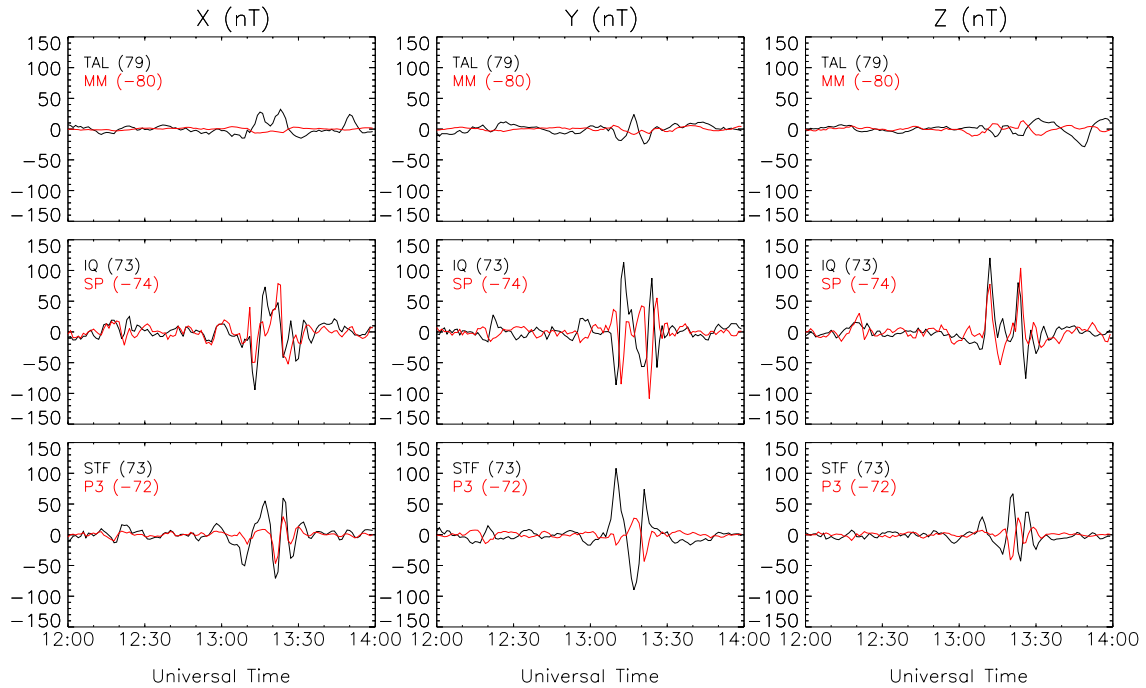


Figure 2.2. Fluxgate magnetometer data obtained at conjugate magnetometers in northern (black) and southern (red) hemispheres. The CGM latitude for each station is shown in parentheses. Running averaged time series with a 30 min window is subtracted from each data to extract the signal of interest. The locations of these conjugate pairs of stations are shown in **Figure 2.1**.

Applying the magnetometer data analysis described in **Section 2.2.1**, convection patterns for the May 22 event are shown in **Figure 2.3**. Roughly, a clockwise (counterclockwise) convection vortex is interpreted as field-aligned currents flowing into (out of) the ionosphere in both northern and southern hemispheres. It is shown that at 1310 UT in the northern hemisphere, a two-cell convection pattern appeared, with a counterclockwise vortex in the 8-12 MLT sector and a clockwise vortex in the 12-15 MLT sector. In addition, a strong poleward and duskward flow occurred around local magnetic noon at 73°-80° CGM latitudes (MLAT). This flow changed its direction to equatorward and dawnward at 1316 UT, resulting in a reversed two-cell convection pattern in the 10-14 MLT sector at 1318 UT. The guiding center of TCVs moved westward at 70°-75° MLAT in the dawn to noon sector during the interval 1310-1318 UT. The averaged speed of the guiding center motion is 3-5 km/s at ionospheric altitude. The northern and southern convection patterns are essentially identical. The amplitudes of the magnetic perturbations, however, are small in the southern hemisphere, except for comparable magnetic perturbations at SP and IQ, which are both close to the guiding center of the TCVs.

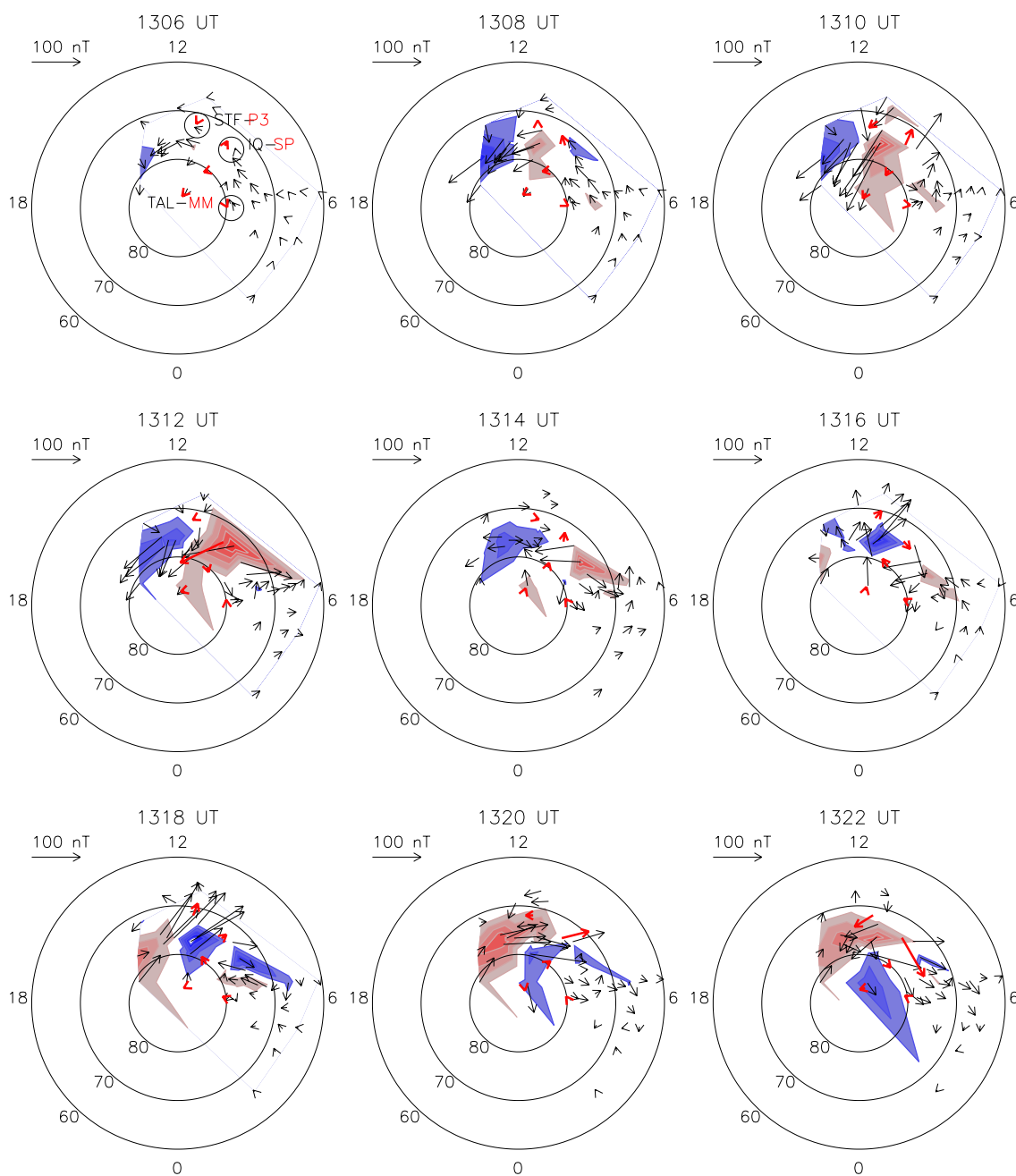


Figure 2.3. Convection patterns in CGM coordinates for the time interval 1306-1322 UT on May 22, 1996. The lengths of arrows are expressed in nT. Thick red arrows represent flow vectors obtained from magnetometer data in the southern hemisphere. Red and blue contours mean the regions with positive and negative values of the Z component in the northern hemisphere, respectively. The contour interval is 20 nT without zero contour lines.

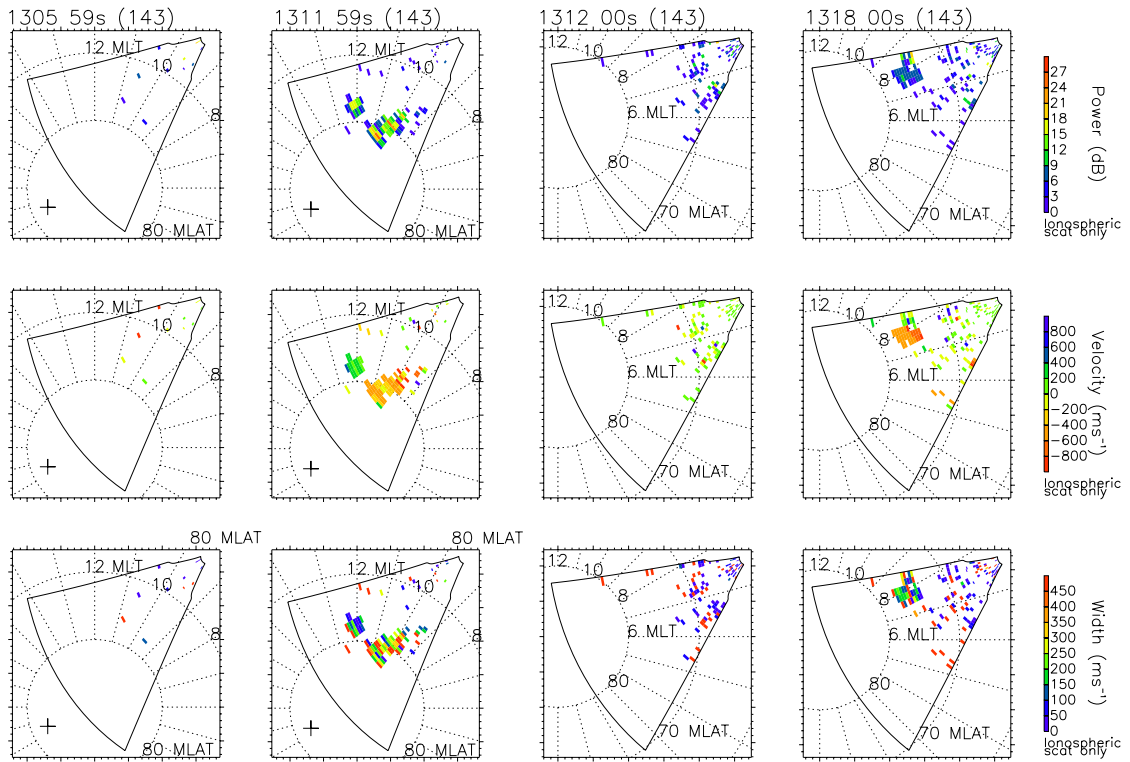


Figure 2.4. Backscatter power (top), Doppler line-of-sight velocity (middle), and spectral width (bottom) obtained from HF radars at Goose Bay (left two columns) and Kapuskasing (right two columns) in the northern hemisphere on May 22, 1996. The fields-of-view of the HF radars are shown by solid lines.

2.3.2 Ionospheric Disturbances

Figure 2.4 shows the distributions of backscatter power, Doppler line-of-sight velocity, and spectral width measured by SuperDARN on May 22, 1996. Positive (negative) velocities represent irregularity toward (away from) the radars. From **Figure 2.4**, it is found that the TCVs are accompanied by localized backscatter regions, named as "backscatter blobs" hereafter, in the sunlit northern hemisphere. The backscatter blobs convected along with the tailward bulk motion of TCVs across three fields-of-view of HF radars for ten minutes. At 1312-1314 UT, the backscatter blob first appeared in the 10-12 MLT and 75°-85° MLAT sector in the field-of-view of the Goose Bay radar, as shown in the left two columns of **Figure 2.4**. At 1318-1320 UT, the backscatter blob reached to the 7-9 MLT and 74°-77° MLAT sector in the field-of-view of the Kapuskasing radar, as shown in the right two columns of **Figure 2.4**. After these periods, the backscatter blobs decayed in the overlapped fields-of-view of the Kapuskasing-Saskatoon pair radars. From the comparison between **Figure 2.3** and **Figure 2.4**, it is concluded that these backscatter blobs located near the leading edge of the upward field-aligned current.

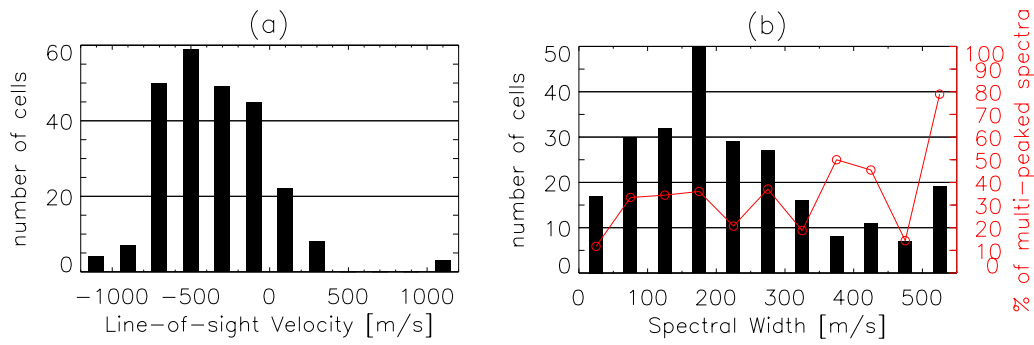


Figure 2.5. Histograms of the number of beam-range cells for (a) Doppler line-of-sight velocity and (b) Doppler spectral width within TCV-related backscatter regions. Percentages of the multi-peaked spectra are superposed with red lines and circles in the right panels. Sample duration is 1312-1322 UT on May 22, 1996.

The spectral characteristics of backscatter blobs are investigated in detail. As shown in **Figure 2.5**, the histograms of the number of radar beam-range cells are constructed for the ranges of Doppler line-of-sight velocities and spectral widths within the backscatter blob. The time interval used to construct the histograms is 1312-1322 UT. Since the backscatter blobs traveled across the three fields-of-view of HF radars, counts are added for all three radars. **Figure 2.5a** shows that Doppler line-of-sight velocities are almost unidirectional, mostly distributed around 400-600 m/s with flow directions away from the radar for this period. On the other hand, **Figure 2.5b** shows that the Doppler spectral width of backscatter is broadly distributed mainly in the range of 50-300 m/s, but sometimes over 400 m/s. The spectral forms of these backscatters during the time interval 1312-1322 UT are investigated in more detail. Although single-peaked spectra are dominant, multi-peaked spectra are found occasionally. Now the ‘multi-peaked spectrum’ is defined in this study as a spectrum that is composed of multiple distinct peaks clearly separated each other. Representative examples of multi-peaked spectral forms are shown by *Kataoka et al.* [2003]. Percentages of the multi-peaked spectra are represented with open circles connected with solid lines in **Figure 2.5b**. Note that the multi-peaked spectral occurrence is significantly enhanced up to 80% in the range of extremely broad (>500 m/s) spectral widths.

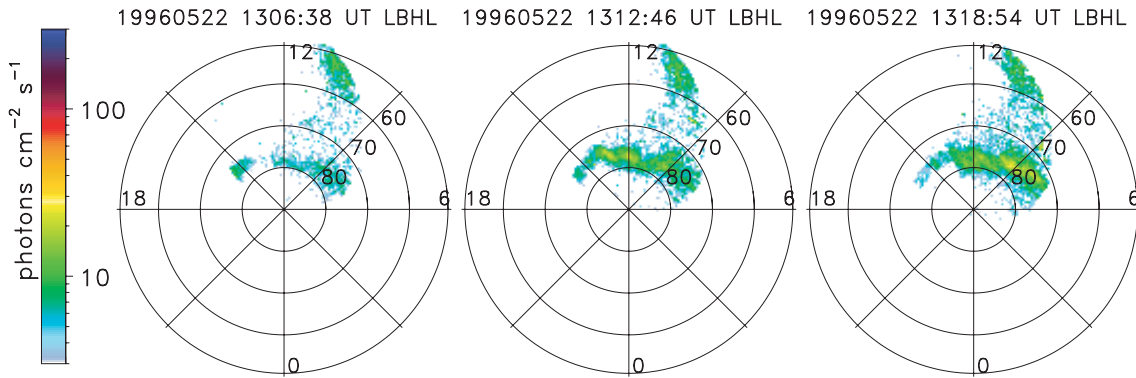


Figure 2.6. POLAR UVI LBHL observations of aurora from 1306:38 UT to 1318:54 UT on May 22, 1996. Magnetic local noon is at the top of each image, and dawn is to the right. CGM latitudinal circles are drawn at 50°, 60°, 70°, and 80°.

2.3.3 Auroral Dynamics

POLAR observations of the May 22 event are shown in **Figure 2.6**. The UVI instrument has a wobble of ~ 10 pixels and this affects the resolution of the image in the directions of the wobble. In the May 22, 1996 images, the wobble is roughly in the 15-3 MLT direction, and the wobble effect does not affect the result and discussion in this study. Transient UV auroral enhancements appeared around noon at 1312:46 UT and moved westward (to the 8-10 MLT sector) in the next frame at 1318:54 UT. From a comparison between **Figure 2.6** and **Figure 2.3**, auroral enhancements are found to be relatively strong in the clockwise vortex associated with the upward field-aligned current. The convection flow does not correspond to the auroral motion, although the auroral motion corresponds to the propagation velocity of TCVs themselves. Localized UV aurora with similar properties was reported by *Sitar et al.* [1998] for the TCVs associated with a hot flow anomaly (HFA) event on July 24, 1996. Also, backscatter blobs overlapped on the poleward and westward sides of the transient aurora as shown in **Figures 2.4**. In summary, clockwise vortex, negative Z values, UV aurora, and backscatter blob are nearly colocated, implying the relationship with the upward field-aligned current.

Mende et al. [2001] investigated ground-based all-sky auroral images in Antarctica for the May 22 event in detail. During the TCV interval 1310-1330 UT around the SP station, short-lived dayside auroral activity was observed equatorward of the quiescent auroral oval. This is important observational evidence showing that the field-aligned currents driving the TCVs are excited in the closed field line region. Also, small-scale (~ 10 km) spatial morphology of electron precipitation was confirmed for auroral emissions at the wavelengths of both 427.8 nm and 630.0 nm by *Mende et al.* [2001]. The existence of 427.8 nm emission means the hard electron precipitation of keV order, suggesting that local electron acceleration occurred. The 427.8 nm emission was observed concurrently with the passage of upward field-aligned current at 1316 UT. In association with

large-amplitude TCVs, localized 427.8 nm emission with very similar properties was also reported by *Murr et al.* [2002]. They showed that the electron precipitation causing 427.8 nm emission carries reasonable field-aligned currents.

2.3.4 Interplanetary Conditions

Figure 2.7 shows data of solar wind observations for the time interval 1100-1500 UT on May 22, 1996. A rapid northward turning of the IMF Bz and a dynamic pressure enhancement are found at the time corresponding to the onset of this TCV, at 1255 UT on Wind at GSE $(x, y, z) = (124.1, -24.2, -6.5)$ and at 1244 UT on Geotail at GSE $(x, y, z) = (26.3, 10.6, -3.4)$. Note that the discontinuity occurred at Geotail ~11 min before it was observed at Wind. This curious time delay can be explained by the three-dimensional inclination of the discontinuity plane. The solar wind speed was almost stable at 420-440 km/s.

In the May 22 event, Wind, IMP8, Interball, and Geotail observed similar discontinuities as a possible source of the TCV event as shown in the bottom three panels of **Figure 2.7**. The normal vectors of the discontinuities associated with northward IMF turnings can be calculated at different satellite locations with an assumption of TDs. The result is shown in **Table 2.3**, and visualized in **Figure 2.8**. Since solar wind data from four different satellites are fortunately available, the normal vector is also calculated as

$$\mathbf{n}_4 = \frac{(\mathbf{V}_{12} - \mathbf{V}_{13}) \times (\mathbf{V}_{12} - \mathbf{V}_{14})}{|(\mathbf{V}_{12} - \mathbf{V}_{13}) \times (\mathbf{V}_{12} - \mathbf{V}_{14})|}, \quad \mathbf{V}_{ij} = \mathbf{R}_{ij} / T_{ij}, \quad (2.6)$$

where \mathbf{R}_{ij} is the vector connecting satellite i and satellite j, and T_{ij} is the time lag from satellite i to satellite j. Taking the Wind satellite as the satellite 1, \mathbf{n}_4 is calculated as GSE $(x, y, z) = (-0.17, -0.85, 0.51)$. All \mathbf{n}_{TD} vectors are close to the \mathbf{n}_4 vector with only a small difference between the \mathbf{n}_{TD} direction and the \mathbf{n}_4 direction (within $\sim 20^\circ$). It is also seen from the results in **Table 2.3** that \mathbf{n}_{MVA} derived from the MVA method using Wind high time resolution (3 s) data is almost identical to \mathbf{n}_{TD} at Wind. From these results, it is concluded that this discontinuity is identified as a TD.

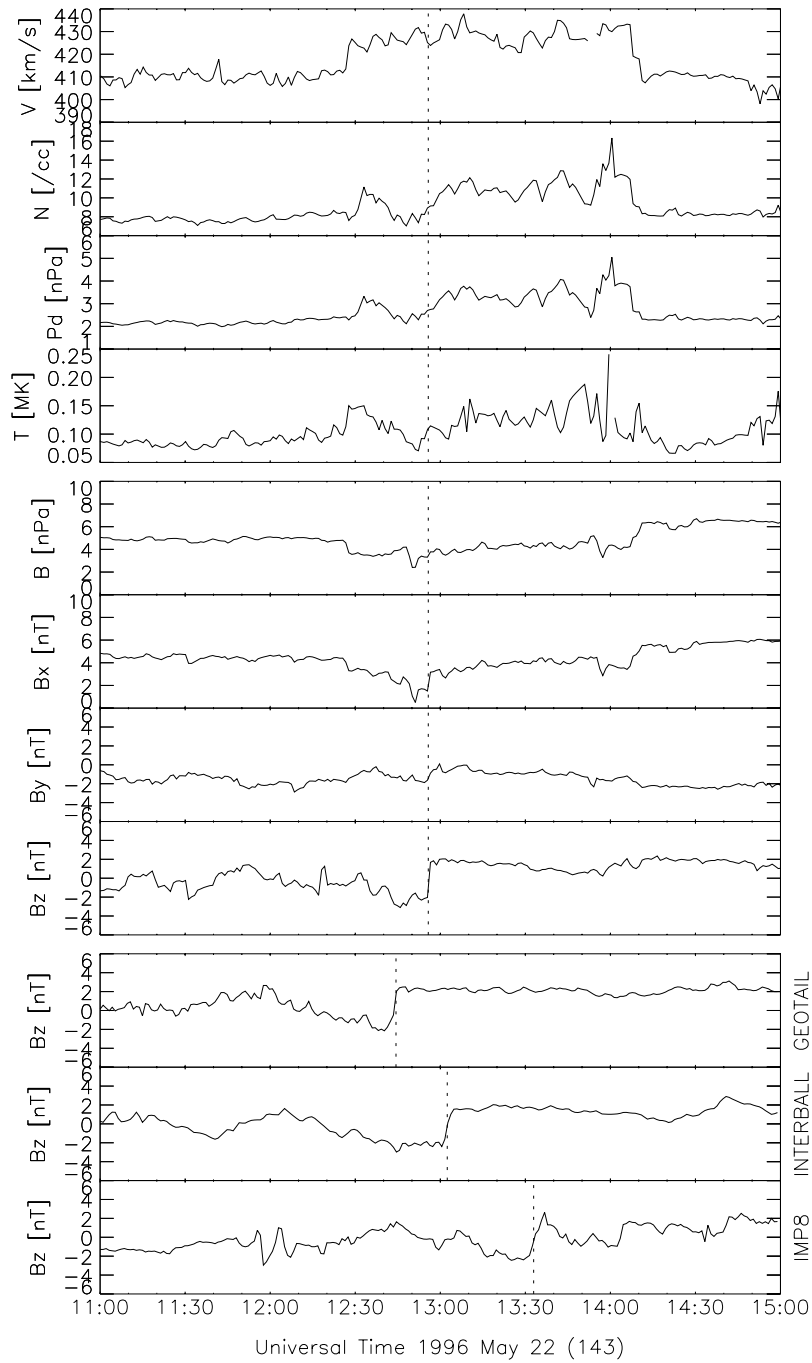


Figure 2.7. Solar wind data for the time interval 1100-1500 UT on 22 May 1996. Top four panels show solar wind bulk speed (km/s), proton density (/cc), dynamic pressure (nPa), and proton temperature (MK) measured by the Wind satellite. Middle four panels show the total IMF, Bx, By, and Bz components (nT) in GSE coordinates measured by the Wind satellite. Bottom three panels show the IMF Bz component (nT) in GSE coordinates measured by Geotail, Interball, and IMP8. Dotted lines indicate the arrival time of an IMF discontinuity analyzed in Section 2.3.4.

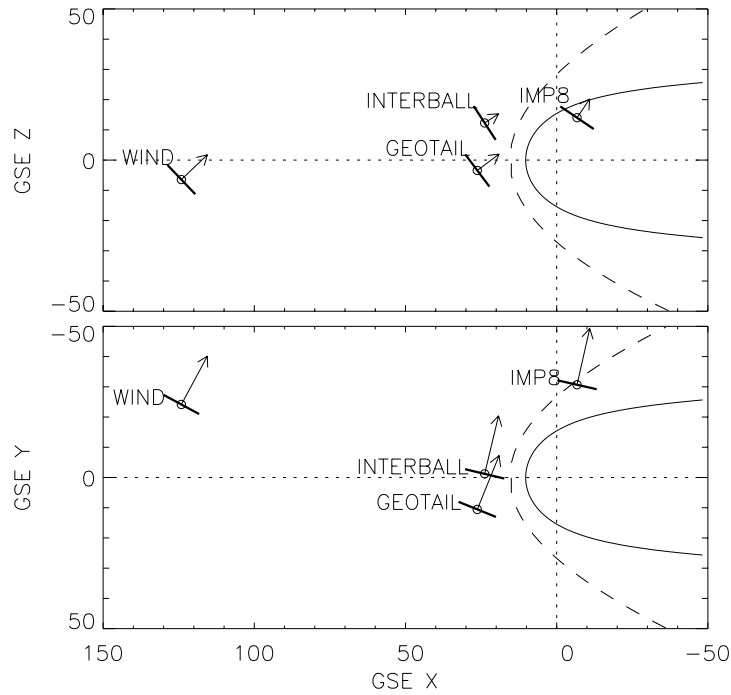


Figure 2.8. Normal vectors (arrows) and front planes (thick lines) of the IMF discontinuity estimated at four satellite locations in GSE X-Z coordinates (top) and GSE X-Y coordinates (bottom). The Earth's magnetopause and bow shock are depicted by solid and dashed lines, respectively. The magnetopause model used here is from *Shue et al.* [1998] for 2.0 nPa and zero IMF condition. The bow shock model used here is from *Peredo et al.* [1995] for Alfvén Mach number between 13 and 20, ignoring any IMF effects.

Table 2.3. Arrival times and normal vectors in GSE coordinates for the IMF discontinuity estimated at four satellite locations.

Satellite	Method	Time (UT)	Normal Vector in GSE
Wind	MVA	1255.46	(-0.43, -0.85, 0.29)
Wind	TD	1255.46	(-0.43, -0.80, 0.41)
Geotail	TD	1244.23	(-0.36, -0.95, 0.13)
Interball	TD	1302.27	(-0.23, -0.96, 0.15)
IMP8	TD	1332.56	(-0.21, -0.93, 0.31)

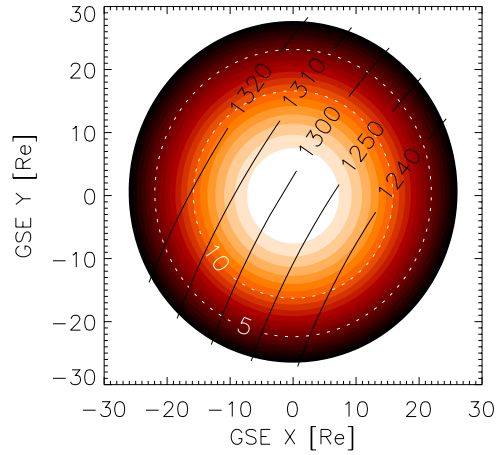


Figure 2.9. Intersection of the tangential discontinuity (black lines) and the bow shock at 10-min intervals in GSE Y-Z coordinates for 1240-1320 UT on May 22, 1996. The bow shock surface is colored in gradational red from zero GSE X (black) to the bow shock nose (white). White dotted contour lines also indicate the GSE X component (in R_E) of the bow shock surface.

Figure 2.9 show the intersection of the TD with the bow shock surface for the May 22 event. The bow shock model used here is from *Peredo et al.* [1995] for Alfvén Mach number between 13 and 20, ignoring any IMF effects. The arrival time of the TD is calculated using the \mathbf{n}_4 and the equation (2.2). For simplicity, the solar wind velocity is fixed as $(-420, 0, 0)$ km/s. From **Figure 2.9**, it is concluded that the Earth’s arrival time of this TD is proper for the cause of this TCV event, even taking into account the transition time from the bow shock to the magnetosphere, and from the magnetosphere to the ionosphere as described in **Section 2.2.2**.

2.4 Discussion

2.4.1 F region Plasma Irregularity

The plasma instability is a key process to produce ionospheric plasma irregularities necessary for HF radar backscatter. It is discussed what kind of instability process can occur inside the transient backscatter blobs. The first concern is the unidirectional line-of-sight Doppler velocity distribution in **Figure 2.5a**. This unidirectional distribution may suggest that the plasma flow direction controls the growth of instability. Since the gradient drift instability (GDI) occurs when the direction of the plasma drift is in the same direction to the background density gradient, this instability is a plausible candidate for the generation of irregularities inside the blobs. Note that plasma velocity inside the blob is predominantly away from the radar. Combining two-dimensional patterns of convection flow directions obtained by magnetometers (see **Figure 2.3**), the velocity vectors should be directed poleward and/or eastward. In that case, the background density gradient vector must be directed poleward and/or eastward to amplify the instability. According to the IRI-90 model [*Bilitza, 1990*], the background density gradient produced by a sunlit effect is directed nearly eastward (with an increase of $\sim 0.2 \times 10^5$ / cc per 2.0 MLT at 300 km altitudes) in the high-latitude prenoon sector. However, this background density gradient alone is too small to produce GDI as discussed below. Another plausible candidate to produce localized and strong density gradient is the F region density wake structure of TCVs. The TCV wake can produce a strong poleward density gradient in the high-latitude portion of the TCV current system. From an ionospheric simulation, *Schunk et al.* [1994] showed that localized temperature enhancement and electron density depression occur in the TCV wake structure when the maximum convection electric field is 100 mV/m corresponding to a drift velocity of 2 km/s. *Valladares et al.* [1999] showed the incoherent scatter radar signature of density depression by a factor of two at F region altitudes during a TCV event with magnetic perturbations larger than 100 nT. Both authors indicated that the O^+ recombination due to strong electric field causes density depression via enhanced frictional heating [*Schunk et al., 1975*].

The second concern is how large electric field or plasma flow speed is needed for a significant density depression in the TCV wake structure via O^+ recombination with N_2 . The reaction rate k_1 of O^+ with N_2 was given by *St.-Maurice and Laneville* [1998] as a function of an effective temperature T_{eff} for the reaction below.



The value of T_{eff} is given by the expression,

$$T_{eff} = \frac{m_n}{m_i + m_n} \left(\frac{m_i U^2}{3k_B} + T_i - T_n \right) + T_n, \quad (2.8)$$

where m_n and m_i are the masses of neutral and ion reactants, respectively, k_B is the Boltzmann

constant, T_i and T_n are the ion and neutral temperatures, respectively, and U is the magnitude of the relative velocity between ion and neutral motions. The ion temperature due to ion frictional heating above the 200 km altitude is given by [e.g., *Schunk et al.*, 1975]

$$T_i = T_n + \frac{m_a U^2}{3k_B}, \quad (2.9)$$

where m_a is the mass of the ambient gas. Assume an ambient gas consisting of atomic oxygen, and the effective temperature for O^+ recombination with N_2 is given by $T_{eff} = T_n + 8.2 \times 10^4 U^2$. Assume that any production and transport terms in the continuity equation remain in a steady state, and that the loss term alone has an effect on the density depression because of its time constant. Then an approximate relation of the density depression rate α is formulated as

$$\alpha = \frac{\delta[O^+]}{[O^+]} = (k1(T_{eff}) - k1(T_n))[N_2]\delta t, \quad (2.10)$$

where $[N_2]$, $[O^+]$, and $\delta[O^+]$ are the number densities of nitrogen, oxygen ion, and its fluctuation during the time of δt . We choose $\delta t = 10^2$ s as a typical time for TCV transients.

The one dimensional GDI growth rate is given by *Linson and Workman* [1970] as

$$\gamma_{GDI} = \frac{U}{L}, \quad (2.11)$$

where L is the scale length of the plasma density gradient, i.e., $L = n / |\nabla n|$. It is expected that the GDI growth rate would be huge because the backscatter blobs suddenly appeared with the TCV timing as shown in **Figure 2.4**. Such a huge growth rate allows us to use an instantaneous GDI growth rate for correct estimation, nevertheless the history of plasma along the streamline should be considered in general [*Sojka et al.*, 2000]. In order to accomplish GDI during TCV duration, the growth rate γ_{GDI} would be larger than at least 10^{-3} s⁻¹. If the created density slope has a scale of 10^2 km, $U\alpha$ should be larger than 10^{-1} km/s.

The density depression rate is plotted as a function of U with a solid curve in **Figure 2.10**. With typical values from the MSISE-90 model [*Hedin*, 1991] under sunlit high latitude conditions at 300 km altitude ($[N_2] = 10^8$ cm⁻³ and $T_n = 800$ K), it is found that the relative velocity between ion and neutral species, U , is needed at least 1.7 km/s for producing GDI at this condition. Also, an effect on density depression due to convection flow less than 1.0 km/s is negligible (<1%). In **Figure 2.5a**, it is shown that the Doppler velocity is typically distributed in the range 400-600 m/s. It is clear from the **Figure 2.10** that the observed flow speed is too slow to meet the criteria. Also, it is expected that the velocity of 400-600 m/s is not significantly underestimated as an actual velocity because convection patterns derived from magnetometers imply almost the north-south aligned velocity as shown in **Figure 2.3**. In this reason, it would be impossible for this one-dimensional GDI scenario alone to accomplish the formation of the TCV wake and to make the irregularities.

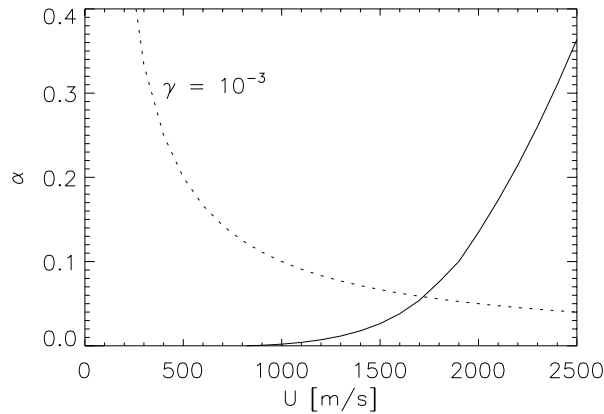


Figure 2.10. Density depression rate (solid line) and a threshold of GDI growth rate (dotted line) as a function of plasma flow velocity.

There are other possibilities to produce irregularities. In **Section 2.3.3**, it was shown that the backscatter blob is located in the poleward and westward part of transient UV aurora, and that electron precipitation is relatively strong in the upward field-aligned current region. The localized upward current distribution around the blob may have a possibility of making the density irregularities. The current convective instability (CCI), that is the three-dimensional version of GDI caused by the upward field-aligned current [*Ossakow and Chaturvedi, 1979*], could elevate the GDI growth rate significantly, compared with the one derived from the one-dimensional GDI scenario described above. Note that CCI occurs even under the stable condition for GDI. It is further speculated that the growth rate could be rapidly enhanced via some nonlinear processes such as a production of density irregularities due to structured electron precipitation themselves [*Kelley et al., 1982*], and a formation of strong background density gradient in the F region due to transient soft-electron precipitation within the TCV current system. In this scenario, observed unidirectional Doppler velocities are also explained because the motion of the irregularity region is fixed under a portion of the TCV current system where the growth rate is maximized. From the discussion above, it is concluded that the transient backscatter blob would not be produced by one-dimensional GDI process but by the three-dimensional GDI process through the nonlinear rapid evolution of instabilities in the upward field-aligned current region.

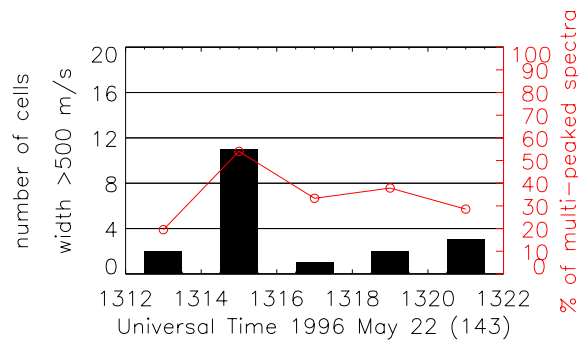


Figure 2.11. Histograms of the number of beam-range cells for extremely broad spectral width. Percentages of the multi-peaked spectra are superposed with red lines and circles.

2.4.2 Spectral Width Enhancement

Another unsolved problem in the ionospheric response of the TCVs is the occurrence of multi-peaked Doppler spectra in the localized backscatter blob accompanying the TCVs. What is the cause of multi-peaked spectral forms and large increases in spectral widths? The Doppler spectral width is a measure of the variation of electric field in both the spatial domain corresponding to the radar sampling cell (typically 45 km by 100 km in dimension) and the time domain corresponding to the radar integration time of 7 s. A large increase in the spectral width indicates that the electric field has varied rapidly in one or both of these two domains. **Figure 2.11** summarizes the temporal evolution of multi-peaked spectra and extremely broad spectral widths for the May 22 event. Most of these multi-peaked spectra and extremely broad spectral widths are found to be observed for the single scan period of 1314-1316 UT.

A possible source for making the short-lived, extremely broad spectral width is Pc 1-2 bursts because Pc 1-2 bursts are closely correlated with TCVs [e.g., *Sato et al.*, 1999; *Fukunishi et al.*, 2002]. *Kataoka et al.* [2001] found the occurrence of a pronounced increase in the Doppler spectral width when a TCV passed through the irregularity region associated with the TCV event on June 6, 1997. *Andre et al.* [1999, 2000] have evaluated the impact of time-varying electric field on the spectral width as seen by SuperDARN. Even though the scenario of *Andre et al.* [1999, 2000] can explain how Pc 1-2 bursts make transient broad spectral widths and multi-peaked spectra, there has been no report so far on simultaneous occurrences of Pc 1-2 burst and backscatter with broad spectral widths. In this scope, search-coil magnetometer data are also analyzed for checking occurrences of Pc 1-2 burst during the TCVs.

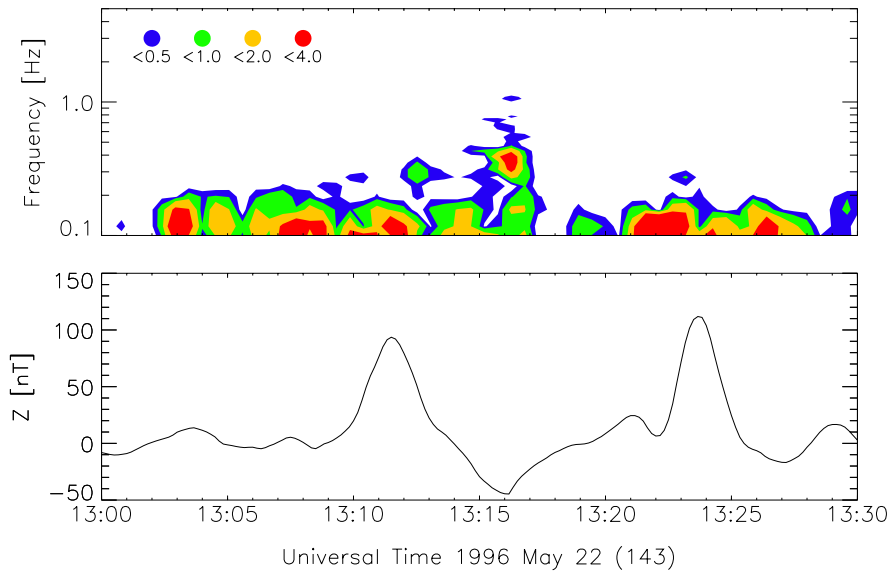


Figure 2.12. Dynamic cross-spectrum using data obtained from search-coil magnetometer at SP (top). The cross-spectral power is normalized by $N/(2\sigma^2)$, where $N = 256$ is the number of points of the window interval, and $\sigma^2 = \sigma_x^2 + \sigma_y^2 = 0.022 \text{ (nT/s)}^2$ is the variance of the horizontal components for this 30 min interval. Colored contours are at the normalized power of 0.5, 1.0, 2.0, and 4.0. Geomagnetic perturbations in the Z-component obtained from fluxgate magnetometer at SP are also shown for comparison (bottom).

In order to investigate Pc 1-2 wave activity during the May 22 event, a time-frequency analysis based on the Fast Fourier Transform is performed using the search-coil magnetometer data obtained in Antarctica. To extract activity of Pc 1-2 band in the frequency range of 0.1 Hz - 5.0 Hz, dynamic spectrum analysis is conducted using a Hanning window and by a sliding one forth of the window interval. The activity of Pc 1-2 band is clearly enhanced at SP station in association with the passage of the TCV. **Figure 2.12** shows dynamic cross-spectrum of the horizontal components in the frequency range from 0.1 Hz to 5.0 Hz. After subtracting 12.8 s running average, a 25.6 s window is selected for 10.0 Hz sampling search-coil magnetometers at SP. A Pc1-2 burst is observed for the time interval 1315-1317 UT. A peak is found in the cross-spectral power between 0.3 and 0.4 Hz. The bottom panel enlarges perturbations in the Z-component to indicate the polarity of field-aligned currents. From a comparison of the two panels, it is speculated that Pc 1-2 burst occurred concurrently with an upward field-aligned current filament associated with the TCV. From a comparison between **Figure 2.11** and **Figure 2.12**, it is expected that Pc 1-2 burst and enhancement in the Doppler spectral width is closely related. This observational result supports the scenario of *Andre et al.* [1999, 2000]. No distinct Pc 1-2 band activity was observed at P1 and P5. The spectral analysis using search-coil magnetometer data can not be performed for MM and P3 because of bad data quality due to a lot of noise spikes on the May 22 event.

It is worthwhile to note here that the distribution profiles of spectral width in **Figure 2.5b** have some similarities to the histograms obtained in the low-latitude boundary layer region by *Baker et al.*

[1995]. *Andre et al.* [2000] also showed from a simulation study that the spectral width in the velocity gradient region is enhanced as large as ~ 250 m/s. Combining the discussion above, it is concluded that the distributions of spectral width shown in **Figure 2.5b** would be produced by two sources. One is the velocity gradient structure of vortices themselves, which produces a gradual background distribution from 50 to 300 m/s. Another source is the time-varying electric field, which enhances the spectral width more than 400 m/s when Pc 1-2 burst exists.

2.4.3 Generation Mechanism

What processes do determine the location and motion of TCVs? Why can only particular TDs trigger TCVs? These are the most fundamental questions for investigating the generation mechanism of TCVs. Bearing in mind that the source of the TCV event on July 24, 1996 is identified as a HFA [*Sibeck et al.*, 1999], a possibility of the HFA formation and overall consistency are investigated in detail. It is assumed that all the spacecraft were not at the right time and right place to identify the HFA because there is no direct observational evidence for the occurrence of HFA on the May 22 event. This assumption becomes reasonable later in terms of the spacecraft locations as shown in **Figure 2.8**. Firstly, in order to investigate whether the HFA is a possible source for the TCV event on May 22, 1996, a geometric relation between the TD and the bow shock is evaluated.

There are at least two criteria for producing HFAs at the bow shock. The first criterion concerns the transit speed of TD along the bow shock. The kinetic description of a HFA creation suggest that the intersection of the current sheet with the bow shock must move sufficiently slowly along the bow shock so that reflected ions remain close to and interact with the current sheet of TD. A requirement for TDs whose normal vectors have large cone angles ($>60^\circ$) with small normalized transit velocities (<0.3) has been suggested from the statistical analysis of HFAs by *Schwartz et al.* [2000]. The second criterion concerns the motional electric field (MEF) accompanying TD. TDs create HFAs when the MEF is oriented toward the TD on one or both sides of the TD. The condition of inward pointing MEF can be checked by the angle θ between the TD normal vector \mathbf{n} and the solar wind MEF vector $\mathbf{E} = -\mathbf{V} \times \mathbf{B}$ in the prior to and after TD passage, where \mathbf{B} is the magnetic field and \mathbf{V} is the solar wind velocity. Since the negative X component of \mathbf{n} is selected, the relationship for inward pointing MEF is that $\theta_{nE_pre} > 90^\circ$ and $\theta_{nE_post} < 90^\circ$.

The TD of the May 22 event has normal vectors with very large ($\sim 80^\circ$) cone angles as is shown by arrows in **Figure 2.8**. The normalized transit velocity of TD was less than 0.3 everywhere on the bow shock for at least one side of TD. This TD also satisfies the condition of inward pointing motional electric field as $\theta_{nE_pre} = 164^\circ$ and $\theta_{nE_post} = 44^\circ$. From these results, the TD satisfies the conditions for the formation and evolution of HFA at the bow shock. Similar properties are confirmed for other TCVs, e.g., May 27, 1998 event [*Kataoka et al.*, 2002] and July 24, 1996 event

[Sibeck *et al.*, 1999]. Once a HFA is formed at the bow shock, the HFA structure should move with the intersection of the TD and the bow shock [Sibeck *et al.*, 2000]. TCVs caused by HFAs will move mainly in the longitudinal direction along the azimuthal sweep motion of the intersection line. The westward motion of the TCVs on the May 22 event is consistent with the dawnward sweep motion of the intersection line as shown in **Figure 2.9**.

Snapshots of the TCVs and the expected deformations of the dayside magnetosphere at 1310 UT and 1316 UT in the May 22 event are schematically shown in **Figure 2.13**. The formation of a HFA is assumed to start near the nose of the bow shock where HFAs are preferentially formed. Possible effects of pressure pulses and bursty flows due to anti-parallel dayside reconnection are also schematically illustrated in **Figure 2.13**. Basically, HFAs and pressure pulses deform the magnetosphere outward and inward, respectively [Sibeck *et al.*, 2000]. The deformation of the magnetopause produces field-aligned currents via vortical plasma flows and/or divergence of the inertia currents in the closed boundary region as reviewed by Cowley [2000]. On the other hand, anti-parallel reconnection would work as a voltage generator to produce field-aligned currents in both open and closed field line regions via merging of the solar wind MEF into the magnetosphere [Glassmeier and Heppner, 1992].

It is worthwhile to note that the downward, upward, and downward field-aligned triplet structure at 1316 UT in **Figure 2.13** is very similar to TCVs due to the HFA on July 24, 1996 as described by Sitar *et al.* [1998]. The first pair of leading downward and trailing upward field-aligned currents observed in the noon sector at 1310 UT in **Figure 2.13** matches the two-cell convection pattern with a strong poleward flow around magnetic noon, and the second pair of leading upward and trailing downward field-aligned currents observed in the same sector at 1316 UT matches to a reversed two-cell convection pattern with a strong equatorward flow around magnetic noon. The effects of the magnetopause deformation in the closed field line region are expected to produce conjugate magnetic perturbations in the northern and southern hemispheres. In summary, all of the morphological features of the event can be explained by the HFA mechanism.

Several additional pieces of evidence support the conclusion that only the HFA mechanism can select the appropriate solar wind discontinuities for the generation of TCVs, even though there are many IMF Bz turnings or pressure pulses in the solar wind. Combining the TCV event on May 27, 1998, it can also be concluded that pressure pulses or IMF Bz turnings alone are not a sufficient condition for triggering TCVs as demonstrated by Kataoka *et al.* [2002] in detail.

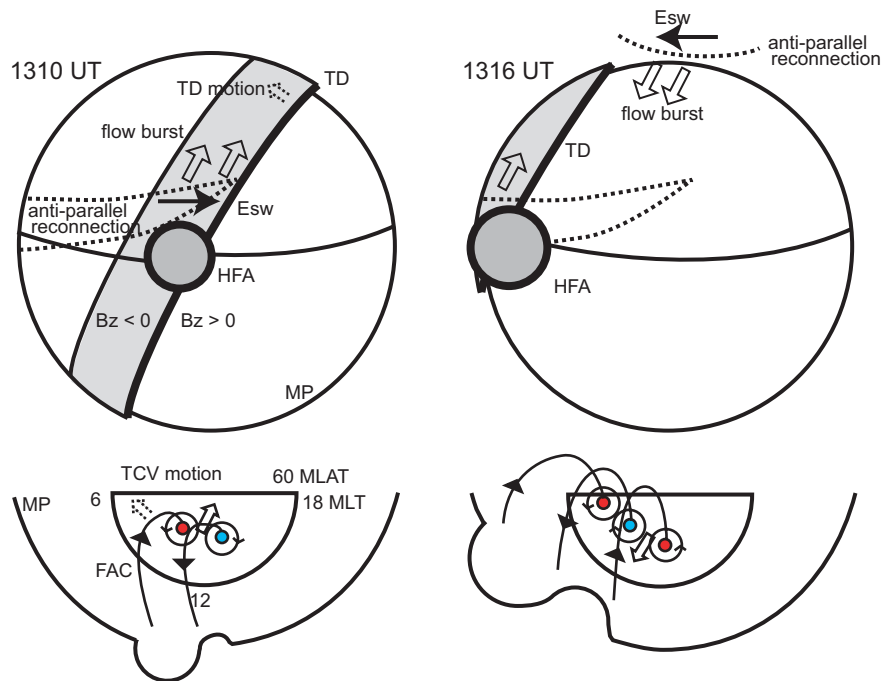


Figure 2.13. Summary sketch of TCVs and expected deformations of the dayside magnetosphere associated with the arrival of a tangential discontinuity at 1310 UT and 1316 UT on May 22, 1996. In the top diagrams, possible effects of pressure pulses and bursty flows due to antiparallel dayside reconnection are schematically illustrated by a 3D view of the dayside magnetopause. Dotted lines show the expected regions of antiparallel reconnection, and merging electric fields are denoted as Esw. In the bottom diagrams, the equatorial cut of the dayside magnetopause is depicted with field-aligned currents flowing into or out of the northern polar ionosphere. Blue and red circles represent the guiding centers of clockwise and counterclockwise vortices, respectively.

As discussed above, although magnetopause deformation due to HFA formation at the bow shock can explain all observed morphological features and the triggering process of the TCVs, it is necessary to consider the additional effects of reconnection and pressure pulses, since interplanetary TDs often accompany abrupt north-south IMF turnings and enhancements of dynamic pressure. It is worthwhile to note that a strong poleward and duskward flow around the magnetic noon meridian at 1310 UT in the May 22 event can also be interpreted as a result of bursty merging at the dayside magnetopause that is caused by a relatively strong southward and dawnward IMF observed several min before the TD passage. The average values of IMF in this interval is approximately GSE $(B_x, B_y, B_z) = (2.0, -1.5, -2.0)$ nT. Considering the topology of the anti-parallel reconnection, both flow bursts and magnetic tension caused by the dayside reconnection should be directed poleward and duskward in the northern magnetopause (see **Figure 2.13**).

On the other hand, the reversed two-cell convection pattern with an equatorward flow around magnetic noon at 1316 UT may also be interpreted as a bursty flow due to high-latitude reconnection caused by a rapid northward IMF turning (~ 2 nT) after the TD passage. Since the change of the

large-scale convection pattern propagates tailward on a similar time scale (4-13 min) and with a propagation velocity at ~ 1.5 MLT/min [see *Murr and Hughes*, 2001], the transition of the large-scale convection pattern itself could become the TCVs.

Dotted lines in **Figure 2.13** show the expected regions of anti-parallel reconnection inferred from the criterion of *Rodger et al.* [2000] under the IMF conditions of southward B_z and negative B_y in summer solstice. It is also expected that the first pair of leading downward and trailing upward field-aligned currents derived from the northern magnetometer networks is associated with the eastward merging electric field (denoted as E_{sw} in **Figure 2.13**) due to dayside reconnection. Since the magnetopause counter current flows from dusk to dawn, it gives rise to a system of downward field-aligned currents on the morning side and upward currents in the noon sector (see Figure 11 of *Glassmeier and Heppner* [1992]). Such field-aligned currents occur naturally because of considerations of current continuity. In a similar manner, it is expected that the second pair of leading upward and trailing downward field-aligned currents is associated with the westward merging electric field at high latitude. The current system produced by this merging scenario does not conflict with the HFA current system. Furthermore, the current system produced by a pressure jump at the TD also does not conflict with the current system of the HFA mechanism. A HFA not only has a dynamic pressure decrease in the core but also has pressure pulses at the edge [*Sibeck et al.*, 1999, 2000]. The pre-existent pressure enhancement at the TD would be further reinforced by the pressure pulse at the trailing edge of the HFA. Such a pair of localized rarefaction and compression regions might produce a much stronger gradient in the magnetopause deformation and produce further impulsive current systems.

2.4.4 Energetics

In order to discuss the energetics of TCVs, a model current system is introduced in this Section. The model used in this Section is essentially based on the method of *Kamide and Matsushita* [1979]. The electric current continuity equation and the Ohm's law for the ionospheric current are approximated as follows.

$$\nabla_{\perp} \cdot \mathbf{i}_{\perp} = j_{\parallel} \sin \chi, \quad (2.12)$$

$$\mathbf{i}_{\perp} = \Sigma \cdot (\nabla \Phi), \quad (2.13)$$

where \mathbf{i}_{\perp} is the height-integrated current density, j_{\parallel} is the field-aligned current density flowing into the ionosphere, χ is the inclination angle of a geomagnetic field line with respect to the horizontal ionosphere, Σ is the height-integrated ionospheric conductivity tensor, and Φ is the electrostatic potential. Neglecting any conductivity gradient, equation (2.12) is reduced to the Poisson equation. The Poisson equation is numerically solved by a successive overrelaxation method for a given distribution of field-aligned currents in spherical coordinates constructed with the grid

points of 61×72 (every 1° in latitude and every 5° in longitude). Obtained electrostatic potential leads to the height-integrated current density via the equation (2.13). The Biot-Savart's law is finally applied to reproduce ground magnetic perturbations.

$$\mathbf{B}(\mathbf{r}_0) = \frac{\mu_0}{4\pi} \int \frac{\mathbf{j}(\mathbf{r}) \times (\mathbf{r}_0 - \mathbf{r})}{|\mathbf{r}_0 - \mathbf{r}|^3} d^3r \quad (2.14)$$

Magnetic field vector $\mathbf{B}(\mathbf{r}_0)$ is calculated from the three-dimensional current system $\mathbf{j}(\mathbf{r})$ using a matrix form of the Biot-Savart's law in spherical coordinates combined with the *Ashour's* [1971] relationship. The algorithm was shown by *Kisabeth and Rostoker* [1977].

The fitting procedure is subjectively done by trial and error. The final result is shown in **Figure 2.14** for the northern hemisphere. Taking into account the Pedersen and Hall conductivities in the realistic sunlit condition at 1316 UT on May 22, 1996, the principal and secondary diagonal of the height-integrated ionospheric conductivity tensor is taken as 5 mho and 10 mho, respectively. From a comparison between the left panel of **Figure 2.14** and the middle right panel of **Figure 2.3**, at 1316 UT, it is found that both horizontal and vertical magnetic perturbations are nicely reproduced. Also, the obtained convection speed of 500 m/s is consistent with SuperDARN observation (see **Figure 2.5**). The obtained three-dimensional current system is shown in the right panel of **Figure 2.14**. Convergence and divergence of ionospheric currents are clear around upward (blue) and downward (red) field-aligned currents, respectively. It is concluded that the geomagnetic perturbations of TCVs with a peak amplitude of ~ 100 nT and a horizontal scale size of ~ 1000 km is consistent with a total current amplitude of ~ 0.1 MA with a potential drop of ~ 20 kV. From the dot product of electric field and ionospheric current, the total Joule heating rate is calculated as 4.2 GW in this case.

The fact that the magnetic impulse events observed at IQ and SP have comparable amplitudes (see **Figures 2.2** and **2.3**) is one of the most interesting questions concerning the energetics of TCVs. In the May 22 event, in comparison with the northern hemisphere, small amplitude perturbations are observed in other Antarctic magnetometer stations (see **Figures 2.2** and **2.3**), which is consistent with low ionospheric conductivity in the dark southern hemisphere if the magnetospheric generator is the voltage generator. However, comparable amplitudes observed at IQ and SP can be interpreted as the properties of the current generator [e.g., *Murr et al.*, 2002]. *Lanzerotti et al.* [1991] also showed that most MIEs have comparable amplitudes at a magnetic conjugate pair of stations. The present wide spatial separation of the Antarctic magnetometer stations makes it difficult to settle this question. It is important to carry out measurements of geomagnetic perturbations with much denser arrays at least 100 km separation in Antarctica.

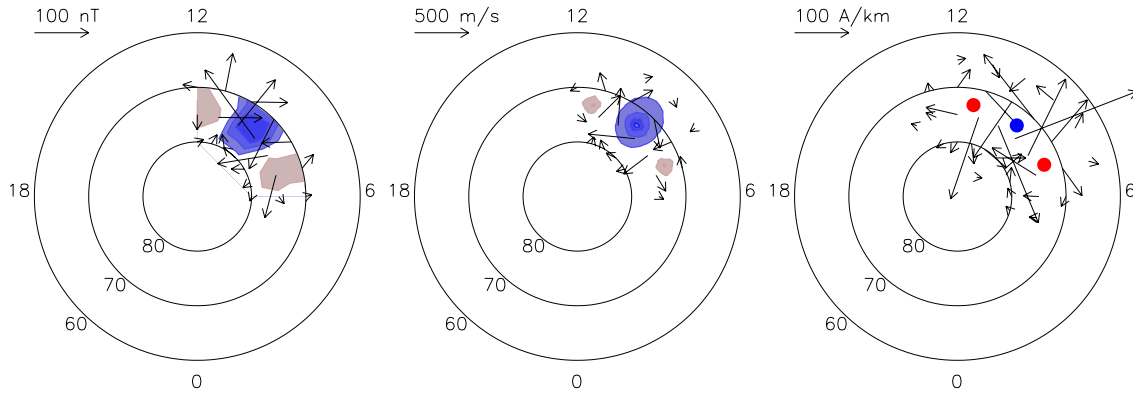


Figure 2.14. Modeling result of the TCV event at 1316 UT on May 22, 1996: (left) Ground magnetic field perturbations are shown with the same format as **Figure 2.3**. Virtual magnetometers are distributed at 70°, 75°, and 80° in latitude and every 1.0 local time intervals from noon to dawn. (middle) Ionospheric convection velocity vectors >50 m/s are shown every 5° latitude and 1.0 hour local time intervals. Blue and red contour lines show negative and positive electrostatic potential distribution every 4 kV intervals without zero potential line. (right) Ionospheric current vectors >10 A/km are shown every 5° latitude and 1.0 hour local time intervals. Red circles show downward field-aligned currents with an amplitude of 0.05 MA, while a blue circle shows an upward field-aligned current with an amplitude of 0.1 MA.

Equation (2.14) is quite general and can also be used to estimate magnetic field perturbations at geosynchronous orbit caused by the magnetospheric current system. Impulsive geomagnetic perturbations were observed at the geosynchronous orbit at 6.6 R_E altitude as shown in **Figure 2.15**. The GOES 8 spacecraft was located in the prenoon sector during the TCV event as shown in **Figure 2.16**. It is expected that pairs of field-aligned currents that produce the TCVs on the ground also produce impulsive magnetic field perturbations at geosynchronous orbit. A model current system shown in **Figure 2.16** can reproduce the fundamental features of GOES 8 observation quantitatively as shown by dotted lines in **Figure 2.15**. The fitting procedure is subjectively done by trial and error. The field-aligned currents are assumed to flow along dipole magnetic fields originated from 70° ionospheric latitude. The intensity of field-aligned currents flowing into and out of the ionosphere is assumed to be 0.5 MA and 1.0 MA, respectively. The separation angle of each field-aligned current is assumed to be 30° as inferred from **Figure 2.3**. The closure current is assumed to be azimuthal at 20° below the magnetic equator. The motion of the current system from 12 to 6 hour local time is consistent with the ground observations of the TCVs. The SYM-H index shown in the bottom panel of **Figure 2.15** implies rarefaction during 1310-1315 UT and compression during 1315-1320 UT. It is interesting to note from the comparison with the SYM-H index that this result can also be interpreted as a pair of localized rarefaction and compression of the magnetopause as shown in **Figure 2.13**.

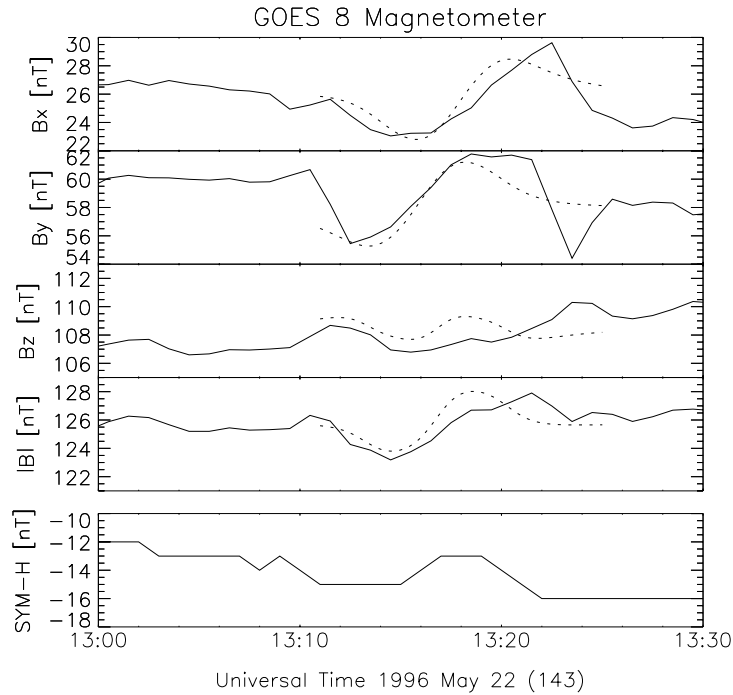


Figure 2.15. Magnetic field perturbations at geosynchronous orbit as measured by GOES 8 in GSE coordinates. The result of a three dimensional current system model is superposed as dotted lines. The values of SYM-H index are also shown in the bottom panel.

In summary, the total current intensity is estimated as 1.0 MA in the magnetosphere, and 0.1 MA in the ionosphere. This large amplitude difference may be caused by an oversimplification of the 3D magnetospheric current system. The simplification from actual complicated current density distribution into a filament current form possibly causes such a significant overestimation of actual total current intensity. Another possibility for overestimation is that this estimation could include the magnetospheric currents which are not closed via the ionospheric currents. It is therefore concluded that the total current intensity of this TCV event should be an order of 0.1 MA in the magnetosphere, and consistent with the estimation from the ionospheric current. The power supply into the ionosphere in this case is estimated as 1-10 GW, comparable value with that of typical SCs. It is worthwhile to consider the relative importance of TCVs to SCs because the induction effect due to SCs is known as dangerous in terms of space weather. The time scales of SCs and TCVs are similar (~10 min), and the occurrence probability of TCVs is ~10 times larger than those of SCs. Furthermore, it is much more difficult to identify the solar wind source of TCVs than that of SCs. There is another noteworthy point-of-view for the energetics of TCVs. TCVs frequently occur during quiet conditions when the background energy is a few GW under northward IMF. This means that TCVs tend to play a dominant role in the dayside magnetosphere in terms of the energetics.

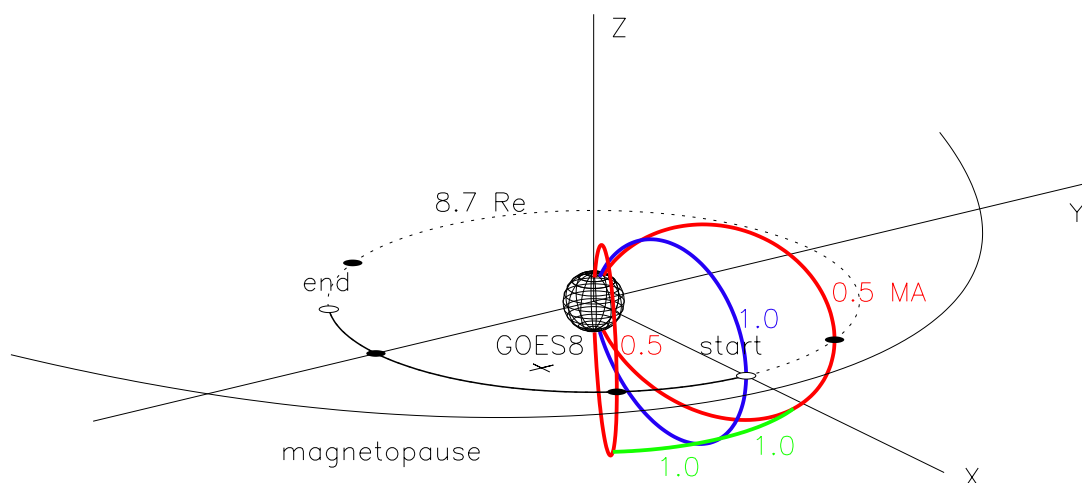


Figure 2.16. Model current system to reproduce magnetic field perturbations at geosynchronous orbit as measured by GOES 8. Field-aligned currents flowing into and out of the ionosphere are indicated by red and blue lines, respectively. These field-aligned currents are connected each other via the closure currents flowing in the magnetosphere azimuthally as shown by green lines. The model current circuit is azimuthally moved from 'start' to 'end' to produce the dotted lines in **Figure 2.15**.

2.5 Summary

The solar wind source of the TCV event on May 22, 1996 is identified to be a TD exhibiting a rapid northward turning of the IMF. This TD satisfies the criteria for HFA formation at the bow shock. That is, this TD has inward pointing MEFs at both sides of the TD and the normal vector of TD has a large cone angle with respect to the sunward direction. The sweeping motion of the intersection line of TD and the Earth's bow shock is also consistent with the observed motion of TCVs. The magnetopause deformations due to the HFA can explain the triggering process, temporal and spatial evolution of the current system, and all other observed features of the TCVs. Other mechanisms such as solar wind pressure pulses or dayside reconnection burst alone can not explain all of these features. The three-dimensional current system of the TCVs produces a transient production of localized aurora and localized F region irregularities with hundreds of km extent in the ionosphere. The total current intensity of this current system is estimated as an order of 0.1-1 MA, and the total power supply into the ionosphere is estimated as 1-10 GW.

Chapter 3

Statistical Study of MIEs

In **Chapter 2**, it was shown that the tangential discontinuity (TD) is one of the most important solar wind origins of traveling convection vortices (TCVs). The importance of the hot flow anomaly (HFA) was also shown by the comprehensive event study. In this Chapter, a statistical analysis is applied to magnetic impulse events (MIEs) to reveal the contribution rate of HFAs and several other generation mechanisms to produce TCVs.

3.1 Magnetometer Data Analysis

Data obtained by the fluxgate magnetometer at South Pole (SP) station are used to identify MIEs for the 8 year period 1995-2002. Many past statistical studies of MIEs have used visual detection for their event selections [Glassmeier *et al.*, 1989; Vorobjev *et al.*, 1994b; Sibeck and Korotova, 1996; Sitar and Clauer, 1999]. Instead, this study uses a selection algorithm using the continuous wavelet transform [Torrence and Compo, 1998]. Assume that one has a wavelet function, $\psi_0(\eta)$, that depends on a non-dimensional time parameter η . The best wavelet function, especially suitable for the objective and reproducible detection of solitary waveforms and therefore to detect MIEs, is the Paul wavelet that has an identical waveform to that of typical MIEs:

$$\psi_0(\eta) = \frac{2^m i^m m!}{\sqrt{\pi(2m)!}} (1 - i\eta)^{-(m+1)}, \quad (3.1)$$

where m is the order, here taken to be 4. The wavelet function is shown in **Figure 3.1**. Assume that one has a time series, x_n , with an equal time spacing δt and $n = 0 \dots N - 1$. The continuous wavelet transform of a discrete sequence x_n is defined as the convolution of x_n with a scaled and translated version of $\psi_0(\eta)$:

$$W_n(s) = \sum_{n'=0}^{N-1} x_{n'} \psi^* \left[\frac{(n' - n)\delta t}{s} \right], \quad (3.2)$$

where the (*) indicates the complex conjugate.

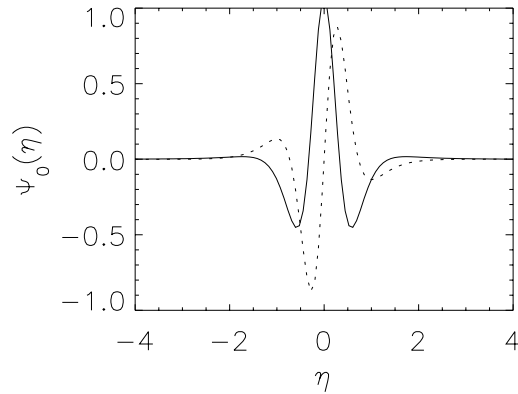


Figure 3.1. Waveform of the wavelet function used in this analysis. The real part and imaginary part for the Paul wavelet in the time domain are plotted by solid and dotted lines, respectively.

These magnetometer data at SP used for MIE detection is the 3-component vector data with 10 s values in one day unit, after denoising, interpolating, and resampling with an equal time spacing of 10 s. That is, $N = 8640$ points and $\delta t = 10$ s. Here, “MIE power” is defined as a scale-averaged wavelet power from 240 s to 640 s normalized by the scale-integrated time-averaged wavelet power with a 90-min running window. For the Paul wavelet with the order of 4, the relationship between the Fourier period λ and the wavelet scale s is $\lambda \sim 1.4s$ [Torrence and Compo, 1998]. In this case, the range of the Fourier period becomes 5.6 min to 14.9 min, corresponding to the typical MIE duration. We selected events in which MIE power is greater than 2. This criterion means that an impulsive target has more than twice the power of the running variance in a 90 min window. This factor of 2 is decided by tuning to find traditional MIEs in the literature. Note that this criterion is a pattern matching process in any amplitude range, and independent of the absolute MIE amplitude itself.

If the detected MIEs in different components are within 15 min, these MIEs are treated as the same event. In order to avoid any undesirable effects of the cone of influence [Torrence and Compo, 1998] or nighttime substorms, only dayside events occurring between 6 and 18 MLT (0930-2130 UT at SP) are selected. This is reasonable because MIEs are concentrated on the dayside of the Earth [e.g., Lanzerotti *et al.* 1991]. Finally, it is required that the peak-to-peak amplitude variation is greater than 100 nT during the MIE interval at least in one component, where “MIE interval” means the time interval 10 min before and after each extremum of MIE power. A typical example of event detection for the HFA event on July 24, 1996 [Sibeck *et al.*, 1999] is shown in **Figure 3.2**. The detected MIE is shown by vertical arrows.

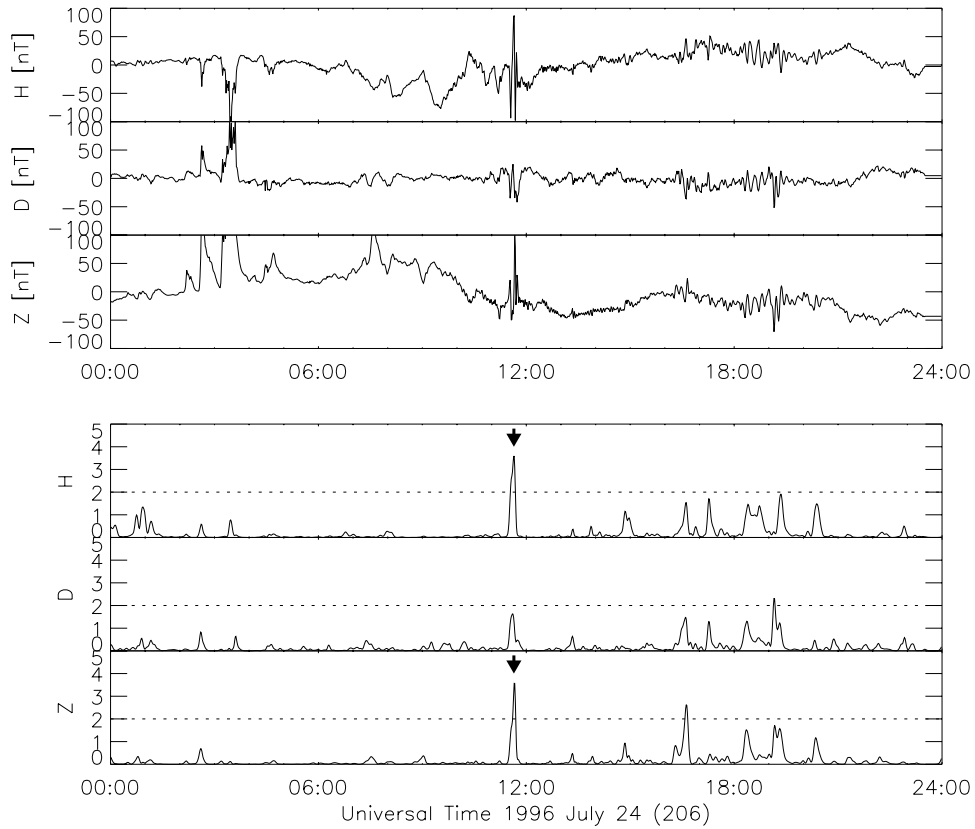


Figure 3.2. An example of MIE detection on July 24, 1996. Top three panels show the three components of magnetic field for 1-day interval measured by the fluxgate magnetometer at South Pole station. Bottom three panels show MIE power for each of three components. The detected MIE is shown by vertical arrows.

The new detection algorithm of MIEs described above is tuned to give almost identical detection efficiency in comparison to the past studies that have used human-eyes of magnetometer specialists. Consequently, the results in this analysis are remarkably consistent with previous results in the literature. The final list consists of 825 MIEs for the 8 year period 1995-2002. This list includes the May 22, 1996 event investigated in **Chapter 2**, and other MIEs listed in **Table 2.1**. Also, 8 of 31 TCV events analyzed by *Murr and Hughes* [2003] are included in the MIE list. *Murr and Hughes* [2003] used criteria combining several magnetometers in the northern hemisphere to confirm the traveling nature of TCVs. Essentially, the list made in this study is almost identical with their list, with a difference mainly due to the difference of local time coverage between their magnetometer network and SP.

3.2 Solar Wind Discontinuity Analysis

Solar wind data from the Wind and ACE spacecraft are used in order to provide information on interplanetary magnetic field (IMF), solar wind velocity, proton temperature, and proton number density. For convenience, IMF and other plasma parameters at ACE and Wind that are used for the analysis are denoised, interpolated, and resampled with an equal time spacing of 64 s using the Key Parameter data from the CDAWeb (<http://cdaweb.gsfc.nasa.gov/>). In this study, only far upstream solar wind data is required. However, Wind observes bow shock crossings around the time of its perigee. In order to remove such near-Earth data, a simple criterion that the Wind satellite is located more than 30 R_E upstream is used. Since the Wind spacecraft moved away from the L1 point after May 1998, the Wind-based analysis is terminated in 1998 and ACE data is used instead after February 1998. Wind 3-s high-resolution data are used for detailed classification of IMF discontinuities. OMNI data (<http://nssdc.gsfc.nasa.gov/omniweb/>) of 1-hour averaged solar wind parameters are also used in this study in order to obtain background solar wind parameters.

Figure 3.3 shows an example of the 4 hour interval including the detected MIE at 1138 UT. The IMF discontinuity is detected using a criterion that the IMF changes its direction by at least 30° within 128 s (using the 64-s resampled data). Multiple discontinuities within 5 min are regarded as a single discontinuity. Detected IMF discontinuities are shown with vertical dotted lines in **Figure 3.3**. The final list includes about 4.7×10^4 and 9.7×10^4 IMF discontinuities during the period of 1995-1997 for Wind and the period of 1998-2002 for ACE, respectively.

The selection of TDs from the detected IMF discontinuities is a central objective of this study. TDs play the role of a boundary separating different plasma regions. Significant jumps in any of total magnetic field, ion temperature, or ion number density are the first clue for TDs. On the other hand, the first clue for rotational discontinuities (RDs) is a negligible jump in every scalar parameter because RDs do not usually have such magnitude changes, unless there is a significant thermal anisotropy in the transition region [*Hudson, 1970*]. Conventionally, the normal vector of the IMF discontinuity plane is another clue to distinguish between TDs and RDs because TDs do not have magnetic field across the discontinuity plane, whereas RDs often do.

For the minimum variance analysis (MVA) described in **Section 2.2.2**, Wind 3 s data for the time interval of 30-120 s are used. The cutoff ratio of the intermediate to the minimum eigenvalues is taken as $\lambda_{\text{int}} / \lambda_{\text{min}} > 2$ to define the discontinuities. The time lag between each MIE and corresponding IMF discontinuity is confirmed to be consistent in terms of the derived normal vector \mathbf{n}_{MVA} with equation (2.2), where nominal magnetopause position is assumed at GSE $(x, y, z) = (10, 0, 0)$ as the target and the measured solar wind velocity as \mathbf{V} . A maximum 20 min error is allowed for this lag coincidence test.

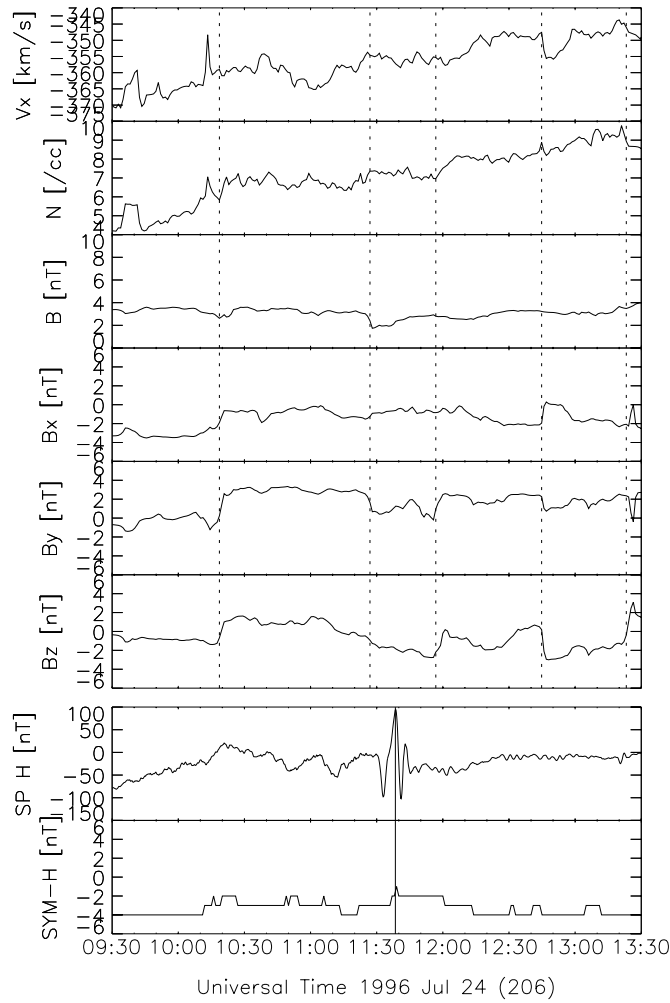


Figure 3.3. An example of IMF discontinuity detection. From top to bottom, solar wind velocity, proton number density, total IMF, Bx, By, and Bz components in GSM coordinates are shown for a 4-hour interval on July 24, 1996. Detected IMF discontinuities are indicated by vertical dotted lines. The bottom two plots show variations of the H component at South Pole and the SYM-H index. The detected MIE is indicated by vertical solid lines at 1138 UT.

Total 36 MIEs are found to be appropriate for the detailed discontinuity analysis. Each of these MIEs has a one-to-one correspondence with an IMF discontinuity. The number of events (36) is low because this one-to-one criterion is quite strict. Under our selection criteria of IMF discontinuities, there are two or more IMF discontinuities that could be the solar wind origin of most of the MIEs. In other words, several IMF discontinuities usually exist in one hour interval around MIE timing.

Table 3.1. Classification criteria of TD, RD, and Others.

TD:	$\Theta < 15^\circ$ and ($\Delta N/N > 10\%$, $\Delta V/V > 10\%$, or $\Delta B/B > 20\%$)
RD:	$\Theta > 15^\circ$ and ($\Delta N/N < 10\%$, $\Delta V/V < 10\%$, and $\Delta B/B < 20\%$)
Others:	$\Theta < 15^\circ$ and ($\Delta N/N > 10\%$, $\Delta V/V > 10\%$, or $\Delta B/B > 20\%$)

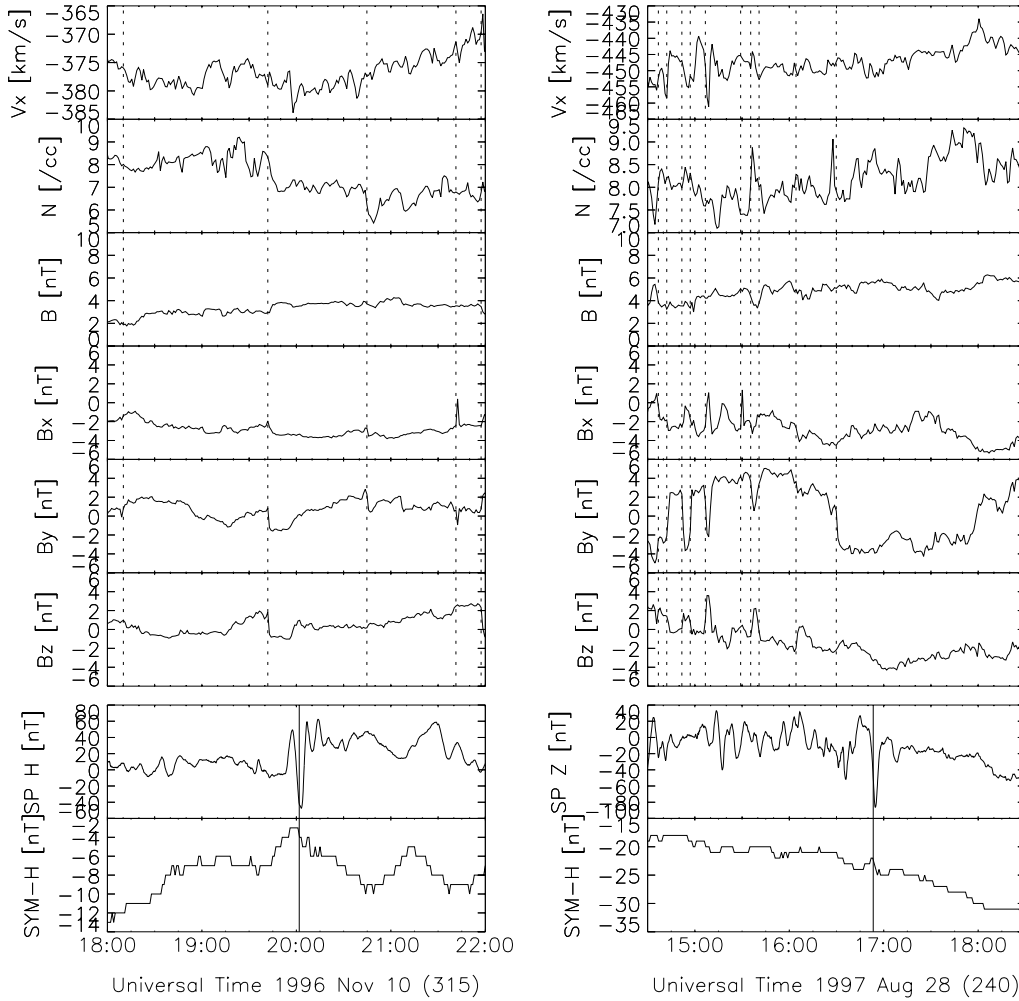


Figure 3.4. Typical examples of (left) TD at 1942 UT on November 10, 1996 and (right) RD at 1631 UT on August 28, 1997. The format is the same as **Figure 3.3**.

Since there is no magnetic field across TDs, the normal vector of the TD, \mathbf{n}_{TD} , is deduced by a cross product of magnetic fields immediately upstream and downstream of the TD. Let us define ϕ as the acute angle between \mathbf{n}_{TD} and \mathbf{n}_{MVA} . The parameters Θ , $\Delta B/B$, $\Delta N/N$, and $\Delta V/V$ are used to determine whether each event is a RD or a TD with the identification criteria listed in **Table 3.1**. Typical examples for TD and RD are shown in the left and right panels in **Figures 3.4**, respectively. The estimated time lag using equation (2.2) is 13 min for the November 10, 1996 event, and the observed time lag is 26 min. This is a typical TD event because $\Theta = 9^\circ$ and there are significant jumps in N and B . The estimated time lag using equation (2.2) is 23 min for the August 28, 1997 event, and the observed time lag is 21 min. This is a typical RD event because $\Theta = 90^\circ$ and there are negligible jumps in N , V , and B . The 25 TD events and the remaining 11 events are listed in **Tables 3.2** and **3.3**.

Table 3.2. MIEs and TDs with one-to-one correspondence.

#	Date	MIE	TD
01	1995/02/05	16:03	14:52
02	1995/02/28	14:30	13:49
03	1995/04/26	11:18	09:48
04	1995/08/26	13:58	13:41
05	1995/08/29	16:15	15:51
06	1995/08/30	14:21	14:01
07	1995/09/13	13:49	14:00
08	1995/11/23	11:37	11:05
09	1996/04/27	14:11	13:45
10	1996/05/22	13:11	12:56
11	1996/07/24	11:38	10:19
12	1996/09/08	13:49	13:35
13	1996/10/02	12:50	12:36
14	1996/10/21	10:56	10:26
15	1996/11/10	20:02	19:42
16	1996/12/10	15:28	15:18
17	1997/05/02	17:06	16:33
18	1997/07/18	15:31	15:05
19	1997/07/24	13:38	13:15
20	1997/08/11	14:08	13:45
21	1997/08/14	11:48	11:24
22	1997/08/20	09:56	09:15
23	1997/09/25	13:31	13:06
24	1997/09/25	19:47	19:51
25	1997/10/03	14:17	14:02

Table 3.3. MIEs and RDs with one-to-one correspondence.

#	Date	MIE	RD
01	1995/02/28	14:56	14:08
02	1995/05/27	16:12	15:25
03	1995/08/28	12:21	11:55
04	1995/08/28	18:13	17:49
05	1995/08/28	18:36	18:05
06	1997/05/04	11:41	10:46
07	1997/08/01	10:57	10:35
08	1997/08/28	16:53	16:31

Table 3.4. MIEs and Others with one-to-one correspondence.

#	Date	MIE	Others
01	1995/01/29	12:45	12:12
02	1995/06/04	20:44	19:46
03	1995/11/04	19:04	18:25

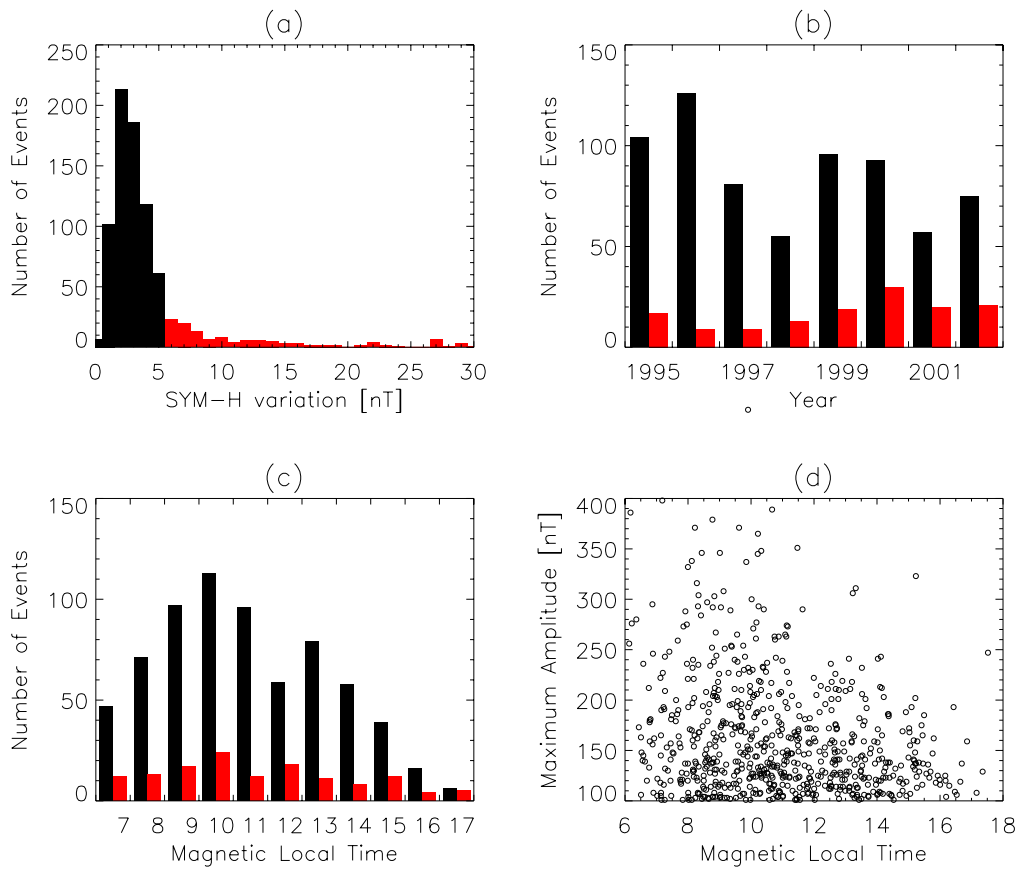


Figure 3.5. MIE occurrence distributions: (a) Histograms of MIE occurrence versus SYM-H perturbations, (b) long term variations of the annual number of MIEs from 1995 to 2002, (c) histograms of MIE occurrence versus MLT, and (d) scatter plot of maximum amplitude versus MLT. Red and black histograms identify compressive MIEs with >5 nT SYM-H perturbations and non-compressive MIEs with <5 nT SYM-H perturbations, respectively.

3.3 Occurrence Properties

Statistical results for occurrences of 825 MIEs are shown in **Figure 3.5**. The MIEs in **Figure 3.5** are divided into two types in terms of the amplitudes of the SYM-H fluctuations: non-compressive MIEs with <5 nT SYM-H perturbations (solid histograms) and compressive MIEs with >5 nT SYM-H perturbations (lighter histograms). From **Figure 3.5a**, it is found that MIEs with global compression/expansion signatures are about 17%. Note that a number of sudden commencements (SCs) are actually included in the 825 events. When we define SCs as events with >10 nT step-like jump within 10 min in the SYM-H index, a total of 66 SCs are found in the 825 events. This accounts for 8.0% of 825 MIEs.

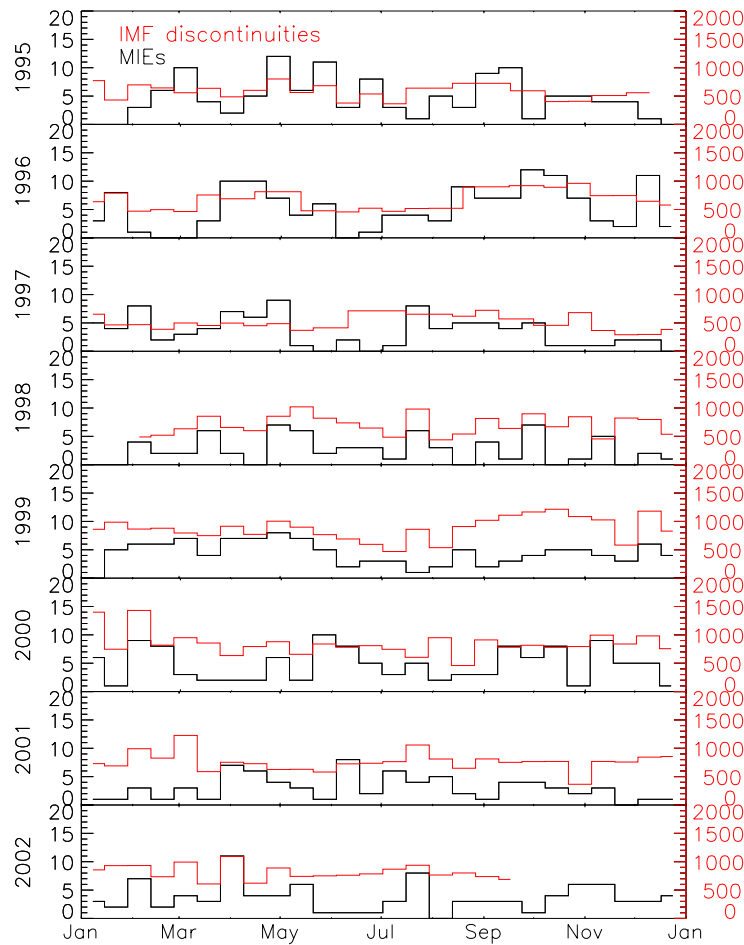


Figure 3.6. Seasonal variations in the occurrence numbers of MIEs (black lines) and IMF discontinuities (red lines) for the 8 year period 1995-2002. The occurrence numbers are counted every 14 day intervals.

Figure 3.5b shows the long term trend in the annual number of MIEs for the period 1995-2002. The occurrence of compressive MIEs increases from solar minimum to solar maximum. This suggests that the solar wind driver of MIEs tends to be more compressive in the maximum phase. **Figure 3.5c** shows MIE occurrences versus MLT for the 8-year period 1995-2002. The double-peak distribution originally reported by *Lanzerotti et al.* [1991] is reproduced with a larger peak in the morning sector and a smaller peak in the afternoon sector. Note that the double-peak distribution is due to a dip in occurrence at 12 MLT bin. All other histograms exhibit a broad distribution with a single peak in the morning sector. The occurrence maximum in the local morning hours shown in **Figure 3.5c** are consistent with many other studies [*Glassmeier et al.*, 1989; *Vorobjev et al.*, 1999; *Zesta et al.*, 2002]. **Figure 3.5d** shows a scatter plot of the peak-to-peak amplitudes of MIEs versus MLT. Only the non-compressive events (total of 687 events) are plotted. The maximum amplitude tends to be larger in the prenoon sector than in the post-noon sector. A similar distribution was reported by *Sibeck and Korotova* [1996].

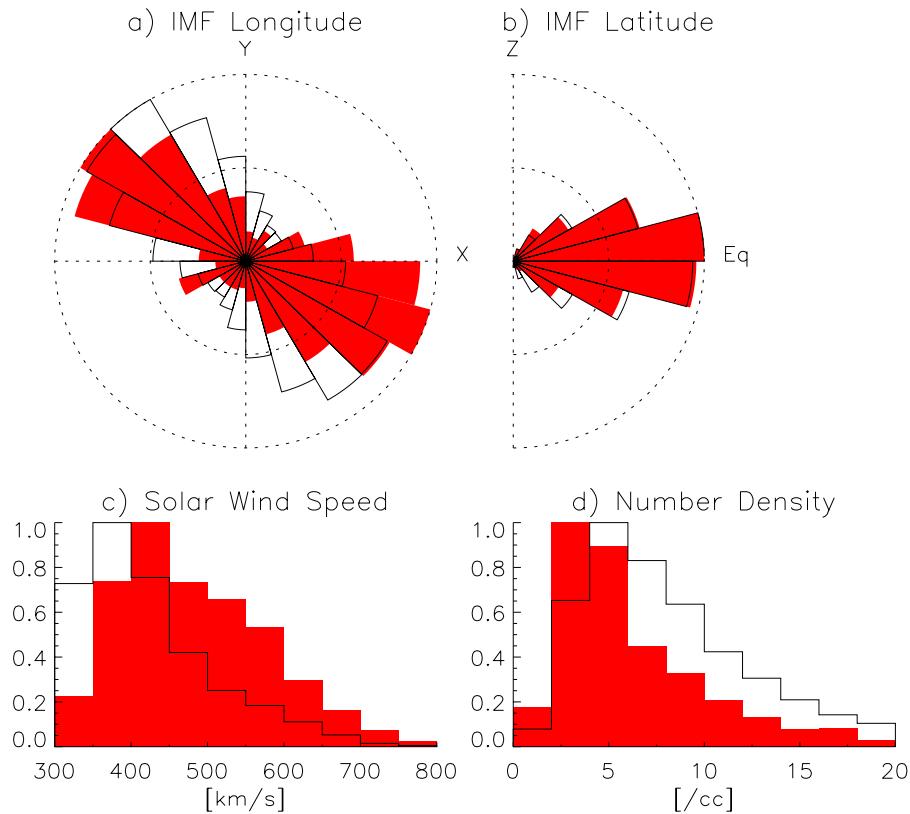


Figure 3.7. Histograms of MIE occurrence versus solar wind parameters. Plotted are normalized occurrences versus (a) GSM longitude and (b) latitude of IMF, (c) solar wind velocity, and (d) proton number density. Red areas indicate occurrences in the intervals 30 min before and after the timings of MIEs, whereas open areas indicate the distribution for the entire 8 year period using OMNI 1-hour averaged data.

A comparison is made between the list of 825 MIEs and the list of 14.4×10^4 IMF discontinuities. **Figure 3.6** shows seasonal variations in occurrences of MIEs and IMF discontinuities as histograms at 14 day intervals in sequence of the 8 years from 1995 to 2002. Histograms for both MIEs and IMF discontinuities show similar seasonal trends. The correlation coefficients between the number of MIEs and that of IMF discontinuities are 0.48 and 0.40 for 1995-1997 Wind data and 1998-2002 ACE data, respectively. These values of correlation coefficients are statistically significant and suggest that both phenomena are correlated each other.

Figure 3.7 shows the normalized MIE occurrence distributions (825 MIEs) as functions of the IMF orientations in the X-Y plane (top left), and the X-Z plane (top right), and solar wind speed (bottom left), and density (bottom right). Shaded areas indicate the occurrences of median values for the intervals of 30 min before and after 825 MIEs, whereas open areas outlined by thick solid lines indicate the distributions of interplanetary parameters for the entire interval 1995-2002 from OMNI 1-hour averaged data. In all cases, the times of solar wind data are shifted to the magnetopause position, considering the measured solar wind velocities and the separation distances along the

Sun-Earth line, and assuming the flat and non-tilted discontinuity planes. The magnetopause is taken as a target at GSE $(x, y, z) = (10, 0, 0)$ for the arrival estimation. As shown in **Figure 3.7**, MIEs occur under a wide range of solar wind conditions. A preference for the IMF direction approaching to the Sun-Earth line (**Figure 3.7a**) is consistent with previous statistical results [Konik *et al.*, 1994; Sibeck and Korotova, 1996; Vorobjev *et al.*, 1999]. It is also found that MIE occurrence probabilities increase in high-speed (**Figure 3.7c**) and low-density (**Figure 3.7d**) solar wind.

3.4 Discussion

First, the cause of the long-term trends found in the occurrences of MIEs and IMF discontinuities is discussed. In **Figure 3.8**, the top panel shows the seasonal variations of these two parameters, averaged over the 8 year period 1995-2002. The histograms of MIEs and IMF discontinuities are shown by black lines and red lines, respectively. The occurrences of MIEs are characterized by a weak semi-annual variation with maxima in the spring and fall seasons. The occurrences of discontinuities also have a maximum in fall. The absence of a clear maximum in spring is due to large fluctuations in the occurrence number of discontinuities in the period from January to March during the solar maximum phase when we analyzed. For example, it is clear from **Figure 3.6** that triple peaks in the beginnings of January, February, and March are found in both 2000 and 2001. A semi-annual trend of MIE occurrences was reported by *Sibeck and Korotova* [1996], based on magnetometer data acquired in the northern hemisphere. In contrast, *Glassmeier et al.* [1989] found a minimum in occurrence during equinoxes in their statistical study, and *Zesta et al.* [2002] concluded that there is no clear seasonal variation for TCV events.

It is also worthwhile to note here that there is an apparent preference in MIE occurrence probabilities for high-speed and low density solar wind conditions. These are the conditions associated with coronal hole streams, although MIE occurrences also include many intervals with normal conditions, or even conditions opposite to those expected for coronal holes. It is noteworthy that *Tsurutani and Ho* [1999] have shown that the number of IMF discontinuities increases in the solar wind originating from coronal holes. The semi-annual variation of MIE occurrence may be explained by the 7° declination of the Sun's rotation axis to the ecliptic plane. In this geometry, high-speed streams from coronal holes with inward (outward) IMF tend to hit the Earth in spring (fall). A similar but more complicated effect has been discussed for geomagnetic activity for a long time [e.g., *Russell and McPherron*, 1973]. The bottom panel in **Figure 3.8** shows histograms for the durations of high-speed (>600 km/s) streams, averaged over the 8-year period 1995-2002. It is clear that the durations of the streams with inward (outward) IMF increase in spring (fall), consistent with the hypothesis. However, the solar wind conditions of high-speed streams and low densities are inconsistent with previous statistical results concerning the occurrence conditions of MIEs [e.g., *Sibeck and Korotova*, 1996; *Vorobjev et al.*, 1999]. This discrepancy may be due to different data sets. The MIE list in this study has 825 events covering from solar minimum to solar maximum conditions. This large event number and long-term period would produce much reliable results compared with the past studies.

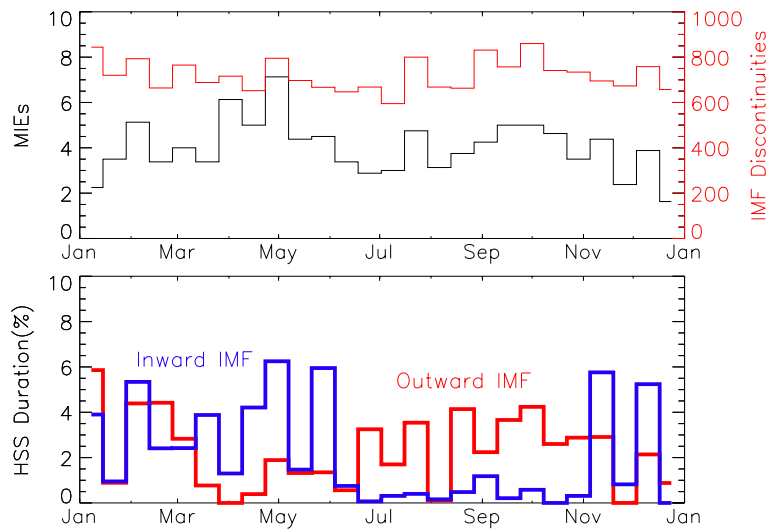


Figure 3.8. (top) Averaged occurrences of MIEs (black lines) and IMF discontinuities (red lines) integrated over the 8-year period 1995-2002. (bottom) Histograms for the durations of high-speed (>600 km/s) streams averaged over the 8-year period 1995-2002. High-speed streams with inward and outward IMF are distinguished as blue and red lines, respectively.

Secondly, the solar wind origins and the generation mechanisms of MIEs are discussed. TDs would include several different mechanisms for producing MIEs as previously proposed, such as bursty reconnection, pressure pulses, and HFAs as discussed in **Section 2.4.3** (see **Figure 2.13**). It is important to find the percentage of each of these driving mechanisms contributing to the production of MIEs. Out of the 36 events listed in **Tables 3.2** and **3.3**, the numbers of positive, negative and no Bz turnings are 11, 12, and 13, respectively. From this result, it is concluded that the bursty reconnection mechanism may explain at most ~30% of MIEs. There are 6 MIEs with SYM-H variations >5 nT in the 36 events. From this result, it is concluded that the pressure pulse mechanism may explain at most ~20% of MIEs. The small number of events that are related to pressure pulses is consistent with previous studies [Konik *et al.*, 1994; Sibeck and Korotova, 1996; Vorobjev *et al.*, 1999]. Note that this occurrence rate of compressive MIEs is very similar to the result of **Figure 3.5a**. On the other hand, there are 25 TDs, 8 RDs and 3 Others in **Tables 3.2**, **3.3**, and **3.4**. That is, ~70% of the IMF discontinuities that are associated with MIEs are TDs. These TDs have special characteristics as discussed below.

Previous studies have shown that the formation of HFAs requires solar wind motional electric fields (MEF) pointing toward TD, at least on one side of TD [Schwartz *et al.*, 2000]. **Figure 3.9** shows a scatter plot of the angles between the 25 TD normal vectors and the MEF for the events given in **Table 3.2**. The five (of 25) TD events (20%) in the right bottom sector do not have inward pointing MEF on either side. It is important to note that these five events are accompanied by positive or negative IMF Bz turnings. This may imply some contributions of reconnection processes to produce MIEs.

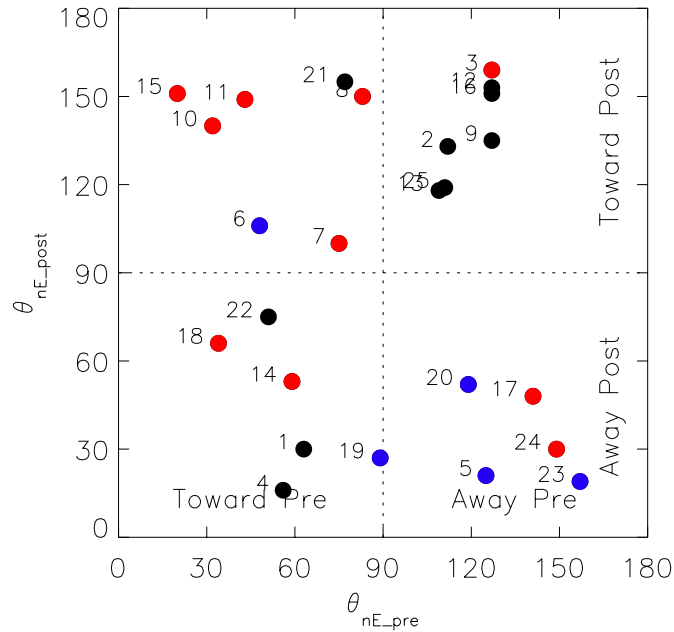


Figure 3.9. Scatter plot of the angle between the TD normal vector and the solar wind motional electric field in the region prior to (horizontal) and after (vertical) TD passage. Events shown by red, blue, and black circles have northward, southward, and no IMF turnings, respectively. The event number of **Table 3.2** is indicated for each event.

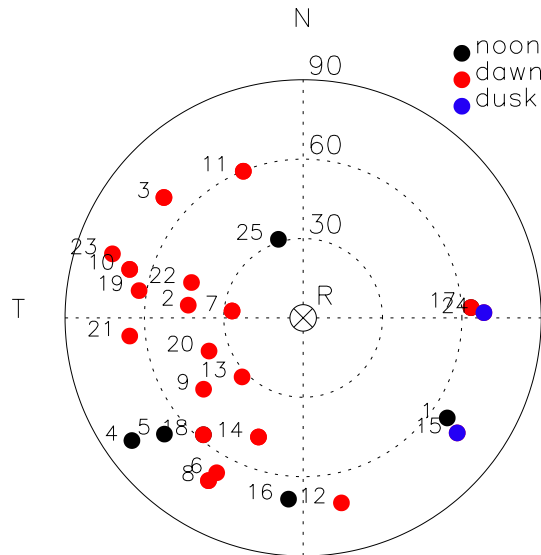


Figure 3.10. Directions of normal vectors of TDs associated with MIEs. The normal vectors are displayed in the RTN coordinate system, with R radially out from the Sun, N northward, and T completes the right-handed triad. The plot shows a view from the Sun, with T to the left and N toward the top. The radial coordinate in the plot gives the cone angle from the R axis from 0° (center) to 90° (outer edge). Conventionally, normal vectors are reversed as is required to ensure positive R components. Occurrences of MIEs in the dawn (dusk) sector are indicated by red (blue) circles. Other MIEs in the noon sector (11-13 MLT) are indicated by black circles. The event number of **Table 3.2** is indicated for each event.

Figure 3.10 shows the directions of the TD normal vectors associated with MIEs in the RTN coordinate system with R radially out from the Sun and N northward. We classified the TDs into three groups: TDs related to MIEs occurring in the dawn (dusk) sector are indicated by red (blue) circles. Other events in the noon sector (11-13 MLT) are indicated by black circles. It is found from this result that the orientations of TDs control the generation sites of MIEs. The same TD will first lie tangent to the bow shock on one side, then intersect it on the same side, and then intersect it on the other side. MIEs are more common on the dusk side when TDs intersect the dusk bow shock at a perpendicular angle, and vice-versa. The large cone angle of the TD normal ($>40^\circ$) is another condition for enhancement of the TD-bow shock interaction. HFAs prefer such a condition because the effective time of the interaction between the TD and the bow shock becomes longer [Schwartz *et al.*, 2000]. Combining the above two HFA criteria of inward MEF and large cone angle, there are 17 TD events that satisfy both criteria simultaneously. Since total 36 MIEs (25 TDs, 8 RDs, and 3 others) were selected, we can conclude that HFAs can explain at most ~50% of MIEs.

Finally, the importance of the interaction between the solar wind and the bow shock is discussed. The results shown in **Figure 3.7** confirm that low density, high-speed solar wind conditions, and/or radial IMF conditions are evidently more favorable for occurrences of MIEs. A significant correlation in the occurrences of MIEs and IMF discontinuities was also found from the long term analysis as shown in **Figure 3.6**. Furthermore, as shown in **Figures 3.9** and **3.10**, significant preferences are found in MIE occurrences for TDs with inward MEF and large cone angle conditions that are the empirical criteria for HFA formation at the bow shock [Schwartz *et al.*, 2000]. However, the fact that approximately 100 times as many IMF discontinuities as MIEs are observed suggests that IMF discontinuities themselves may be an inefficient source of MIEs, although the factor of ~100 could be reduced to the factor of ~10, considering the fact that SP alone can not detect all the MIE signatures on the ground and assuming that the local time coverage of SP is a few hours. Some special properties, such as TDs with inward pointing MEF, should be needed if IMF discontinuities are a necessary condition for triggering MIEs. On the other hand, there could be other driving factors. High-speed stream and radial IMF enhance the interaction between the bow shock and incoming solar wind to produce foreshock cavities via the ion beam instability [Sibeck *et al.*, 2001]. It is also worthwhile to note here that there is no discontinuity as a possible source for the TCV event on June 6, 1997, and strongly radial IMF is a possible cause of the TCV event [Kataoka *et al.*, 2001]. Triggering processes and noonward motion of the TCV can be explained by foreshock cavities. This evidence implies that IMF discontinuities are not always needed to produce MIEs, and not only HFAs but also foreshock cavities are important mechanism to produce MIEs. For example, it is possible that IMF discontinuities are more common under high-speed stream and so are MIEs, and foreshock cavities are sensitive and unstable to produce MIEs under such conditions. In this reason, it is concluded that both HFAs and foreshock cavities are the main cause of MIEs.

3.5 Summary

The lists of MIEs and IMF discontinuities were compiled during the 8-year period 1995-2002 that covers from solar minimum to solar maximum. From the comparison between the two lists, it was found that seasonal variations in occurrences of IMF discontinuities and MIEs have a significant correlation to each other. It was also found that MIEs tend to occur during intervals of low density, high-speed solar wind streams, and/or radial IMF. Of the 36 one-to-one correspondence events between MIEs and IMF discontinuities, ~70% of IMF discontinuities are identified to be TDs. The HFA mechanism can explain at most ~50% of the MIEs, and dayside reconnection burst or solar wind pressure pulses were possibly associated with about ~30% and ~20% of the MIEs, respectively. The relationship between the three-dimensional orientation of TDs and the generation site of MIEs is also consistent for the HFA mechanism. All of the obtained results are consistent with HFAs or foreshock cavities being the main cause of MIEs.

Chapter 4

Simulation of TCVs

As shown in **Chapter 2**, it is revealed that one of the most important sources of traveling convection vortices (TCVs) is the magnetopause deformation due to hot flow anomalies (HFAs). Statistical results in **Chapter 3** also suggest that the magnetopause deformation due to both HFAs and foreshock cavities is the fundamental source of TCVs. The essential effect of these HFAs and foreshock cavities on the magnetosphere can be simplified and represented by a “localized density pulse” superposed just in front of the bow shock. In this Chapter, the transient response of the Earth’s magnetosphere-ionosphere system to such a localized density pulse in the solar wind is investigated using a global magnetohydrodynamic (MHD) simulation. It is demonstrated that this model can reproduce the characteristics of TCVs.

4.1 Simulation Model

All of the previous simulation models [*Lysak and Lee, 1992; Slinker et al., 1999; Chen et al., 2000*] reproduce symmetrical vortices with respect to the noon-midnight meridian because these models dealt with uniform pressure pulses. However, observed TCVs do not show such a dawn-dusk symmetry. Statistical studies show the dominant occurrence of the morning TCVs as shown in **Figure 3.5c**. In addition, pressure pulses localized in the prenoon sector may be a more realistic solar wind input in terms of foreshock cavities [*Sibeck et al., 2001*]. In this scope, a localized density pulse is placed in the prenoon sector just in front of the bow shock as shown in **Figure 4.1**.

The numerical technique used in this study was developed by *Tanaka* [1994, 1995, 2000a, 2000b]. The finite volume (FV) total-variation diminishing (TVD) scheme is employed to solve the three-dimensional MHD equations in a solar wind-magnetosphere-ionosphere system. The boundary conditions and the grid system are explained in detail by *Tanaka* [2000a]. The outer and inner boundaries for the simulation are at $200 R_E$ and $3 R_E$ from the center of the Earth. Simulation results at $3 R_E$ are mapped along dipole field lines to the ionosphere at $1 R_E$. The inner boundary condition is given by current continuity and continuity of plasma flows tangential to the ionosphere. The height-integrated ionospheric conductivity is given by considering the effects of solar EUV, diffuse auroral precipitation, and upward field-aligned current. The grid system within the dayside magnetosphere is basically a spherical coordinate system. The spatial resolution in the dayside magnetosphere is $\sim 0.25 R_E$ in radial direction, $\sim 1.0^\circ$ in latitude, and $\sim 1.5^\circ$ in longitude.

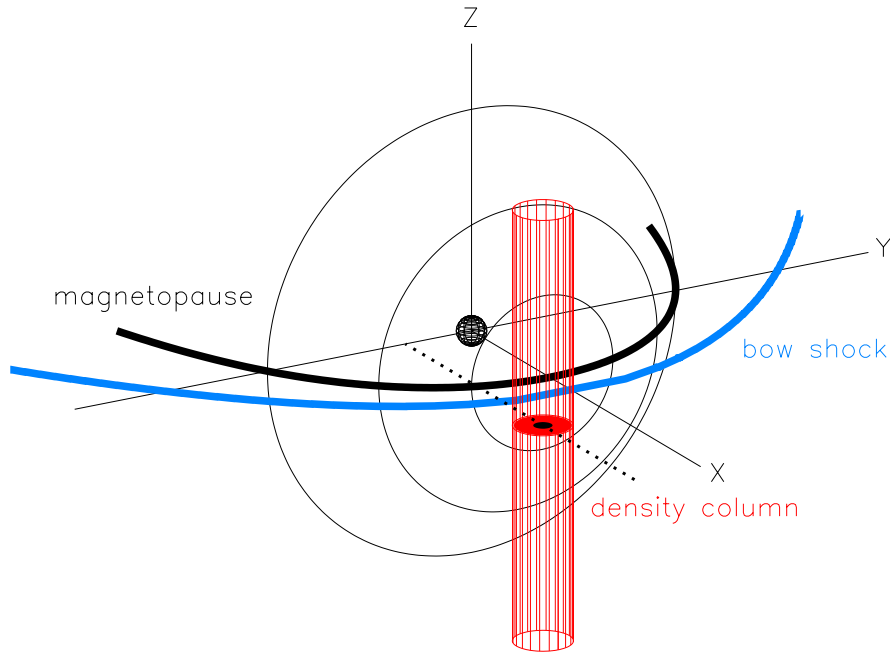


Figure 4.1. Schematic illustration of the simulation model. Solar wind number density is enhanced to 25 /cc within the red column from 10 /cc outside the column. The equatorial cuts of the magnetopause and the bow shock are shown by black and blue lines, respectively. The three-dimensional magnetopause surface is also indicated by black circles.

Initial conditions are basically the same as the ones given by *Fujita et al.* [2003] except for the localized compression of the magnetosphere. As shown in **Figure 4.1**, a cylindrical density enhancement with $2 R_E$ radius aligned with Z axis is superposed upstream of the prenoon bow shock at $Y = -5 R_E$, where X and Z axes denote the sunward and the northward direction, respectively, and Y completes the orthogonal triad. The solar wind density is set to be 25 /cc and 10 /cc inside and outside of the column, respectively. The solar wind velocity is 350 km/s in the negative X direction, and the corresponding dynamic pressure is 5.1 nPa and 2.0 nPa inside and outside of the column, respectively. In order to investigate the power supply due to the density impact regardless of dayside reconnection effects, IMF is set to be northward, IMF $(B_X, B_Y, B_Z) = (0.0, 2.5 \text{ nT}, 4.3 \text{ nT})$. The time axis is selected so that the density column appears in the upstream region of the Earth's bow shock ($X = 18 R_E$ at 0.0 min).

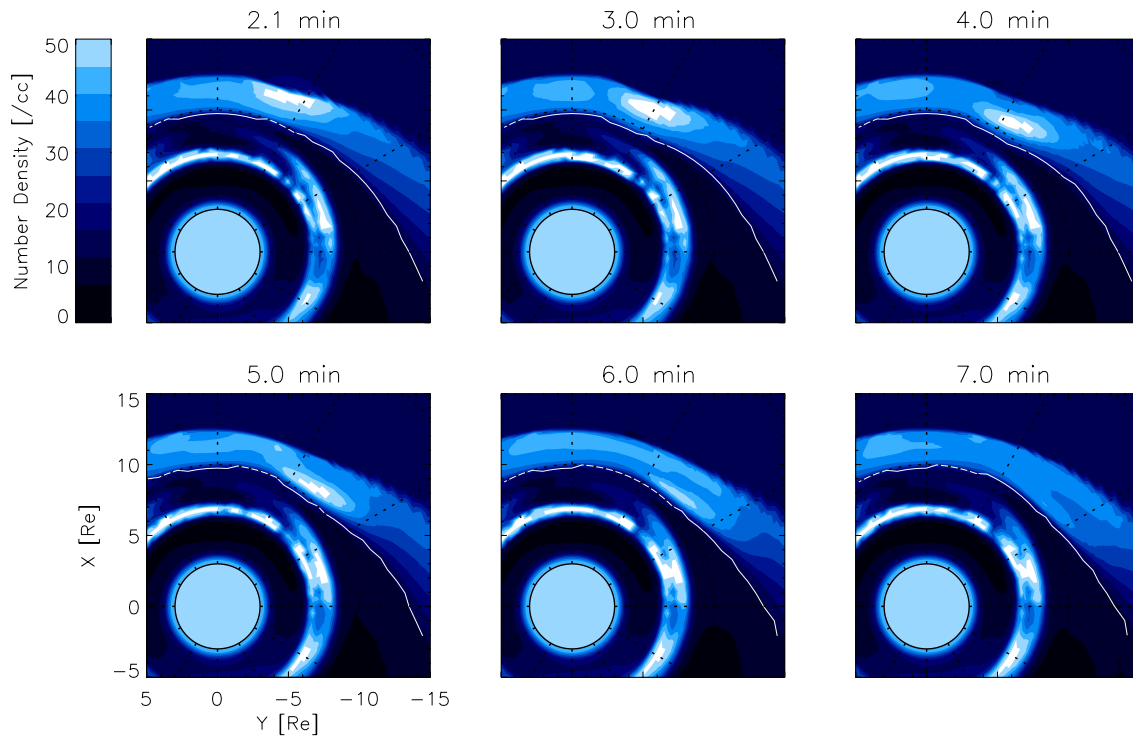


Figure 4.2. Equatorial maps of plasma density for the time interval from 2.1 min to 7.0 min. The contour interval is 5 /cc. Magnetopause location is shown as a white line in each panel.

Figure 4.2 shows the time evolution of the density distribution in the magnetospheric equatorial plane for the time interval from 2.1 min to 7.0 min to overview simulated plasma disturbances in the magnetosphere. We close up the prenoon sector because of no significant disturbances in the postnoon sector. Magnetopause location is shown with a white line in each panel. The density column arrives at the magnetopause at 2.1 min with a peak density of $>50/\text{cc}$ in the magnetosheath. The density column leads to a ripple propagating antisunward along the magnetopause after 3.0 min. Both the density column and the magnetopause ripple decay as traveling antisunward. The azimuthal extent of the magnetopause ripple ($\sim 5 R_E$) is comparable to that expected from observations of small-scale pressure pulses [e.g., *Sibeck et al.*, 2003].

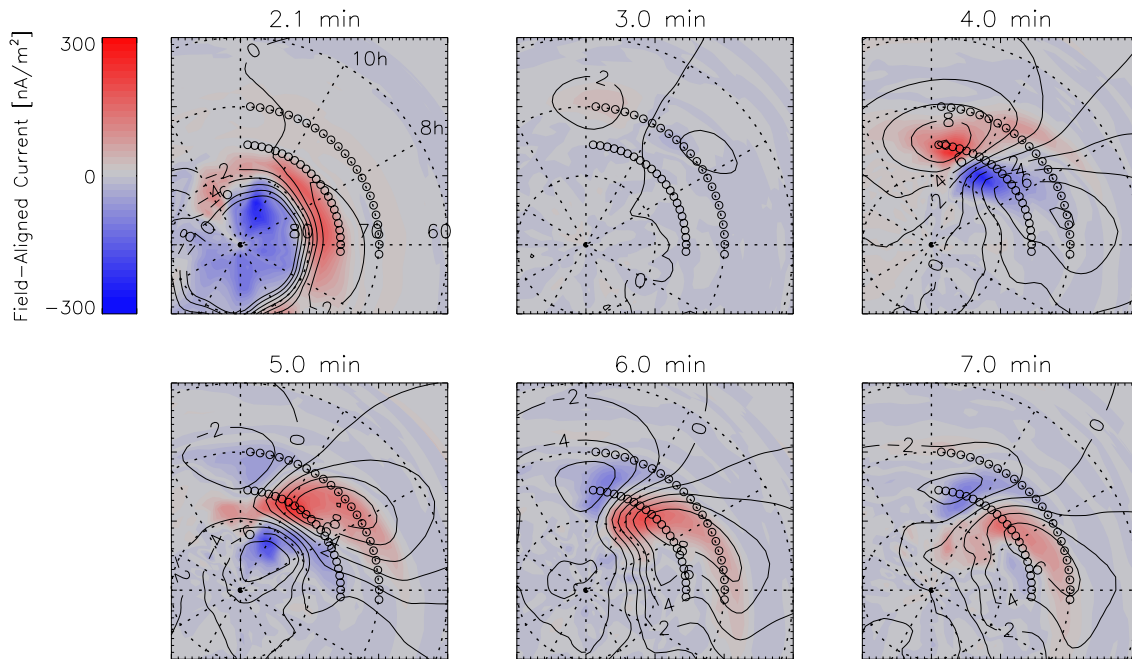


Figure 4.3. Time variation of field-aligned currents (colors) at the ionosphere level and that of the ionospheric electric potential (contour lines) for the time interval from 2.1 min to 7.0 min and in the latitude range higher than 60° . Red and blue colors indicate downward and upward field-aligned currents. The contour interval is 2 kV for the potential. Chains of circles indicate the ionospheric footprints of 70° and 75° magnetic field lines

4.2 Ionospheric Disturbances

TCVs are reproduced in this experiment as shown below. **Figure 4.3** shows temporal variations of field-aligned currents every 1 min in the latitude range higher than 60° in the ionosphere and for the time interval from 2.1 min to 7.0 min. Field-aligned currents shown by red and blue colors are downward (into the ionosphere; positive) and upward (out of the ionosphere; negative), respectively. Superposed contour lines show the ionospheric electric potential. The electric potential corresponds to the ionospheric convection vortices. In the northern hemisphere, ionospheric plasma flows clockwise and counterclockwise along the negative and positive contour lines, respectively. The first panel at 2.1 min shows a quasi steady current system and a corresponding convection pattern under northward IMF condition as explained by *Tanaka* [1999]. There are no signals associated with the density impact at 2.1 min. In order to demonstrate the perturbed features clearly, five panels after 2.1 min show the deviations of field-aligned currents and those of potential from those at 2.1 min.

At 3.0 min, a pair of clockwise (negative potential) and counterclockwise (positive potential) vortices appears at latitudes of $\sim 70^\circ$ centered around 8-9 and 11-13 hour local time (LT), respectively. In the time interval 4.0-6.0 min, the positive potential peak moves from 11 LT to 9 LT at the latitude

of $\sim 75^\circ$, resulting in the averaged propagation speed of ~ 7 km/s. At 5.0 min a new clockwise vortex (negative potential) appears centered around 11-13 LT. In the interval of 6.0-7.0 min, the negative potential peak moves from 12 LT to 11 LT at the latitude of $\sim 75^\circ$, giving an averaged propagation speed of ~ 7 km/s. The propagation speeds of the simulated TCVs are comparable with magnetometer observations [Murr *et al.*, 2002; Kataoka *et al.*, 2001, 2002, 2003; Amm *et al.*, 2002]. The skew of the simulated TCVs as moving away from noon is also consistent with magnetometer observations [e.g., Friis-Christensen *et al.*, 1988; Moretto *et al.*, 1997; Murr *et al.*, 2002].

It is interpreted that field-aligned currents generate the ionospheric potential. At 3.0 min, a pair of upward and downward field-aligned currents appears at latitudes of $\sim 70^\circ$ centered around 8-9 and 11-13 LT, respectively. This is essentially the same signature as the preliminarily impulse phase explained in detail by Fujita *et al.* [2003] except for a less LT extent due to the localized compression. At 4.0-5.0 min, when a pair of field-aligned currents grows and shifts toward higher latitudes and westward, a new upward field-aligned current appears at latitudes lower than the area of the preceding downward field-aligned current centered around 11-13 LT. After 6.0 min, a new pair of preceding downward and trailing upward field-aligned currents shifts westward with less distinguished latitudinal motion. In past observational studies, field-aligned current densities associated with TCVs have been estimated to be of the order of $1 \mu\text{A}/\text{m}^2$ [Glassmeier *et al.*, 1989; Glassmeier, 1992; Lanzerotti *et al.*, 1991; Lühr *et al.*, 1996; Murr *et al.*, 2002; Amm *et al.*, 2002]. The maximum density of a pair of field-aligned currents in our simulation is $\sim 0.3 \mu\text{A}/\text{m}^2$. The field-aligned currents are strong near the poleward and the rear edge of the simulated TCVs. This is also consistent with the picture obtained from recent observations [Kataoka *et al.*, 2001; Amm *et al.*, 2002]. In other words, the TCV centers tend to be located equatorward of the field-aligned current peaks. This could attribute to the fact that TCVs are often mapped well inside of the magnetopause [Moretto and Yahnin, 1998], while sometimes the source region was located much closer to the magnetopause [Kataoka *et al.*, 2001]. Thus it is concluded that the simulated ionospheric disturbances exhibit the common properties similar to those observed during TCVs.

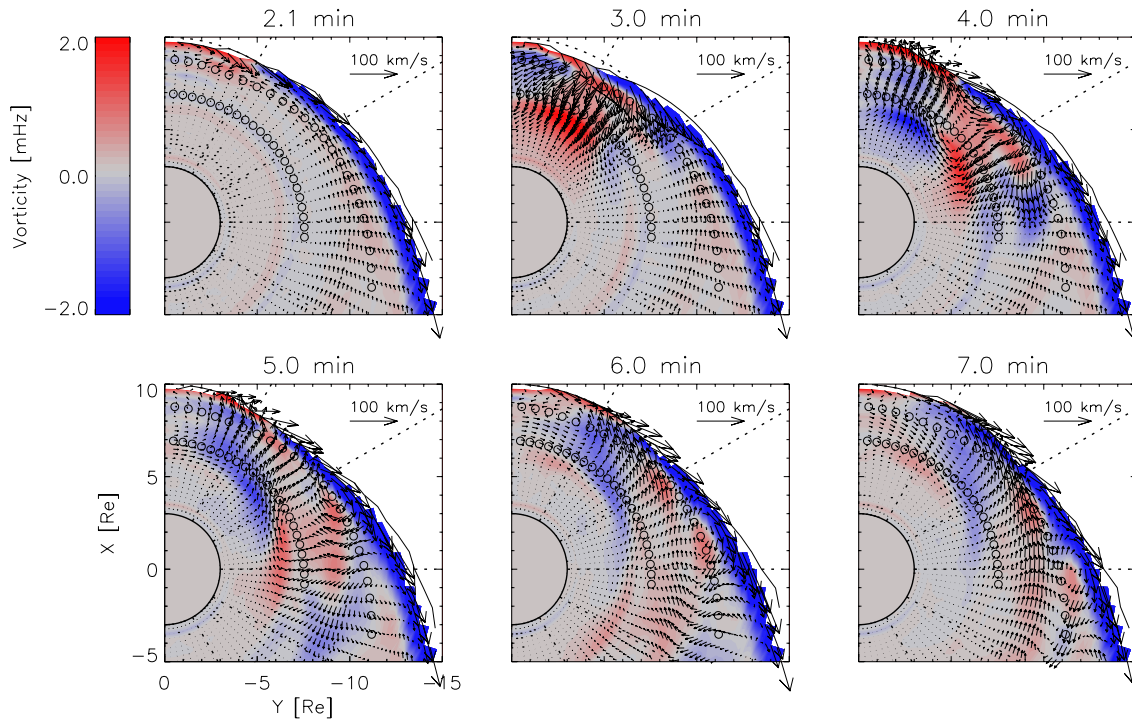


Figure 4.4. Maps of magnetospheric plasma flows (arrows) and vorticities (colors) on the equatorial plane in the prenoon sector for the simulation time interval from 2.1 min to 7.0 min. Vectors are drawn in the region where magnetic field is almost perpendicular to the equatorial plane. Chains of circles indicate the equatorial intersects of 70° and 75° magnetic field lines.

4.3 Magnetospheric Disturbances

From the simulation result of the ionospheric response, it is revealed that the localized density pulse in the solar wind is a possible source of TCVs. Therefore, the numerical results deserve to be analyzed in detail for investigation of magnetospheric plasma processes associated with TCVs. In order to understand how the field-aligned currents driving the simulated TCVs are generated in the magnetosphere, the magnetospheric plasma disturbances caused by the localized density pulse is investigated first. Bearing in mind that magnetospheric plasma flows and vorticities convey fundamental information about the magnetosphere-ionosphere system, their temporal variations in the equatorial plane are shown in **Figure 4.4**. Vectors of perpendicular plasma flows are shown as black arrows. Red and blue colors show positive and negative vorticities, respectively. The positive and negative vorticities correspond to downward (into the ionosphere) and upward (out of the ionosphere) field-aligned currents, respectively. The inner and outer chains of circles in **Figure 4.4** are the equatorial intersects of the field lines originated from the ionosphere at latitudes of 70° and 75° , respectively. The ionospheric ends of the 70° and 75° field lines are also shown as chains of circles in **Figure 4.3**.

In the magnetosphere at 2.1 min just before the impact, there are weak sunward flows in the magnetosphere and strong antisunward flows in the magnetopause region. These flows are associated with quasi steady magnetospheric plasma convection under northward IMF condition as explained by *Tanaka* [1999]. At 3.0 min, the density impact impinging onto the magnetopause invokes earthward flows around the perturbed region. This is a signature of compressional disturbance. The flows turn toward antisunward in the front region of the disturbance in the inner magnetosphere ($L < 6$). There appears a flow shear, in other words, Alfvén mode disturbances with field-aligned currents are produced. Actually, we confirmed that this is the mode conversion from the compressional wave to the shear Alfvén wave by the same way as discussed by *Fujita et al.* [2003]. At 4.0 min, these antisunward flows turn sunward to induce a flow shear in reverse sense. The same type of the shear structure was first reported by *Slinker et al.* [1999]. The flow shear fades away gradually after 5.0 min as propagating antisunward.

Basically, the electric charge, equivalent of the vorticity in the first approximation, is transmitted to the ionosphere as the electric potential with an Alfvén transit time delay because the energy is conveyed by shear Alfvén waves with field-aligned currents. There is 20-60 s (80-140 s) propagation time of Alfvén waves from the equatorial plane to the 70° (75°) ionosphere along the magnetic field lines. Considering this time delay, the vorticity distribution in **Figure 4.4** almost corresponds to the electric potential distribution at the ionosphere in **Figure 4.3**. It is worthwhile to note here that the distribution of the vorticity itself shows the skew in the equatorial plane. The longer Alfvén transit time in higher latitudes also enhances the skew of the TCVs in the ionosphere. In terms of the position of the source current of the field-aligned currents driving the simulated TCVs, it is concluded that the magnetopause current has a minor importance because of two reasons. First, there is a small field-aligned current near the open/close boundary at the ionospheric latitude of $\sim 80^\circ$ compared with the one of $\sim 75^\circ$ in **Figure 4.3**. The second reason is that the Alfvén transit time from the equatorial magnetopause to the ionosphere is too long (5-8 min) to become the effective source of the simulated TCVs.

4.4 Wave Equation of Field-Aligned Currents

The previous discussions revealed the correspondence between the ionospheric potential and the vorticity in the magnetosphere. However, the exact generation mechanism of field-aligned currents associated with TCVs remains an open question. It is possible to answer the question quantitatively by using the full 4-dimensional time-space data obtained through the simulation. However, in the realistic ambient magnetic field and plasma environment, it is difficult to analyze the magnetospheric disturbances by applying the former theoretical approaches developed under a simplified condition. The formula suitable for such analysis is the wave equation of field-aligned

currents proposed by *Itonaga et al.* [2000]. The wave equation is introduced below to evaluate the generation mechanism of field-aligned currents in detail.

$$\frac{1}{V_A^2} \frac{\partial^2 \delta j_{\parallel}}{\partial t^2} - \frac{1}{V_A^2} \frac{\partial}{\partial s} \left[V_A^2 B \frac{\partial}{\partial s} \left(\frac{\delta j_{\parallel}}{B} \right) \right] = T1 + T2 + T3 + T4 \quad (4.1)$$

$$T1 = -\frac{1}{V_A^2} \frac{\partial}{\partial s} (\nabla V_A^2 \cdot \delta \mathbf{j}_I) \quad (4.2)$$

$$T2 = \frac{1}{V_A^2} \left[\nabla^2 (V_A^2 \delta \mathbf{j}_I) \right]_{\parallel} \quad (4.3)$$

$$T3 = -\frac{1}{V_A^2} \frac{\partial}{\partial s} \left(\frac{V_A^2}{p_B} \nabla_{\perp} p_B \cdot \delta \mathbf{j}_D \right) \quad (4.4)$$

$$T4 = -\frac{1}{V_A^2} \frac{\partial}{\partial s} \left(\frac{V_A^2}{2p_B} \nabla_{\perp} (\delta p_B - \delta p) \cdot \mathbf{j}_D \right) \quad (4.5)$$

$$\delta \mathbf{j}_I = \frac{1}{B^2} \mathbf{B} \times \left(\rho \frac{\partial \delta \mathbf{u}}{\partial t} \right) \quad (4.6)$$

$$\delta \mathbf{j}_D = \frac{1}{B^2} \mathbf{B} \times (\nabla_{\perp} \delta p) \quad (4.7)$$

$$\mathbf{j}_D = \frac{1}{B^2} \mathbf{B} \times (\nabla_{\perp} p) \quad (4.8)$$

The variable s is a distance measured along the magnetic field line and increases in the direction of \mathbf{B} . The subscript \parallel stands for a scalar component parallel to \mathbf{B} . The term $\delta p_B = B \delta B / \mu_0$ is the perturbed magnetic pressure.

As shown in equations (4.2) and (4.3), T1 and T2 mean that the perturbed field-aligned current is produced by the perturbed inertia current (4.6) where there is inhomogeneity of Alfvén speed or curvature of the magnetic field line, respectively. The third term T3, shown in equation (4.4), shows that the perturbed field-aligned current is caused by the perturbed diamagnetic current (4.7) where the unperturbed magnetic pressure is inhomogeneous. The fourth term T4, shown in equation (4.5), means that the perturbed field-aligned current is generated by perturbations of the magnetic and plasma pressures where the diamagnetic current (4.7) flows in the unperturbed state. Note that the term T1 corresponds to the model suggested by *Lühr et al.* [1996] (L96), while the terms T3 and T4 are associated with the model suggested by *Glassmeier* [1992] (G92). Therefore, we can investigate the importance of these proposed models by evaluating these source terms from the simulated results.

Since there are no TCV models discussing the generation of field-aligned currents via the curvilinear effect T2, the meaning is explained in detail. Assume that the ambient magnetic field as $\mathbf{B} = \nabla \Phi \times \nabla \varphi$, where Φ and φ are Euler potentials [*Stern*, 1967], and $\nabla \Phi \cdot \nabla \varphi = 0$ without loss of generality. The Euler potentials Φ and φ are constant along each magnetic field line and

label the meridional and longitudinal directions, respectively. When the characteristic length in spatial variation of the perturbed inertial current is much smaller than those of the scale factors of the Euler potentials and the Alfvén speed, we can approximate the term T2 in a simple form [Itonaga *et al.*, 2000]

$$\frac{1}{V_A^2} \left[\nabla^2 (V_A^2 \delta \mathbf{j}_I) \right]_{\parallel} \sim \frac{2}{R_C} \frac{\partial \delta j_{\Phi}}{\partial s}, \quad (4.9)$$

where R_C denotes the radius of curvature of the magnetic field line designated by Φ . Equation (4.9) means that the curvilinear effect is enhanced when perturbed inertial currents in the curvature direction vary along with the magnetic field line in the case that there is a significant curvature. Therefore, the main source current of the curvilinear effect is the curvature component of the perturbed inertial current.

In order to evaluate each term in equation (4.1), we need to calculate perturbed values of MHD parameters. The perturbed values are defined as their deviations from those before the solar wind impulse at 2.1 min. The perturbed inertia current (4.6) is evaluated based on the following equation:

$$\rho \frac{\partial \delta \mathbf{u}}{\partial t} = (\mathbf{j} + \delta \mathbf{j}) \times (\mathbf{B} + \delta \mathbf{B}) - \nabla(p + \delta p). \quad (4.10)$$

Spatial derivatives are approximated by a central difference in spherical coordinates.

4.5 Discussion

Now it is discussed how the dominant field-aligned currents are excited in the magnetospheric source regions which are mapped to ionospheric latitudes of 70° and 75°. These field-aligned currents are associated with the strong perturbed flow shear as shown in **Figure 4.4**. **Figures 4.5** and **4.6** show the three-dimensional view of the magnetic field lines originated from the ionospheric latitudes of 70° and 75°, respectively. The circles in **Figures 4.3** and **4.4** are the footprints of these magnetic field lines at both ends. **Figures 4.5** and **4.6** have the same format and the same color scale for comparisons. The magnetopause positions at 2.1 min and 3.0 min are depicted as dotted and solid lines, respectively. Results are shown as snapshots at 3.0 min. The generation mechanism discussed hereafter is essentially the same even after 3.0 min, although the amplitude decays.

On the 70° latitude field lines, the diamagnetic terms T3 and T4 are negligible as shown in **Figures 4.5c** and **4.5d**. **Figures 4.5a** and **4.5b** show that, around the LT sector of the magnetopause ripple, the inhomogeneous effect T1 is dominant near the equatorial region, while the curvilinear effect T2 is dominant on the high latitude field lines off from the equatorial plane. This inhomogeneous effect T1 is interpreted by the mode conversion from compressional wave to shear Alfvén wave that occurs in the equatorial magnetosphere of $6 < L < 7$ where the radial gradient of Alfvén speed is enhanced as explained by *Fujita et al.* [2003].

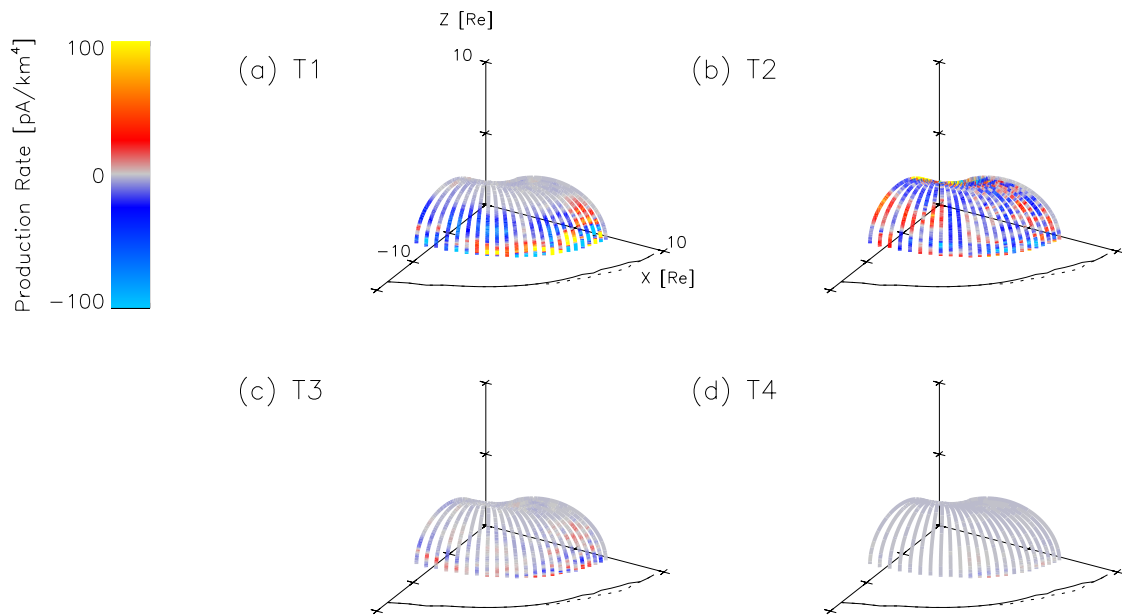


Figure 4.5. Three-dimensional view of the magnetic field lines on the $L = 6-7$ shell originated from the ionospheric latitude of 70° . The magnetopause positions at 2.1 min and 3.0 min are depicted on the equatorial plane as dotted and solid lines, respectively. Red and blue colors denote positive and negative amplitudes of the four source terms in wave equation (4.1).

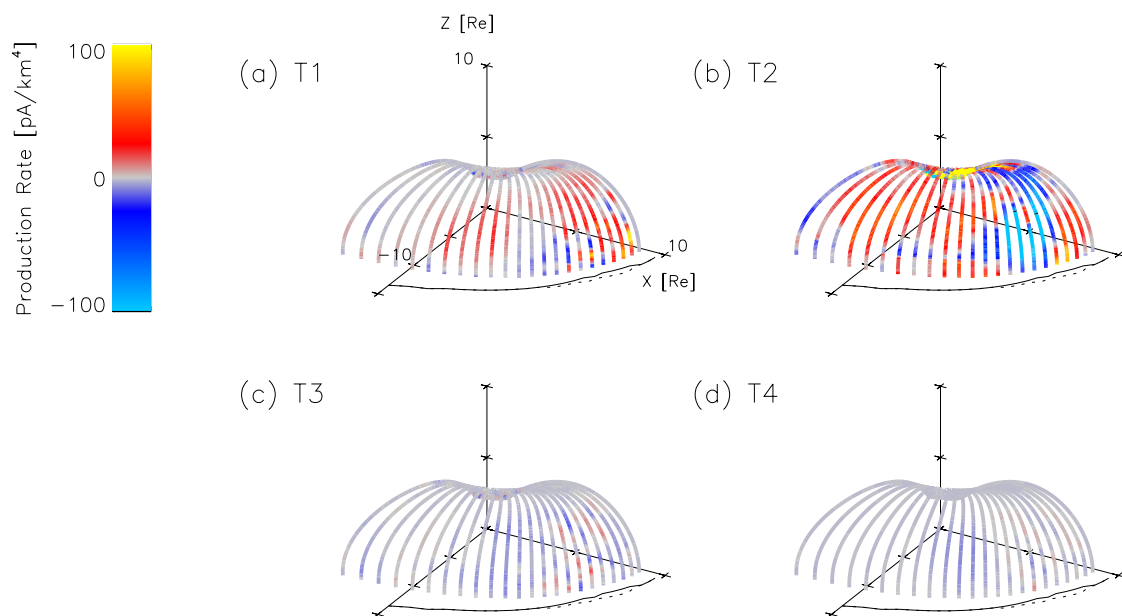


Figure 4.6. Three-dimensional view of the magnetic field lines on the $L = 8-10$ shell originated from the ionospheric latitude of 75° . The format and color scale are the same as **Figure 4.5**.

On the 75° latitude field lines, the diamagnetic terms T3 and T4, are negligible as seen in **Figures 4.6c** and **4.6d**. The inhomogeneous effect T1 is not dominant as shown in **Figure 4.6a** because of a lack of sharp gradient of Alfvén speed. As shown in **Figure 4.6b**, the curvilinear effect T2 is dominant off from the equatorial plane in the LT sector of the magnetopause ripple. The curvilinear effect appeared in **Figures 4.5b** and **4.6b** does not mean the mode conversion, but is interpreted by the conversion of polarization current into the field-aligned current within the shear Alfvén mode.

Let us summarize the evaluation of the generation mechanisms of field-aligned currents discussed above. The field-aligned currents driving the simulated TCVs are mainly generated in the magnetospheric region of $6 < L < 10$ with the inner and outer boundaries mapped to the ionospheric latitudes of 70° and 75° , respectively. The magnetopause, dealt by *Kivelson and Southwood* [1991] (KS91) and G92 model, is not identified as the main source region. The field-aligned currents produced in the KS91 and G92 models may be discriminated when the magnetopause ripple is much amplified, for example, as shown in *Sibeck et al.* [1999]. Simulation runs using several different types of solar wind drivers are very interesting as the next step. The field-aligned current suggested by the L96 model is not identified in the outer region mapped to the ionospheric latitude of 75° , although the mode conversion takes place in the inner region mapped to the ionospheric latitude of 70° . This is because the low-latitude boundary layer is not included in our simulation as proposed by the L96 model. In the real magnetosphere, however, the field-aligned current of the L96 model would be enhanced in the outer region because of sharp gradient of Alfvén speed at the inner edge of the low-latitude boundary layer.

Figure 4.7 shows an illustration summarizing the dominant generation mechanism of pairs of field-aligned currents due to a localized density pulse. The magnetopause is deformed by the localized impact, and a ripple structure moves antisunward. In-out plasma acceleration accompanied with the magnetopause deformation causes the inertia current, and the vorticity arises in the magnetosphere. Since the vorticity is approximately equivalent to the electric charge, discharge occurs via field-aligned currents in two ways. In the magnetospheric region of $8 < L < 10$, the inertial current is converted into the field-aligned current off from the equatorial plane via the curvilinear effect. On the other hand, in the magnetospheric region of $6 < L < 7$ where the sharp gradient of Alfvén speed exists, the inertia current is converted into the field-aligned current not only by the curvilinear effect but also via the inhomogeneous effect.

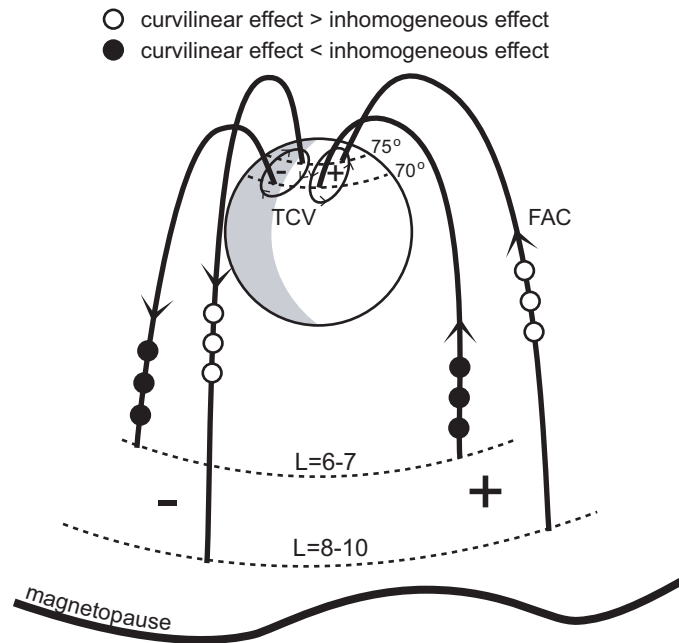


Figure 4.7. Summary sketch to describe the generation mechanism of field-aligned currents caused by a localized density pulse in the solar wind.

4.6 Summary

The essential effect by the production of the bow shock processes such as HFAs and foreshock cavities can be simplified and represented by localized density pulses. TCVs are reproduced by a global MHD simulation of the transient response of the magnetosphere-ionosphere system to such a localized density pulse in the solar wind. The dominant source of the field-aligned currents driving the simulated TCVs does not exist in the magnetopause region. The main source current of the field-aligned currents is the inertial current associated with plasma acceleration within the magnetosphere near the impact region. The curvilinear effect off from the equatorial plane is an important mechanism to produce the field-aligned currents. The inhomogeneous effect also generates the field-aligned currents at $L = 6-7$ where the sharp gradient of Alfvén speed exists.

Chapter 5

Conclusion

The whole topics associated with traveling convection vortices (TCVs) are compiled in this thesis. The generation mechanism and the energetics of TCVs are quantitatively revealed based on both observations and theories. Interaction processes between tangential discontinuities (TDs) and the Earth's bow shock play a dominant role for the generation of TCVs via the production of hot flow anomalies (HFAs). The magnetopause deformations due to localized pressure pulses associated with HFAs can explain the triggering process, temporal and spatial evolution of the three-dimensional current system, and all other features of TCVs. The inertial current associated with plasma acceleration within the magnetosphere near the impact region is converted into the field-aligned current to form this three-dimensional current system. This current system causes a transient production of localized dayside aurora and localized F region irregularities, with hundreds of km horizontal extent in the ionosphere. The total current intensity of this current system is 0.1-1 MA, and the total power supply into the ionosphere is 1-10 GW. It is concluded that TDs are the most effective solar wind discontinuities to produce TCVs, and the three-dimensional structure of TDs is essential to understand and to predict the transient response of the Earth's magnetosphere to solar wind discontinuities.

References

- Amm, O., M. J. Engebretson, T. Hughes, L. Newitt, A. Viljanen, and J. Watermann, A traveling convection vortex event study: Instantaneous ionospheric equivalent currents, estimation of field-aligned currents, and the role of induced currents, *J. Geophys. Res.*, 107(A11), 1334, doi:10.1029/2002JA009472, 2002.
- Andre, R., M. Pinnock, and A. S. Rodger, On the SuperDARN autocorrelation function observed in the ionospheric cusp, *Geophys. Res. Lett.*, 26(22), 3353-3356, 1999.
- Andre, R., M. Pinnock, J.-P. Villain, and C. Hanuise, On the factor conditioning the Doppler spectral width determined from SuperDARN HF radars, *Int. J. Geomag. Aeron.*, 2(1), 77-86, 2000.
- Araki, A physical model of the geomagnetic sudden commencement, in *Solar Wind Sources of Magnetospheric Ultra-Low Frequency Waves*, *Geophys. Monogr. Ser.*, 81, edited by M. J. Engebretson, K. Takahashi, and M. Scholer, 183-200, AGU, Washington, D. C., 1994.
- Ashour, A. A., The evaluation of the field of the currents induced in the earth by an external field whose distribution is known numerically, *Radio Sci.*, 6(2), 171-173, 1971.
- Baker, K. B., R. A. Greenwald, J. P. Villain, and S. Wind, Spectral characteristics of high-frequency (HF) backscatter from high latitude ionospheric irregularities: Preliminary analysis of statistical properties, Interim Rep., RADC-TR-87-284, Rome Air Dev. Cent., Griffis Air Force Base, N. Y., 1988.
- Baker, K. B., J. R. Dudeney, R. A. Greenwald, M. Pinnock, P. T. Newell, A. S. Rodger, N. Mattin, and C.-I. Meng, HF radar signatures of the cusp and low-latitude boundary layer, *J. Geophys. Res.*, 100(A5), 7671-7696, 1995.
- Bilitza, D., *International Reference Ionosphere 1990*, NSSDC 90-22, Greenbelt, Maryland, 1990.
- Cable, S., and Y. Lin, Three-dimensional MHD simulations of interplanetary rotational discontinuities impacting the Earth's bow shock and magnetosheath, *J. Geophys. Res.*, 103(A12), 29,551-29,567, 1998.
- Chen, G. X., Y. Lin, and S. Cable, Generation of traveling convection vortices and field-aligned currents in the magnetosphere by response to an interplanetary tangential discontinuity, *Geophys. Res. Lett.*, 27(21), 3583-3586, 2000.
- Cowley, S. W., Magnetosphere-ionosphere interactions: A tutorial review, in *Magnetospheric Current Systems*, *Geophys. Monogr. Ser.*, 118, edited by S. Ohtani et al., 91-106, AGU, Washington, D. C., 2000.
- Dungey, J. W., Interplanetary magnetic field and the auroral zones, *Phys. Rev. Lett.*, 6(2), 47-48, 1961.
- Fairfield, D. H., W. Baumjohann, G. Paschmann, H. Luhr, and D. G. Sibeck, Upstream pressure variations associated with the bow shock and their effects on the magnetosphere, *J. Geophys. Res.*, 95(A4), 3773-3786, 1990.

- Friis-Christensen, E., M. A. McHenry, C. R. Clauer, and S. Vennerstrom, Ionospheric traveling convection vortices observed near the polar cleft: A triggered response to sudden changes in the solar wind, *Geophys. Res. Lett.*, 15(3), 253-256, 1988.
- Fujita, S., T. Tanaka, T. Kikuchi, K. Fujimoto, K. Hosokawa, and M. Itonaga, A numerical simulation of the geomagnetic sudden commencement: 1. Generation of the field-aligned current associated with the preliminary impulse, *J. Geophys. Res.*, 108(A12), 1416, doi:10.1029/2002JA009407, 2003.
- Fukunishi, H., R. Kataoka, and L. J. Lanzerotti, Magnetic impulse events and related Pc 1 waves in the cusp and LLBL region observed by a ground magnetometer network, *COSPAR Colloquia Series 12, Space weather study using multipoint techniques*, edited by Ling-Hsiao Lyu, 237-241, 2002.
- Fukushima, N., Generalized theorem for no ground magnetic effect of vertical currents connected with Pedersen currents in the uniform-conductivity ionosphere, *Report of Ionosphere and Space Research in Japan*, 30(1/2), 35-40, 1976.
- Germany, G. A., M. R. Torr, D. G. Torr, and P. G. Richards, Use of FUV auroral emissions as diagnostic indicators, *J. Geophys. Res.*, 99(A1), 383-388, 1994.
- Glassmeier, K.-H., M. Honisch, and J. Untiedt, Ground-based and satellite observations of traveling magnetospheric convection twin vortices, *J. Geophys. Res.*, 94(A3), 2520-2528, 1989.
- Glassmeier, K.-H., and C. Heppner, Traveling magnetospheric convection twin vortices: Another case study, global characteristics, and a model, *J. Geophys. Res.*, 97(A4), 3977-3992, 1992.
- Glassmeier, K.-H., Traveling magnetospheric convection twin-vortices: observations and theory, *Ann. Geophys.* 10, 547-565, 1992.
- Greenwald, R. A., K. B. Baker, R. A. Hutchines, and C. Hanuise, An HF phases-array radar for studying small-scale structure in the high latitude ionosphere, *Radio Sci.*, 20(1), 63-79, 1985.
- Greenwald, R. A., K. B. Baker, J. R. Dudeney, M. Pinnock, T. B. Jones, E. C. Thomas, J. P. Villain, J. C. Cerisier, C. Senior, C. Hanuise, R. D. Hunsucker, G. Sofko, J. Kehler, E. Nielsen, R. Pellinen, A. D. M. Walker, N. Sato, and H. Yamagishi, DARN/SuperDARN: A global view of the dynamics of high-latitude convection, *Space Sci. Rev.*, 71(1-4), 761-796, 1995.
- Haerendel, G., G. Paschmann, N. Sckopke, H. Rosenbauer, and P. C. Hedgecock, The frontside boundary layer of the magnetosphere and the problem of reconnection, *J. Geophys. Res.*, 83(A7), 1978.
- Hedin, A. E., Extension of the MSIS thermospheric model into the middle and lower atmosphere, *J. Geophys. Res.*, 96(A2), 1159-1172, 1991.
- Hudson, P. D., Discontinuities in an anisotropic plasma and their identification in the solar wind, *Planet. Space Sci.*, 18, 1611, 1970.
- Hughes, W. J., and M. J. Engebretson, MACCS: Magnetometer array for cusp and cleft studies, in *Satellite - Ground Based Coordination Sourcebook*, edited by M. Lockwood et al., *Eur. Space Agency Spec. Publ.*, SP-1198, 119, 1997.
- Itonaga, M., A. Yoshikawa, and S. Fujita, A wave equation describing the generation of field-aligned current in the magnetosphere, *Earth Planets Space*, 52(7), 503-507, 2000.

- Kamide, Y., and S. Matsushita, Simulation studies of ionospheric electric fields and currents in relation to field-aligned currents 1. Quiet periods, *J. Geophys. Res.*, 84(8), 4083-4098, 1979.
- Kataoka, R., H. Fukunishi, L. J. Lanzerotti, C. G. MacLennan, H. U. Frey, S. B. Mende, J. H. Doolittle, T. J. Rosenberg, and A. T. Weatherwax, Magnetic Impulse Event: A detailed case study of extended ground and space observations, *J. Geophys. Res.*, 106(A11), 25,873-25,889, 2001.
- Kataoka, R., H. Fukunishi, L. J. Lanzerotti, T. J. Rosenberg, A. T. Weatherwax, M. J. Engebretson, and J. Watermann, Traveling convection vortices induced by solar wind tangential discontinuities, *J. Geophys. Res.*, 107(A12), 1455, doi:10.1029/2002JA009459, 2002.
- Kataoka, R., H. Fukunishi, K. Hosokawa, H. Fujiwara, A. S. Yukimatu, N. Sato, and Y.-K. Tung, Transient production of F region irregularities associated with TCV passage, *Ann. Geophys.*, 21, 1531-1541, 2003.
- Kelley, M. C., J. F. Vickrey, C. W. Carlson, and R. Torbert, On the origin and spatial extent of high-latitude F region irregularities, *J. Geophys. Res.*, 87(A6), 4469-4475, 1982.
- Kisabeth, J. L., and G. Rostoker, Modelling of three-dimensional current systems associated with magnetospheric substorms, *Geophys. J. R. Astr. Soc.*, 49, 655-683, 1977.
- Kivelson, M. G., and D. J. Southwood, Ionospheric traveling vortex generation by solar wind buffering of the magnetosphere, *J. Geophys. Res.*, 96(A2), 1661-1667, 1991.
- Konik, R. M., L. J. Lanzerotti, A. Wolfe, C. G. MacLennan, and D. Venkatesan, Cusp latitude magnetic impulse events, 2, Interplanetary magnetic field and solar wind conditions, *J. Geophys. Res.*, 99(A8), 14,831-14,854, 1994.
- Lanzerotti, L. J., L. C. Lee, C. G. MacLennan, A. Wolfe, and L. V. Medford, Possible evidence of flux transfer events in the polar ionosphere, *Geophys. Res. Lett.*, 13(11), 1089-1092, 1986.
- Lanzerotti, L. J., R. D. Hunsucker, D. Rice, L. C. Lee, A. Wolfe, C. G. MacLennan, and L. V. Medford, Ionosphere and ground-based response to field-aligned currents near the magnetospheric cusp regions, *J. Geophys. Res.*, 92(A7), 7739-7743, 1987.
- Lanzerotti, L. J., R. M. Konik, A. Wolfe, D. Venkatesan, and C. G. MacLennan, Cusp latitude magnetic impulse events 1. Occurrence statistics, *J. Geophys. Res.*, 96(A8), 14,009-14,022, 1991.
- Lee, G., C. T. Russell, and H. Kuo, Flux transfer events: spontaneous or driven?, *Geophys. Res. Lett.*, 20(9), 791-794, 1993.
- Lin, Y., L. C. Lee, and M. Yan, Generation of dynamic pressure pulses downstream of the bow shock by variations in the interplanetary magnetic field orientation, *J. Geophys. Res.*, 101(A1), 479-494, 1996a.
- Lin, Y., D. W. Swift, and L. C. Lee, Simulation of pressure pulses in the bow shock and magnetosheath driven by variations in interplanetary magnetic field direction, *J. Geophys. Res.*, 101(A12), 27,251-27,269, 1996b.
- Lin, Y., Global hybrid simulation of hot flow anomalies near the bow shock and in the magnetosheath, *Planet. Space Sci.*, 50, 577-591, 2002.

- Lin, Y., Global-scale simulation of foreshock structures at the quasi-parallel bow shock, *J. Geophys. Res.*, 108(A11), 1390, doi:10.1029/2003JA009991, 2003.
- Linson, L. M., and J. B. Workman, Formation of striation in ionospheric plasma clouds, *J. Geophys. Res.*, 75(16), 3211-3219, 1970.
- Lockwood, M., P. E. Sandholt, S. W. H. Cowley, and T. Oguti, Interplanetary magnetic field control of dayside auroral activity and the transfer of momentum across the dayside magnetopause, *Planet. Space Sci.*, 37(11), 1347-1365, 1989.
- Lockwood, M., and M. N. Wild, On the quasi-periodic nature of magnetopause flux transfer events, *J. Geophys. Res.*, 98(A4), 5935-5940, 1993.
- Lockwood, M., M. A. Hapgood, On the cause of a magnetospheric flux transfer event, *J. Geophys. Res.*, 103(A11), 26,453-26,478, 1998.
- Lühr, H., W. Blawert, and H. Todd, Ionospheric plasma and current patterns of travelling convection vortices: a case study, *J. Atmos. Terr. Phys.*, 55(14), 1717-1727, 1993.
- Lühr, H., M. Lockwood, P. E. Sandholt, T. L. Hansen, and T. Moretto, Multi-instrument ground-based observations of a traveling convection vortices event, *Ann. Geophys.*, 14, 162-181, 1996.
- Lysak, R. L., and D.-H Lee, Response of the dipole magnetosphere to pressure pulses, *Geophys. Res. Lett.*, 19(9), 937-940, 1992.
- Mende, S. B., H. U. Frey, J. H. Doolittle, L. J. Lanzerotti, and C. G. MacLennan, Dayside optical and magnetic correlation events, *J. Geophys. Res.*, 106(A11), 24,637-24,649, 2001.
- Milan, S. E., M. Lester, S. W. H. Cowley, J. Moen, P. E. Sandholt, and C. J. Owen, Meridian-scanning photometer, coherent HF radar, and magnetometer observation of the cusp: a case study, *Ann. Geophys.*, 17, 159-172, 1999.
- Moretto, T., E. Friis-Christensen, H. Luhr, and E. Zesta, Global perspective of ionospheric traveling convection vortices: Case studies of two GEM events, *J. Geophys. Res.*, 102(A6), 11,597-11,610, 1997.
- Moretto, T., A. Yahnin, Mapping travelling convection vortex events with respect to energetic particle boundaries, *Ann. Geophys.*, 16, 891-899, 1998.
- Murr, D. L., and W. J. Hughes, Reconfiguration timescales of ionospheric convection, *Geophys. Res. Lett.*, 28(11), 2145-2148, 2001.
- Murr, D. L., W. J. Hughes, A. S. Rodger, E. Zesta, H. U. Frey, and A. T. Weatherwax, Conjugate observations of traveling convection vortices: The field-aligned current system, *J. Geophys. Res.*, 107(A10), 1306, doi:10.1029/2002JA009456, 2002.
- Murr, D. L., and W. J. Hughes, Solar wind drivers of Traveling Convection Vortices, *Geophys. Res. Lett.*, 30(7), 1354, doi:10.1029/2002GL015498, 2003.
- Ossakow, S. L., and P. K. Chaturvedi, Current convective instability in the diffuse aurora, *Geophys. Res. Lett.*, 6(4), 332-334, 1979.

- Peredo, M., J. A. Slavin, E. Mazur, and S. A. Curtis, Three-dimensional position and shape of the bow shock and their variation with Alfvénic, sonic and magnetosonic Mach numbers and interplanetary magnetic field orientation, *J. Geophys. Res.*, 100(A5), 7907-7916, 1995.
- Ridley, A. J., T. Moretto, P. Ernstrom, C. R. Clauer, Global analysis of three traveling vortex events during the November 1993 storm using the assimilative mapping of ionospheric electrodynamic technique, *J. Geophys. Res.*, 103(A11), 26,349-26,358, 1998.
- Rodger, A. S., S. B. Mende, T. J. Rosenberg, and K. B. Baker, Simultaneous optical and HF radar observations of the ionospheric cusp, *Geophys. Res. Lett.*, 22(15), 2045-2048, 1995.
- Rodger, A. S., I. J. Coleman, and M. Pinnock, Some comments on transient and steady-state reconnection at the dayside magnetopause, *Geophys. Res. Lett.*, 27(9), 1359-1362, 2000.
- Rosenberg, T. J., and J. A. Doolittle, Studying the polar ionosphere and the magnetopause with automatic geophysical observatories: The U. S. program in Antarctica, *Antarct. J. U. S.*, 29(5), 347, 1994.
- Rostoker, G., J. C. Samson, F. Creutzberg, T. J. Hughes, D. R. McDiarmid, A. G. McNamara, A. Vallance Jones, D. D. Wallis and L. L. Cogger, CANOPUS- a ground-based instrument array for remote sensing the high latitude ionosphere during the ISTP/GGS program, *Space Sci. Rev.*, 71(1-4), 743-760, 1995.
- Russell, C. T., and R. L. McPherron, Semiannual variation of geomagnetic activity, *J. Geophys. Res.*, 78(1), 92-108, 1973.
- Russell, C. T., and R. C. Elphic, Initial ISEE magnetometer results: magnetopause observations, *Space Sci. Rev.*, 22(6), 681-715, 1978.
- Sato, M., H. Fukunishi, L. J. Lanzerotti, and C. G. MacLennan, Magnetic impulse events and related Pc1 bursts observed by the Automatic Geophysical Observatories network in Antarctica, *J. Geophys. Res.*, 104(A9), 19,971-19,982, 1999.
- Schunk, R. W., W. J. Raitt, and P. M. Banks, Effect of electric fields on the daytime high-latitude E and F regions, *J. Geophys. Res.*, 80(22), 3121-3130, 1975.
- Schunk, R. W., L. Zhu, and J. I. Sojka, Ionospheric response to traveling convection twin vortices, *Geophys. Res. Lett.*, 21(17), 1759-1762, 1994.
- Schwartz, S. J., C. P. Chaloner, P. J. Christiansen, A. J. Coates, D. S. Hall, A. D. Johnstone, M. P. Gough, A. J. Norris, R. P. Rijnbeek, D. J. Southwood, and L. J. C. Woolliscroft, An active current sheet in the solar wind, *Nature*, 318, 1985.
- Schwartz, S. J., Hot flow anomalies near the Earth's bow shock, *Adv. Space Res.*, 15(8/9), 107-116, 1995.
- Schwartz, S. J., G. Paschman, N. Sckopke, T. M. Bauer, M. Dunlop, A. N. Fazakerley, and M. F. Thomsen, Conditions for the formation of hot flow anomalies at Earth's bow shock, *J. Geophys. Res.*, 105(A6), 12,639-12,650, 2000.
- Shue, J.-H., P. Song, C. T. Russell, J. T. Steinberg, J. K. Chao, G. Zastenker, O. L. Vaisberg, S. Kokubun, H. J. Singer, T. R. Detman, H. Kawano, Magnetopause location under extreme solar wind conditions, *J. Geophys. Res.*, 103(A8), 17,691-17,700, 1998.

- Sibeck, D. G., W. Baumjohann, and R. E. Lopez, Solar wind dynamic pressure variations and transient magnetospheric signatures, *Geophys. Res. Lett.*, 16(1), 13-16, 1989.
- Sibeck, D. G., and G. I. Korotova, Occurrence patterns for transient magnetic field signatures at high latitudes, *J. Geophys. Res.*, 101(A6), 13,413-13,428, 1996.
- Sibeck, D. G., N. L. Borodkova, G. N. Zastenker, S. S. Romanov, and J.-A. Sauvaud, Gross deformation of the dayside magnetosphere, *Geophys. Res. Lett.*, 25(4), 453-456, 1998.
- Sibeck, D. G., N. L. Borodkova, S. J. Schwartz, et al., Comprehensive study of the magnetospheric response to a hot flow anomaly, *J. Geophys. Res.*, 104(A3), 4577-4593, 1999.
- Sibeck, D. G., K. Kudela, R. P. Lepping, R. Lin, Z. Nemecek, M. N. Nozdrachev, T.-D. Phan, L. Prech, J. Safrankova, H. Singer, Y. Yermolaev, Magnetopause motion driven by interplanetary magnetic field variations, *J. Geophys. Res.*, 105(A11), 25,155-25,169, 2000.
- Sibeck, D. G., R. B. Decker, D. G. Mitchell, A. J. Lazarus, R. P. Lepping, and A. Szabo, Solar wind preconditioning in the flank foreshock: IMP8 observations, *J. Geophys. Res.*, 106(A10), 21,675-21,688, 2001.
- Sibeck, D. G., N. B. Trivedi, E. Zesta, R. B. Decker, H. J. Singer, A. Szabo, H. Tachihara, and J. Watermann, Pressure-pulse interaction with the magnetosphere and ionosphere, *J. Geophys. Res.*, 108(A2), 1095, doi:10.1029/2002JA009675, 2003.
- Sitar, R. J., J. B. Baker, C. R. Clauer, A. J. Ridley, J. A. Cumnock, V. O. Papitashvili, J. Spann, M. J. Brittner, and G. K. Parks, Multi-instrument analysis of the ionospheric signatures of a hot flow anomaly occurring on June 24, 1996, *J. Geophys. Res.*, 103(A10), 23,357-23,372, 1998.
- Sitar, R. J., and C. R. Clauer, Ground magnetic response to sudden changes in the interplanetary magnetic field orientation, *J. Geophys. Res.*, 104(A12), 28,343-28,350, 1999.
- Slinker, S. P., J. A. Fedder, W. J. Hughes, J. G. Lyon, Response of the ionosphere to a density pulse in the solar wind: simulation of traveling convection vortices, *Geophys. Res. Lett.*, 26(23), 3549-3552, 1999.
- Sojka, J. J., L. Zhu, M. David, and R. W. Schunk, Modeling the evolution of meso-scale ionospheric irregularities at high latitudes, *Geophys. Res. Lett.*, 27(21), 3595-3598, 2000.
- Sonnerup, B. U. Ö., and L. J. Cahill Jr., Magnetopause structure and attitude from Explorer 12 observations, *J. Geophys. Res.*, 72(1), 171-183, 1967.
- Stern, D., Geomagnetic Euler potentials, *J. Geophys. Res.*, 72(15), 3995-4005, 1967.
- St.-Maurice, J.-P., and P. J. Laneville, Reaction rate of O⁺ with O₂, N₂, and NO under highly disturbed auroral conditions, *J. Geophys. Res.*, 103(A8), 17,519-17,521, 1998.
- Sugiura, M., and D. J. Poros, Hourly values of equatorial Dst for years of 1957 to 1970, Rep. X-645-71-278, Goddard Space Flight Center, Greenbelt, Maryland, 1971.
- Tamao, T., A hydromagnetic interpretation of geomagnetic SSC, *Rep. Ionos. Space Res. Jpn.*, 18, 16-31, 1964.

- Tanaka, T., Finite volume TVD scheme on an unstructured grid system for three-dimensional MHD simulation of inhomogeneous systems including strong background potential field, *J. Comput. Phys.*, 111(2), 381-389, 1994.
- Tanaka, T., Generation mechanisms for magnetosphere-ionosphere current systems deduced from a three-dimensional MHD simulation of the solar wind-magnetosphere-ionosphere coupling processes, *J. Geophys. Res.*, 100(A7), 12,057-12,074, 1995.
- Tanaka, T., Configuration of the magnetosphere-ionosphere convection system under northward IMF conditions with nonzero IMF By, *J. Geophys. Res.*, 104(A7), 14,683-14,690, 1999.
- Tanaka, T., The state transition model of the substorm onset, *J. Geophys. Res.*, 105(A9), 21,081-21,096, 2000a.
- Tanaka, T., Field-aligned current systems in the numerically simulated magnetosphere, in *Magnetospheric Current Systems*, 118, edited by S.-I. Ohtani, R. Fujii, M. Hesse, and R. L. Lysak, 53-59, AGU, Washington, D. C., 53, 2000b.
- Torrence, C., and G. P. Compo, A practical guide to wavelet analysis. *Bull. Amer. Meteor. Soc.*, 79, 61-78, 1998.
- Tsurutani, B. T., and C. M. Ho, A review of discontinuities and Alfvén waves in interplanetary space: Ulysses results, *Rev. Geophys.*, 37(4), 517-541, 1999.
- Valladares, C. E., D. Alcayde, J. V. Rodriguez, J. M. Ruohoniemi, A. P. Van Eyken, Observations of plasma density structures in association with the passage of traveling convection vortices and the occurrence of large plasma jets, *Ann. Geophys.*, 17, 1020-1039, 1999.
- Villain, J.-P., R. A. Greenwald, K. B. Baker, and J. M. Ruohoniemi, HF radar observations of E region plasma irregularities produced by oblique electron streaming, *J. Geophys. Res.*, 92(A11), 12,327-12,342, 1987.
- Vogelsang, H., H. Lühr, H. Voelker, J. Woch, T. Bösinger, T. A. Potemra, and P.-A. Lindqvist, An ionospheric travelling convection vortex event observed by ground-based magnetometers and Viking, 20(21), 2343-2346, 1993.
- Vorobjev, V. G., Dynamics of Hall vortices in the daytime high-latitude area, *Geomagn. Aeron., Engl. Transl.*, 33(5), 612-620, 1994a.
- Vorobjev, V. G., V. L. Zverev, and G. V. Starkov, Geomagnetic impulses in the daytime high latitude region: Main morphological characteristics and association with the dynamics of the daytime aurora, *Geomagn. Aeron., Engl. Transl.*, 33(5), 621-629, 1994b.
- Vorobjev, V. G., O. I. Yagodkina, and V. L. Zverev, Morphological features of bipolar magnetic impulse events and associated interplanetary medium signatures, *J. Geophys. Res.*, 104(A3), 4595-4607, 1999.
- Yeoman, T. K., M. Lester, S. W. H. Cowley, S. E. Milan, J. Moen, and P. E. Sandholt, Simultaneous observation of the cusp in optical, DMSP and HF radar data, *Geophys. Res. Lett.*, 24(17), 2251-2254, 1997.
- Zesta, E., W. J. Hughes, and M. Engebretson, A statistical study of traveling convection vortices using the Magnetometer Array for Cusp and Cleft Studies, *J. Geophys. Res.*, 107(A10), 1317, doi:10.1029/1999JA000386, 2002.

Vita

Name: Ryuho Kataoka

Place of Birth: Sendai, Miyagi, Japan

Post-secondary Education: Tohoku University, Sendai, 1995/04-1999/03, B.Sc. Physics
Tohoku University, Sendai, 1999/04-2001/03, M.Sc. Physics
Tohoku University, Sendai, 2001/04-2004/03, Ph.D. Physics

Awards and Honors: Outstanding Student Paper Award, AGU Fall Meeting, 1999
Research Fellow of the JSPS, 2001/04-2004/03

Publications:

- Kataoka, R., H. Fukunishi, L. J. Lanzerotti, C. G. MacLennan, H. U. Frey, S. B. Mende, J. H. Doolittle, T. J. Rosenberg, and A. T. Weatherwax, Magnetic Impulse Event: A detailed case study of extended ground and space observations, *J. Geophys. Res.*, 106(A11), 25,873-25,889, 2001.
- Kataoka, R., H. Fukunishi, L. J. Lanzerotti, T. J. Rosenberg, A. T. Weatherwax, M. J. Engebretson, and J. Watermann, Traveling convection vortices induced by solar wind tangential discontinuities, *J. Geophys. Res.*, 107(A12), 1455, doi:10.1029/2002JA009459, 2002.
- Kataoka, R., H. Fukunishi, K. Hosokawa, H. Fujiwara, A. S. Yukimatu, N. Sato, and Y.-K. Tung, Transient production of F region irregularities associated with TCV passage, *Ann. Geophys.*, 21, 1531-1541, 2003.
- Kataoka, R., H. Fukunishi, and L. J. Lanzerotti, Statistical identification of solar wind origins of magnetic impulse events, *J. Geophys. Res.*, 108(A12), 1436, doi:10.1029/2003JA010202, 2003.
- Kataoka, R., H. Fukunishi, S. Fujita, T. Tanaka, and M. Itonaga, Transient response of the Earth's magnetosphere to a localized density pulse in the solar wind: Simulation of traveling convection vortices, *J. Geophys. Res.*, 109, A03204, doi:10.1029/2003JA010287, 2004.